2014

Full Wave Electromagnetic Simulations of Terahertz Wire Grid Polarizers and Infrared Plasmonic Wire Gratings

John Cetnar
Wright State University

Follow this and additional works at: https://corescholar.libraries.wright.edu/etd_all

Part of the Engineering Commons

Full Wave Electromagnetic Simulations of Terahertz Wire Grid Polarizers and Infrared Plasmonic Wire Gratings

A dissertation submitted in partial fulfillment of the
requirements for the degree of
Doctor of Philosophy

By

JOHN S. CETNAR
B.S. in Engineering, Wright State University, 1989
Master in Business Administration, Wright State University, 1998
Master in Science, Wright State University, 2010

2014
Wright State University

WRIGHT STATE UNIVERSITY

GRADUATE SCHOOL

March 28, 2014

I HEREBY RECOMMEND THAT THE DISSERTATION PREPARED UNDER MY SUPERVISION BY <u>John S. Cetnar</u>, ENTITLED <u>Full Wave Electromagnetic Simulations of Terahertz Wire Grid Polarizers and Infrared Plasmonic Wire Gratings</u> BE ACCEPTABLE IN PARTIAL FULFILLMENT OF THE REQUIREMENTS FOR THE DEGREE OF <u>Doctor of Philosophy.</u>

_____
Elliott Brown, Ph.D.
Dissertation Director

_____
Ramana Grandhi, Ph.D.
Director, Ph.D. in Engineering Program

_____
Robert E. W. Fyffe, Ph.D.
Vice President of Research and
Dean of the Graduate School

Committee on Final Examination

_____
Elliott Brown, Ph.D.

_____
Douglas Petkie, Ph.D.

_____
Jason Deibel, Ph.D.

_____
Peter Powers, Ph.D.

_____
Dave Tomich, Ph.D.

ABSTRACT

Cetnar, John S. Ph.D., Engineering Ph.D. Program, College of Engineering and Computer Science, Wright State University, 2014. *Full Wave Electromagnetic Simulations of Terahertz Wire Grid Polarizers and Infrared Plasmonic Wire Gratings.*

This dissertation is a study of the interaction of terahertz (THz) and long-wave infrared (LWIR) radiation with various periodic sub-wavelength metallic structures in free-space and on dielectric substrates. There are many new and useful applications for both THz and LWIR radiation. Unfortunately, heavy attenuation by the Earth's atmosphere and low output power from THz sources combine to make THz radiation weak and difficult to detect. LWIR is not as prone to atmospheric attenuation as THz radiation. Nevertheless, the detection of LWIR can be improved upon by strengthening the coupling between incoming radiation and LWIR detector systems.

Light passing through periodic sub-wavelength metallic structures can exhibit extraordinary optical transmission (EOT). When EOT occurs, the amount of light transmitted through such structures is enhanced to well beyond what would be predicted by geometric optics. In addition, exceedingly high electromagnetic (EM) fields develop in the apertures and along the conducting surfaces of EOT structures. These enhanced fields may be used to improve the performance of a THz or LWIR detector through a significant reduction in its size while maintaining good external radiation coupling.

Full-wave numerical simulations using the finite element method (FEM) were used to study the interaction of THz and LWIR radiation with one- and two-dimensional surface plasmonic EOT structures. This dissertation examines the numerical solutions to the Helmholtz wave equation for radiation interacting with plasmonic structures in both the THz and LWIR regions. The simulation results predict that both EOT and EM field enhancement will occur in both regions. In several cases, plasmonic structures designed from optimized FEM results have been fabricated and characterized. The experimental results confirm the simulation predictions qualitatively and quantitatively to within a few dB. Nevertheless, it must be noted that although detectors were a strong motivation for the research conducted here, the realization of detector improvement was not carried out.

Contents

List of Figures

List of Tables

Acknowledgements

I wish to thank almighty God for the inspiration, motivation, wisdom, courage, and strength to do this work. With faith, all things are possible.

I wish to thank my family: Robyn, Sarah, Luke, and Dan for their patience, love, and support while I spent the many hours needed to complete my degree. I could not have done this without you. I also wish to thank my parents, Mary and Ted Cetnar who put my feet on the path of faith and knowledge. Rest in peace Mom and Dad.

I wish to thank my advisor, Dr. Elliott Brown. You encouraged me to follow this line of research; you challenged me intellectually in ways I had never challenged before; you gave me research work that I feel was not only unique and interesting but relevant to THz science and well suited to me. Although not a theoretical or computational physicist, you have guided me very well. You were a seemingly inexhaustible source for books, papers, ideas, and resources. Thank you, I really appreciate your help.

I wish to thank my co-workers, especially John Middendorf and Dr. Matthieu Martin, for your friendship, help, and advice along the way. It has been a pleasure working with you.

To the rest of my thesis committee: Dr. Doug Petkie, Dr. Jason Diebel, Dr. Peter Powers, and Dr. David Tomich, thank for your inputs, advice, and support over the last four years.

1. Introduction

1.1. The Electromagnetic Spectrum

Terahertz (THz) radiation occupies a region of the electromagnetic spectrum above microwaves and below infrared (IR). Long wave infrared (LWIR) radiation occupies a portion of the IR region comprising wavelengths from 6 μm to 15 μm [1]. Thus, LWIR straddles the 8 μm to 14 μm atmospheric transmission window [1]. Fig. 1-1 shows the electromagnetic
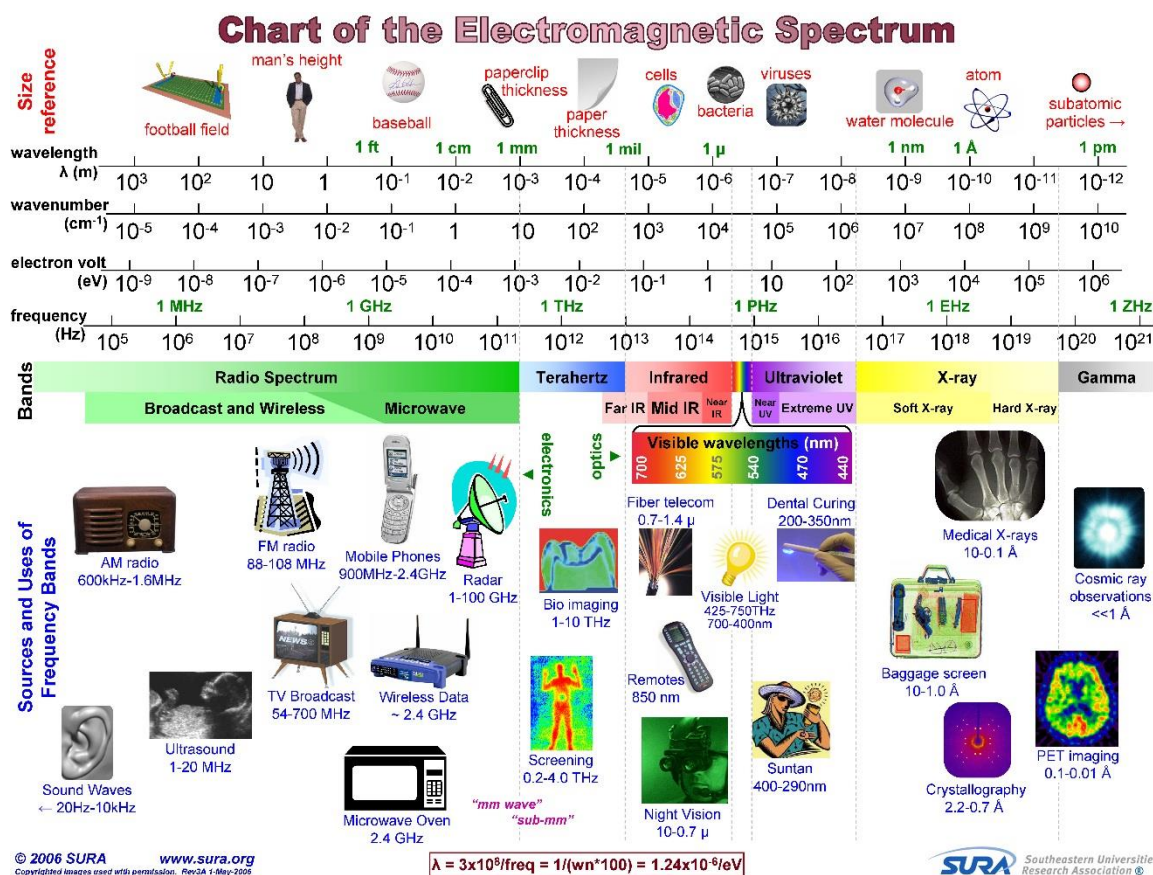
Fig. 1-1: The electromagnetic spectrum. From SUMA (Southeastern Universities Research Association) - www.sura.org.

spectrum of radiation measured in wavelength (m), wavenumber (cm^{-1}), energy (eV), and frequency (Hz). In addition, it includes a size reference comparing wavelengths to well-known objects, common band names for specific spectral regions, radiation sources, and some of the technological uses for the various types of radiation.

In this figure, the THz region is shown in the middle of the spectrum between the frequencies of 300 GHz ($\lambda = 1$ mm) and 10 THz ($\lambda = 30$ μm). Despite being the subject of great scientific interest since the 1920s, this region has been and remains one of the least explored regions of the electromagnetic spectrum [2]. Per Gallerano et al, THz radiation is defined in the frequency band from 100 GHz to 10 THz (3 mm to 30 μm) [3]. Strictly speaking, frequencies between 100 and 300 GHz are considered to be millimeter waves; but, there are no exact rules governing these definitions. This study adopts the convention stated above (100 GHz to 10 THz, although the maximum frequency in this study is 4 THz). As seen in Fig. 1-1, the wavelengths of THz radiation correspond to dimensions between the thicknesses of a paperclip and a sheet of paper. Two applications are shown in Fig. 1-1: bio-imaging and security screening.

LWIR radiation exists on and around the boundary of two wider bands called the Far IR and the Mid IR. LWIR wavelengths correspond to the dimensions of biological cells. Thermal night vision is one major application of LWIR radiation presented in the figure.

1.2. The THz Region: Detectors, Applications, and Challenges

THz radiation has received a significant amount of attention over the past few years. This interest comes from both the purely scientific and applications points of view. From a scientific standpoint, it is only within the last decade or so that advances in electronics and

photonics have made THz sources and detectors more widely available [4]. Because of this, the THz region is not a region of the electromagnetic spectrum that has been as heavily explored or exploited as other regions. Therefore, this region has been known as the "THz gap".

From an applications standpoint, microwave and radar technologies are trending toward shorter wavelengths with the aim of achieving better resolution and smaller system size for imaging and spectroscopy [5]. Meanwhile, optical and IR technologies are trending toward longer wavelengths due to the better transmission properties of THz radiation through most dielectrics and insulating materials [6]. THz is so interesting because it has many of the best properties of both microwaves and IR. Like microwaves, it can penetrate dielectric materials such as cloth, plastics, and wood. Further, THz radiation can penetrate dust, smoke, and fog (see Fig. 1-2) better than IR radiation therefore is superior to IR in navigation applications under these conditions [7], [8]. As a case in point, a small short-range navigation radar system designed for use in a micro-UAV has recently been demonstrated in the W-band [9].

THz radiation is non-ionizing making it very attractive for biomedical imaging application such as Terahertz Computed Tomography (T-Ray CT) and T-Ray QCL (Terahertz Computed Tomography using Quantum Cascade Lasers) [10]. THz radiation is also able to penetrate dielectrics, this makes THz radiation very desirable for security applications such as concealed weapons detection [11]. THz radiation can penetrate many types of paints and coatings. Therefore, it can be used to detect damage in underlying metallic surfaces in non-destructive evaluation (NDE) applications [12], [13]. It can also be used in the remote sensing of vital signs [14], [15] thus providing value in the biomedical and radar fields. THz radiation has also proven to be a unique tool in the medical diagnosis and treatment of burns [16]–[19].

3

Further, THz spectroscopy has been an active field of research for many years now. It has greatly aided our understanding of molecular structures and dynamics [20]–[23]. Finally, THz astronomy is a very important field of research. Spectral signatures of ions, atoms, and molecules in the interstellar medium are fundamental to our understanding of the composition and origin of our Solar System, stellar evolution, our Galaxy, and the Cosmos itself [24], [25].

However, there are some major challenges associated with the use of the THz region, particularly for terrestrial applications. An examination of Fig. 1-2 shows why. The propagation of THz radiation is strongly affected by the Earth's atmosphere. Fig. 1-2 shows the attenuation of electromagnetic radiation in the atmosphere as a function of frequency from microwave (λ = 30 cm) through ultraviolet (λ = 300 nm) as calculated by the Laser Environmental Effects Definition and Reference (LEEDR) atmospheric propagation modeling software developed at the Air Force Institute of Technology's Center for Directed Energy at Wright Patterson Air Force Base, Dayton, Ohio [26].
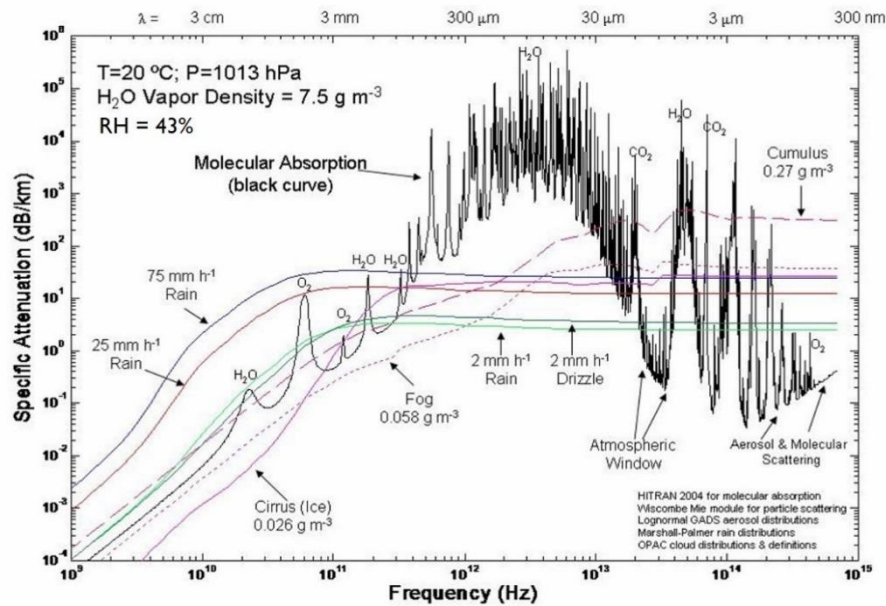
Fig. 1-2: Atmospheric attenuation of electromagnetic radiation across the THz region. From Fiorino et al [26].

The main black curve in the figure shows the attenuation of electromagnetic radiation versus frequency at a given temperature, pressure, and humidity. This curve assumes attenuation in a humid atmosphere with no clouds or precipitation. The solid colored curves show the effects due to rain. The dashed colored curves show the effects due to fog and clouds. The attenuation curve is marked by many resonant peaks of high attenuation and windows of lower attenuation between the peaks. These peaks are due to molecular absorption, primarily from molecular oxygen, carbon dioxide, and water vapor. In the region below 10 THz, the predominant absorber is molecular water vapor.

Wavelengths corresponding to the "atmospheric windows" are typically used for transmission. The minimum attenuation in the widows is the result of the far wings of the peak line shapes and an underlying floor, or continuum. As can be seen, the attenuation continuum increases with frequency starting in the microwave region through the THz region. A peak is reached at approximately 5 THz. Attenuation then decreases with frequency until around 30 THz ($\lambda = 10$ μm) in the region labeled "Atmospheric Window". This region corresponds to the LWIR region. Attenuation then oscillates in strength up to higher frequencies with a minimum occurring in the visible portion of the spectrum. Above the visible region, the continuum attenuation increases again into the ultraviolet. The effect of rain, fog, clouds, and other hydrometeors is to raise the continuum at frequencies above 300 GHz, in the LWIR region, and in the visible region. Atmospheric attenuation of THz radiation is strong and highly variable. This makes the atmospheric propagation of THz radiation over any long distance problematic at best.

To compound the atmospheric transmission problem, compact THz radiation sources, though now widely available, are not often very powerful. Generating THz radiation is

difficult. The distribution of radiation emitted by blackbodies is described by Planck's radiation formula, which is given by [27]:

$$I(\lambda) = \frac{2\pi hc^2}{\lambda^5 \left(e^{hc/\lambda k_B T} - 1\right)}$$

(1.1)

where $I(\lambda)$ is the spectral emittance, λ is the wavelength, T is the absolute temperature, c is the speed of light, h is Planck's constant, and k_B is the Boltzmann constant. A plot of (1.1) for T = 200 K, T = 300 K, and T = 400 K is shown in Fig 1-3. In the terrestrial environment, one can
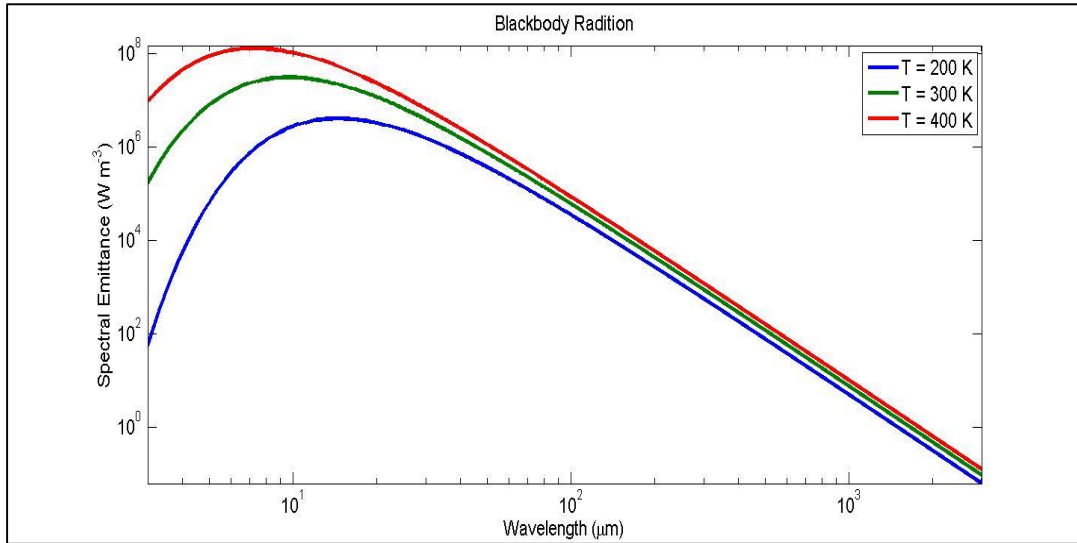
Fig 1-3: Blackbody radiation for a body at T = 200 K, T = 300 K, and T = 400 K.

generally assume that T > 200 K. Therefore, in the THz region, $hc/\lambda \ll k_B T$ so that $\exp(hc/\lambda k_B T) \approx 1 + hc/\lambda k_B T$. Using this approximation, (1.1) can be simplified to

$$I(\lambda) = \frac{2\pi c k_B T}{\lambda^4}$$

(1.2)

(1.2) is known as the Rayleigh-Jeans approximation in radiation theory. Fig 1-3 shows the Rayleigh-Jeans approximation is very good in the limit of large wavelength.

6

The total amount of radiation emitted by a blackbody source, known as the intensity I, can be calculated by integrating (1.1) from 0 to ∞. As can be seen from Fig 1-3, the wavelength at which the peak spectral emittance occurs decreases with increasing temperature while the intensity of a blackbody increases with increasing temperature per the Stephan-Boltzmann law [27].

$$I = \int_0^\infty I(\lambda)\,d\lambda = \sigma T^4 \qquad (1.3)$$

Blackbodies with peak spectral emittance in the THz region are at very low temperatures and have low intensities. Further, the spectral emittance in the THz region from a blackbody at any temperature is very low. For example, using the Rayleigh-Jeans approximation, (1.2), the calculated spectral emittance at 1 THz of a blackbody at 300 K is only 963 Watts per meter cubed (W/m^3). Using (1.1), we find that the same blackbody will radiate 3.10e7 W/m^3 at 30 THz ($\lambda = 10$ μm), a difference of over four orders of magnitude.

The most common THz detectors are thermal detectors and Schottky diodes. Some important thermal detectors, such as Golay cells, bolometers, and pyroelectric detectors will be discussed in Section 1.3. Schottky diodes have been used for detection and mixing in the THz region for many years now and are well understood. The nonlinear rectification property of the metal-semiconductor junction in the Schottky diode rectifier allows for both detection and mixing [28]. The frequency conversion properties of the Schottky diode rectifier as well as its intrinsic sensitivity are described by classical rectifier theory [29]. The Schottky diode has excellent performance characteristics while operating at room temperature including a useful sensitivity over a very large wavelength range, from microwave to THz ($\lambda = 100$ μm), and a very large instantaneous bandwidth which is limited only by the intermediate (in mixers)

7

or the baseband (in rectifiers) frequency circuitry [28]. In addition, Schottky diodes can be fabricated in many geometries to fit the application need at hand. The three most common geometries are the whisker-contacted honeycomb, the beam-lead diode, and the planar or surface-oriented diode [28].

The Schottky diode rectifier is classified as a square-law detector. A square-law detector is a device or circuit which produces an output that is proportional to the square of its input [28]

$$X_{out} = AX_{in}^2 \qquad (1.4)$$

where X_{out} is the device output (current or voltage), X_{in} is the input signal, and A is a proportionality constant dependent only on detector characteristics and not on the power level, at least up to the saturation level where higher-order effects become observable.

The general figures of merit for detectors (THz and LWIR) are the power signal-to-noise ratio (SNR), the responsivity, the noise equivalent power (NEP), the detectivity, and the specific detectivity [1]. The SNR is the ratio of the mean signal power received $< P >$ over the noise power received $<(\Delta P)^2>$; SNR can also be written in terms of the power spectral density S_P and the equivalent noise bandwidth B_{ENB} [28]

$$SNR = \frac{< P >}{\sqrt{<(\Delta P)^2 >}} = \frac{< P >}{S_P B_{ENB}} \qquad (1.5)$$

Responsivity is the ratio of the average value of the electrical signal output of the detector to the average value of the input radiation power. Responsivity is essentially the transfer function of the detector. For the square-law Schottky diode rectifier, and an input signal $x(t) = B \cos(\omega t + \varphi)$, the output is given by [28]

$$X_{out} = AB^2/2 = R_x P_{in} \tag{1.6}$$

The responsivity is then

$$R_x = \frac{X_{out}}{P_{in}} \tag{1.7}$$

where R_x is the responsivity, X_{out} is the average detector output signal (current or voltage), and P_{in} is the incident radiation power.

The NEP is the incident signal power received by the detector needed to produce an output power signal-to-noise ratio (SNR) of 1. NEP can be written in terms of responsivity as

$$NEP = \frac{X_{out}}{R_x G_{Tot}} \tag{1.8}$$

where G_{Tot} is the total detector gain including all loss and impedance matching effects. The detectivity is the reciprocal of the NEP [30].

$$D = \frac{1}{NEP} \tag{1.9}$$

For many detectors the NEP is proportional to the square root of the input signal which is proportional to detector area, A_d. This makes both NEP and detectivity dependent on electrical bandwidth and detector area. Therefore, the specific detectivity, D*, is defined to be the detectivity of a sensor with detector area of 1 cm^2 and a bandwidth normalized to 1 Hz [30]. D* is useful when comparing detectors of the same type having different areas. The specific detectivity is given by

$$D* = D\sqrt{A_d \Delta f} = \frac{\sqrt{A_d \Delta f}}{NEP} \tag{1.10}$$

where Δf is the electrical bandwidth.

9

THz detectors must contend with weak radiation sources and significant atmospheric attenuation in terrestrial environments. These factors often translate into lower than desired SNR values, higher than desired NEPs, and lower than desired Ds and D*s. There are three ways to improve sensor system performance. The first is to improve the transmission channel in order to lower the propagation attenuation. The second is to increase the power of the radiation source. The third is to increase the sensitivity of the detector. We cannot change the first because it is fundamental physics. Historically, from RF through UV, the third of these methods has played a much more important role in improving system performance than the second.

This dissertation is concerned with improving the sensitivity of detector systems. In the THz region, all system performance improvements are based upon enhancing the coupling between the incoming radiation and the detector device. No design changes to the detector device are endeavored. Instead, EOT structures, such as wire-grid polarizers, which can be added to the system design in close proximity to the detector, are investigated as coupling enhancement mechanisms.

1.3.   The LWIR Region: Detectors, Applications and Challenges

There is also a great deal of interest in LWIR radiation. This is primarily due to the many applications that benefit from LWIR technologies. LWIR detectors typically operate from wavelengths of 8-14 μm [1],[31]. There are two types of LWIR detectors: photon detectors and thermal detectors.

Photon detectors can be divided into two broad classes, unipolar (majority carriers only) and bipolar (minority and majority carriers) devices [1]. There are five material systems

10

on which photon detectors are based. First, direct bandgap semiconductors (bipolar) using binary alloys such as InSb and InAs, ternary alloys which use HgCdTe and InGaAs, and Type II and III superlattices which use InAs/GaInSb and HgTe/CdTe [1]. Second, there are extrinsic semiconductors (unipolar) using Si:As, Si:Ga, Si:Sb, Ge:Hg, and Ge:Ga [1]. Third, there are Type I superlattices (unipolar) using GaAs/AlGaAs. These form quantum well infrared photodetectors (QWIPs) [1]. Fourth, there are Silicon Schottky barriers (unipolar) which use PtSi and IrSi [1]. Fifth, there are high-temperature superconductors (minority carriers) [1].

Photon detectors absorb radiation by transferring the energy from incident photons to: 1) bound electrons in the valence band, exciting the electrons into the conduction band (intrinsic absorption); 2) electrons in a donor level, exciting the electrons into the conduction band (extrinsic absorption); or 3) free electrons already in the conduction band exciting them to higher states within the conduction band (free electron absorption). Note that there are analogous processes for holes. The fundamental optical excitation processes in semiconductors (intrinsic absorption, extrinsic absorption, and free carrier absorption) are shown in Fig 1-4.

Under an applied bias voltage, carriers excited by one of these processes drift toward one of the device electrodes, and are then sensed as electrical current by external circuitry. Because of this process, photon detectors show a highly selective wavelength dependence in their response per unit incident radiation power. A qualitative comparison of the frequency response of a photon detector and a thermal detector is shown in Fig 1-5.

Photon detectors exhibit excellent SNRs and very fast response times [1]. Unfortunately, photon detectors usually require cryogenic cooling in order to achieve this. Photon detectors with long-wavelength limits beyond 3 μm are usually cooled to reduce the
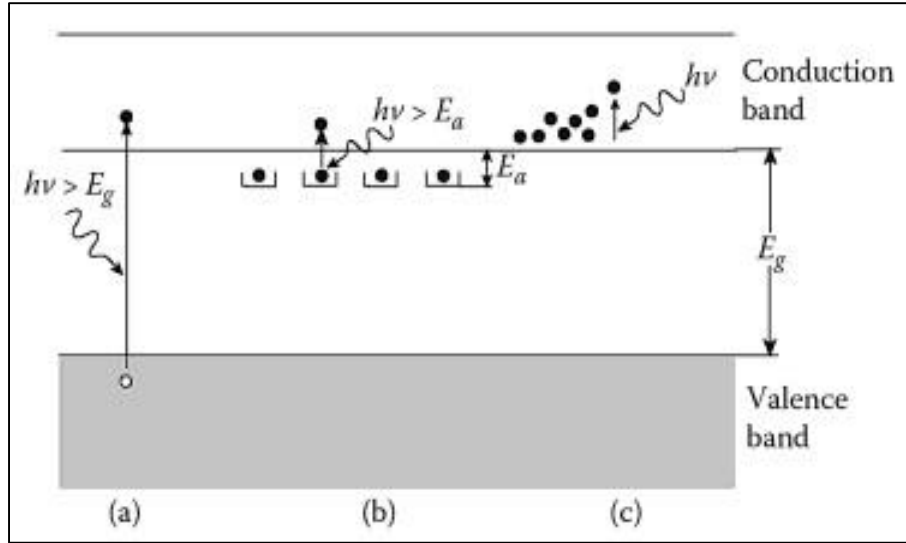
Fig 1-4: The fundamental optical excitation processes in semiconductors: (a) intrinsic absorption, (b) extrinsic absorption, and (c) free electron absorption. From Rogalski [1].
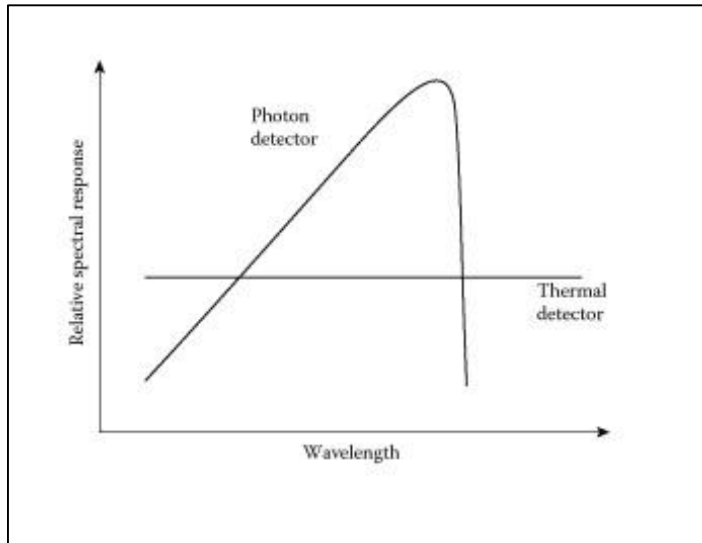
Fig 1-5: Spectral response for a photon and thermal detector. From Rogalski [1]

thermal generation of charge carriers [1]. Non-cooled detectors can be very noisy as thermal generation of free carriers competes with photonic generation. A comparison of D* for some commercially available IR detectors is shown in Fig 1-6.
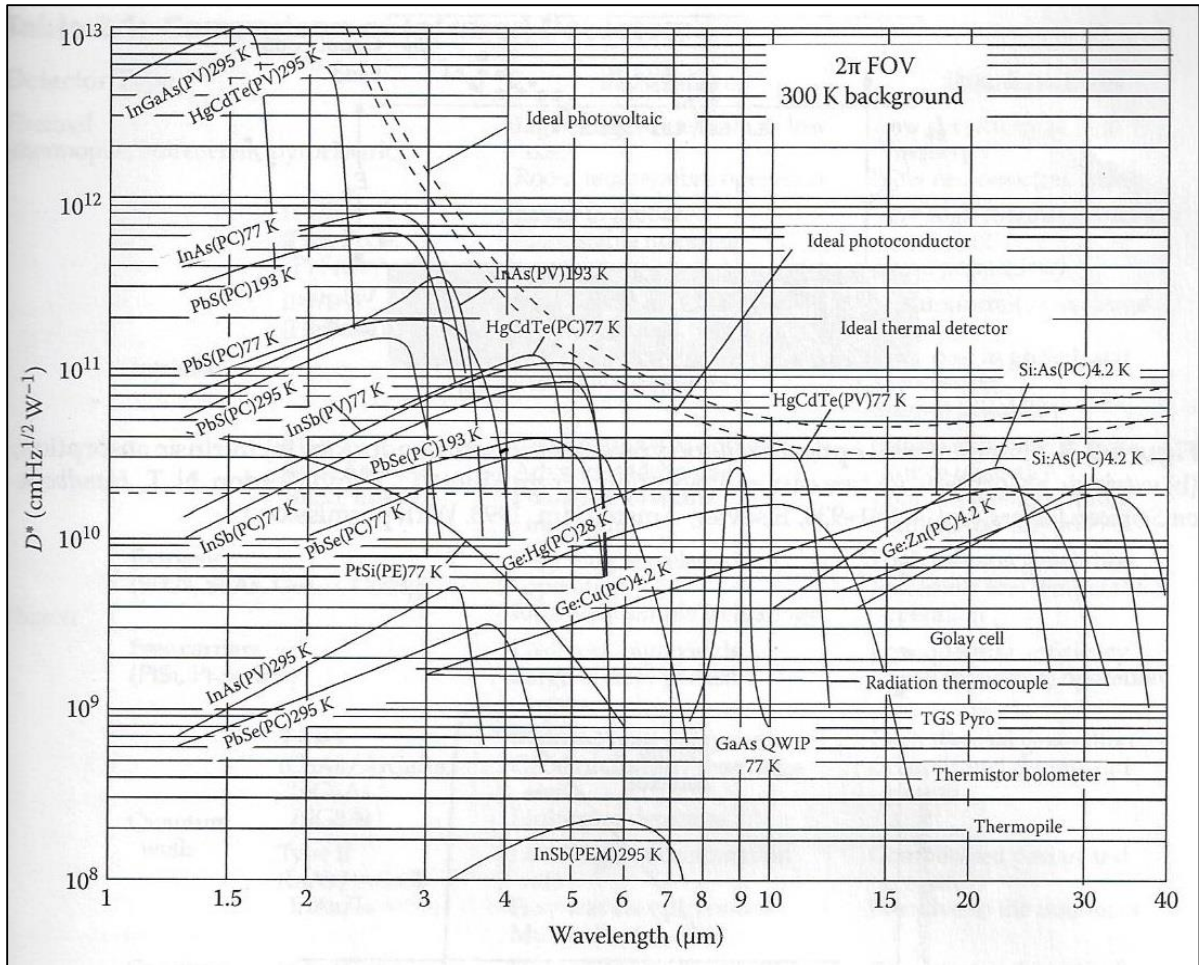
Fig 1-6: D* for various commercially available IR detectors operating at the indicated temperature. The chopping frequency is 1 kHz for all detectors except the thermopile (10 kHz), thermocouple, thermistor bolometer, pyroelectric detector, and Golay cell (10 Hz). The theoretical curves are the background-limited D* (dashed lines) for ideal devices. From Rogalski [1]

Note the cold operating temperatures and the frequency dependent D*s for the photon detectors and the frequency independent D*s for the thermal detectors. The dashed lines are the theoretical performance curves for ideal detectors. A detector is considered to be ideal if it achieves background limited detection (a.k.a. background limited infrared photodetector – BLIP). BLIP means that the performance of the detector, as defined by its SNR, responsivity, detectivity, specific detectivity, and field-of-view, is limited only by background thermal

13

radiation (not electrical noise from the detector itself). In other words, background radiation is the limiting noise source. This assumes that the background radiation intensity fluctuates outside the bandwidth of any post-detection electronic filter circuit.

The types of thermal detectors that have found the greatest utility in infrared technology are bolometers (thermistors), pyroelectric detectors, and thermoelectric detectors (thermocouples or thermopiles) [1], [30]. Bolometers and pyroelectric detectors have also found use in the detection of THz radiation, as have Golay cells, as stated in Section 1.2. In thermal detectors, the incident radiation is absorbed, thereby changing the characteristics of some temperature dependent material within the detector. As a result of this temperature change, some electrical property of the material is changed which is then detected by external circuitry.

A bolometer (thermistor) is a resistive element constructed from a material with a very small thermal capacity and a large temperature coefficient. Absorption of thermal radiation produces a large change in resistance which is detected by an external circuit. A pyroelectric detector uses a pyroelectric crystal that undergoes a change in internal electrical polarization when a change in temperature occurs (i.e. when thermal radiation is absorbed). The polarization change is then detected as a change of capacitance by an external circuit. Thermoelectric detectors work because of the Seebeck effect. At the junction of two dissimilar metals, a voltage is generated by a change in temperature which is detected by an external circuit. Thermocouples and thermopiles are common thermoelectric detectors. A Golay cell is an opto-acoustic detector consisting of a gas filled enclosure with an infrared absorbing material and a flexible membrane. Incident THz or IR radiation is absorbed by the material thereby heating the gas. The gas expands resulting in an increase in pressure which deforms

14

the membrane. The membrane's deformation is detected optically which results in a signal to external circuitry.

The response in thermal detectors does not depend on the photonic nature of the incident radiation so the responsivity of thermal detectors tends to be wavelength independent [1]. This is shown in the ideal-case curves of Fig 1-5 and Fig 1-6. The output signal depends on the incoming radiative power, not on the spectral content. Because of this, the spectral response of a thermal detector is usually very broad. Thermal detectors are typically operated at room temperature and are generally characterized by a modest sensitivity and a relatively slow response. They are generally cheaper and easier to use than photon detectors. As interesting as they are and as widespread as they have become, we will not be looking at thermal LWIR detectors in this study. This dissertation is concerned with improving the performance of LWIR photon detectors only.

One popular type of LWIR photon detector is made from HgCdTe. HgCdTe is a ternary compound semiconductor and has been used in both photoconductor (1st generation devices) and photodiode (2nd generation devices) detectors [32]. It is the only common material that can detect IR radiation in multiple atmospheric windows (SWIR: $\lambda = 1.5$ to 1.8 μm and $\lambda = 2.2$ to 2.4 μm, MWIR: $\lambda = 3$ to 5 μm, and LWIR) [33]. In fact, HgCdTe is the result of a deliberate engineering effort to create a tunable direct bandgap, intrinsic semiconductor with a high absorption coefficient for use in the IR. The bandgap of $Hg_{1-x}Cd_xTe$ is adjustable from $\lambda = 0.7$ μm to $\lambda = 25$ μm [32]. It is controlled by varying x, the composition ratio of CdTe to HgTe. For LWIR operation, $Hg_{0.8}Cd_{0.2}Te$ (x = 0.2) is used. Direct bandgap materials have a sharp onset of optical absorption, unlike thermal detectors. Strong optical absorption in the LWIR (10^2 to 10^3 cm^{-1} [34]) allows HgCdTe detectors to absorb a high percentage of radiation while

keeping device thicknesses very small (10-20 microns) [32]. Minimizing detector thickness helps minimize volume which mitigates both thermal and carrier generation-recombination noise.

HgCdTe is an intrinsic semiconductor, so electron-hole pairs are created for each absorbed photon that exceeds the band-gap energy. The electrons and holes are then collected by suitable readout integrated circuits (ROICs) and transformed into an electrical signal. The fabrication of 2D arrays of HgCdTe detectors on a single substrate is called a "focal plane array" (FPA) [33]. Because of the intrinsic absorption process, HgCdTe detectors can be fabricated with small detector volume, so tend to have a much higher detection speed and higher sensitivity than thermal detectors.

HgCdTe has many other advantages including: very high electron mobility ($\mu_e \sim 10^5$ $cm^2/V \cdot s$ for $Hg_{0.8}Cd_{0.2}Te$ at T = 80 K), long ballistic length (mean free path can be several microns at T = 80 K), moderate dielectric constant, and moderate thermal coefficient of expansion (TCE) relative to competing detector materials [32], [33]. HgCdTe can be grown in bulk or epitaxially using processes such as liquid phase epitaxy and vapor phase epitaxy [32]. The static and high frequency dielectric constants for $Hg_{0.8}Cd_{0.2}Te$ from 77 K to 300 K are $\varepsilon_0 = 13.0$ and $\varepsilon_\infty = 17.8$ respectively [35]. These values are low relative to PbSnTe - a leading competitive material. The static dielectric constant for PbTe is $\varepsilon_0 \approx 400$ and for SnTe is $\varepsilon_0 \approx 1700$ [32]. Higher dielectric constants create higher device capacitances and longer RC time constants. Scanned images then smear in the scanned direction if the device response is too slow [32]. Thus, HgCdTe is a superior material to PbSnTe for FPA-based imaging systems.

A cross-section of an HgCdTe photoconductor is shown in Fig 1-7. Anti-reflective (AR) coatings are used because HgCdTe has a refractive index of approximately n = 4. Much of the incoming IR would be reflected away from the detector without the AR coating. Unfortunately, the AR coating absorbs some of the incident radiation thus attenuating the radiation power received by the detector.

Traditionally, LWIR detectors have been used for thermal night-vision applications [1]. These applications have been driven primarily by military and national security interests. The extent of the requirements for these applications is detection of LWIR radiation and the
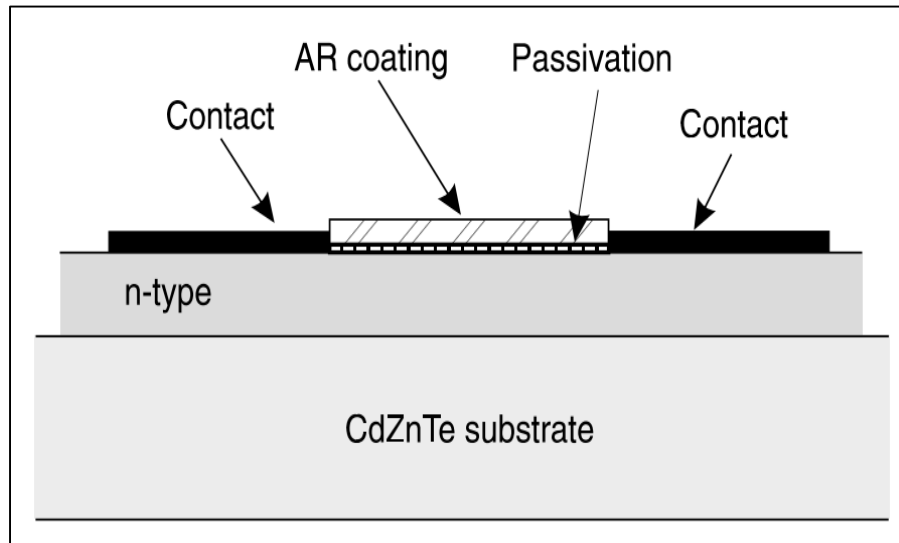
Fig 1-7: Cross-section of a basic HgCdTe photoconductor. The n-type layer is HgCdTe, 10 microns thick. Passivation is an anode oxide. AR coating is ZnS. From Norton [32].

formation of IR images from temperature contrast and emission differences. This has been done in systems for recognition and surveillance, tank sighting systems, anti-tank missile guidance, air-to-air heat seeking missile guidance, and satellite imaging [1], [32]. Further, HgCdTe has been used by NASA and NOAA for LWIR detection in a variety of earth satellite missions [32]. NOAA atmospheric sounders based on the absorption edge of the $\lambda = 14\ \mu m$

CO₂ band, have used HgCdTe photoconductors operating at 90 K since the 1980s [32]. The Moderate Resolution Imaging Spectrometer (MODIS) is a FPA covering spectral bands from visible to LWIR. Its six longest wavelength bands use HgCdTe photoconductors operating at 90 K [32].

Second-generation HgCdTe devices using photodiodes have been used to construct two-dimensional FPAs. A cross-section of a HgCdTe photodiode is shown in Fig 1-8. Second-generation photodiodes are used in scanned IR imaging systems and staring array configurations. FPAs exceeding 1024 x 1024 elements are common, and the IR astronomy application drives even larger staring arrays [32].
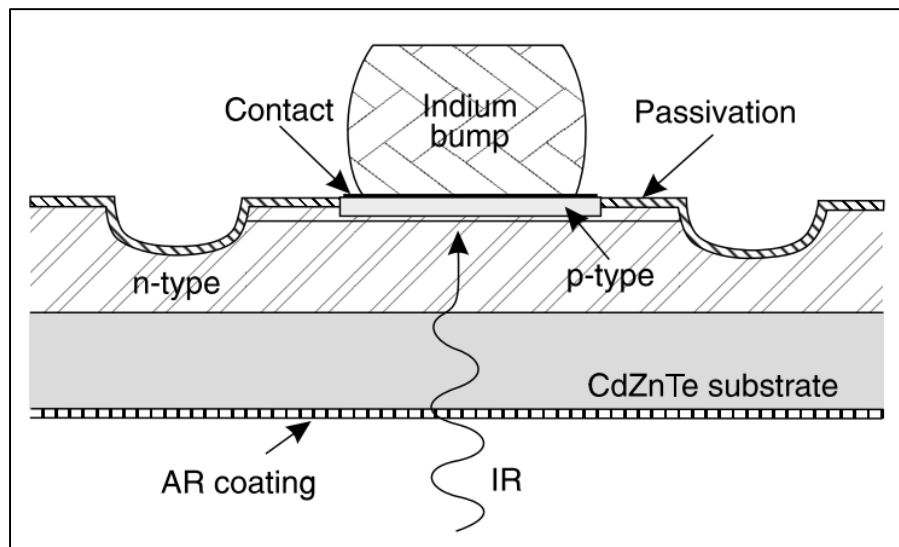
Fig 1-8: Cross-section of a basic HgCdTe photodiode. The n-type layer is HgCdTe, grown on the CdZnTe substrate, followed by a p+-type layer to form the junction. From Norton [32].

Third-generation devices based on HgCdTe are also being developed. These devices are basically photodiodes that have been substantially enhanced to provide more advanced capabilities such as two-color detection, avalanche photodiodes, and hyperspectral arrays [32].

In spite of their advantageous capabilities, there are challenges with detecting LWIR radiation using photon detectors. For HgCdTe photoconductors and photodiodes, dark currents are a major limiting factor in detector performance. Dark currents are internal currents that occur in photon detectors when the device is not being illuminated by light. They are caused by the random thermal generation of electrons and holes within the depletion region of the device. Any applied bias voltage will provide an electric field which then sweeps these carriers across the device junction generating "dark" currents. Dark currents are proportional to the area of the device's active region [30] so can be reduced by reducing this area. Thus, a reduction in device size is desirable. Unfortunately, by conventional optical coupling, reducing the device's size means reducing its optical cross-section, which leads to a lowering of the incident radiant flux absorbed. If a means could be found to reduce the device size while mitigating the reduction of absorbed radiant flux, meaningful improvements to detector performance could be achieved.

1.4. Using Surface-Plasmonic Structures to Improve THz and LWIR Detection

The performance of both THz detectors and LWIR photon detectors could be improved upon if the devices could capture more radiation per unit area. This study examines some passive optical structures (surface-plasmonic structures) that may be able to satisfy that desire. Through the interaction of incident radiation with periodic conducting structures, bound surface waves can be excited on the structures. These surface waves are coupled to the incident radiation and can enhance both the electromagnetic fields near the structure and the far field radiation transmitted through the structure. This phenomenon leads us into the field of surface-

plasmonics. Nevertheless, it must be mentioned that although detectors are a strong motivation for the research conducted here, the realization of detector improvement was not carried out.

This dissertation is organized into six chapters including this introduction. The second chapter will discuss extraordinary optical transmission (EOT) as a phenomenon that may be used to concentrate and filter incoming radiation. This can increase detector sensitivity and selectivity though a corresponding reduction in detector area. The theory and mechanism of EOT will be covered. The third chapter will discuss the use of numerical computation as a modeling and simulation tool to do desktop virtual experiments in physics and engineering. The finite element method (FEM) was used in this study. Therefore, the theory behind FEM and its mathematical underpinnings will be discussed. Two commercially available FEM software packages, HFSS and COMSOL will be also be discussed. The fourth chapter covers the simulations of THz wire-grid polarizers. Wire-grid polarizers are planar structures made of parallel conducting strips which are mounted on low loss dielectric substrates. The geometries of these wire-grid polarizers are subwavelength, meaning the geometry is much smaller than the wavelengths of the incident radiation. What was found in this research was that increasing a wire-grid polarizer parameter called the fill factor (to be defined in Section 4.2) increased the performance of wire-grids as polarizers while concentrating EM fields into smaller volumes. This was unexpected and novel. It opens the door to the possibility of improving the performance of a detector if it is physically positioned to exploit the high fill factor EOT phenomenon. The fifth chapter covers the simulations of a particular LWIR component, a plasmonic wire grating (PWG). The PWG is also a planar metallic structure mounted on a dielectric. Although not taken to this step in this dissertation, the dielectric will eventually be a LWIR photoconductive material or photodiode. The goal is to use PWGs to

create EOT thereby concentrating LWIR into a smaller area thus allowing for a reduction in detector area while maintaining strong radiation to detector coupling. The sixth and final chapter will summarize and conclude this dissertation.

2. The Theory of Extraordinary Optical Transmission

2.1. Definition of EOT

The first report of Extraordinary Optical Transmission (EOT) was in 1998 by Ebbessen et al in the visible and near-IR regions [36]. Ebbessen was investigating the optical characteristics of submicron holes in metallic films. He and his research group found that when these holes were organized into two dimensional (2D) periodic arrays, the structure exhibited an unusually high zero-order transmission spectra (zero-order meaning that the incident and transmitted light were collinear) in the near IR. The cause of this phenomenon was not diffraction since the wavelengths of the incident light were much larger than the periods of the arrays. Ebbessen noted that spectrally sharp transmission peaks were observed and that the transmission efficiency often exceeded unity when normalized to the area of the holes. The peaks were orders of magnitude larger than what would be predicted using standard aperture theory. Ebbessen coined this phenomenon Extraordinary Optical Transmission. Based upon Ebbessen's work, we will define EOT as – *The greatly enhanced transmission of light through a conducting film on which sub-wavelength apertures or other features have been patterned in a regular repeating periodic structure*.

There are three major parts to this definitions. First, EOT is a phenomenon of greatly enhanced light transmission. The amount of light transmitted (usually measured by the

transmission coefficient or transmittance) is much larger than what would be predicted using the theory of geometric optics. Bethe determined the transmission coefficient for light passing through a sub-wavelength cylindrical hole in a metal film in 1944 [37]. Using geometric optics, Bethe calculated that the transmission coefficient was proportional to the fourth power of the radius of the hole and inversely proportional to the fourth power of the wavelength of the incident radiation. This is shown in (2.1) where r is the radius of the hole and λ is the wavelength of the incident light.

$$T \propto \left(r/\lambda\right)^4 \tag{2.1}$$

Second, a conducting film is required. A conducting film is thin sheet of material that has a significant number of free charge carriers within it. Metals, highly doped semiconductors, transition-metal nitrides, or transparent conducting oxides (TCOs) [38] all qualify. There is not an exact number with which to quantify how many free charge carriers are required to support EOT. Nevertheless, the concentration of free charge carriers determine the plasma frequency of the material which is given by [39]

$$\omega_p = \sqrt{\frac{ne^2}{m\varepsilon_0}} \tag{2.2}$$

where n is the electron concentration, e is the electronic charge, m is the electron rest mass, and ε_0 is the permittivity of free space. EOT always occurs at frequencies below ω_p. At frequencies at or above ω_p the material becomes more dielectric in character, and thus more and more transparent with increasing frequency. Third, the apertures or features must be organized in a periodic structure or pattern. This organization can be a 2D hole pattern, as was used in Ebbessen's study, or it can be one-dimensional (1D) gratings [40], [41].

23

There are three physical mechanisms behind EOT: surface plasmon polaritons (SPPs or surface plasmons for short), waveguide modes, and structured surface plasmons (SSPs). Strictly speaking, 2D structures only support TM and TE waveguide modes; waveguide modes in 1D structures are similar to those that occur in parallel plate waveguides: TE, TM, and TEM depending on angle of incidence. Which mechanism is at work depends on the plasma frequency (wavelength) of the conducting film relative to the wavelength of the incident radiation, and the geometry relative to the wavelength of the incident radiation. Both SPPs and waveguide modes occur in periodic structures whenever the wavelength of the incident radiation is slightly greater than or equal to the period of the structure while SSPs are associated with subwavelength structures. SPPs are observed in the visible and IR regions. SPPs can be excited in the THz region but they are not locally confined and therefore are very weak [42]. Waveguide modes and SSPs occur throughout the electromagnetic spectrum. The SSP picture attempts to integrate both the SPP and the waveguide mechanisms into one overarching explanation of EOT. These concepts will be defined and discussed in the following sections.

2.2.   EOT due to Surface Plasmon Polaritons (SPPs)

SPPs are collective excitations created by the coupling of electromagnetic (EM) waves to free electrons in a conductor along a dielectric-conductor interface. At such an interface, it is possible to create surface waves with E-field components perpendicular to the interface in both media. These components will be directed towards and away from the interface, beginning and ending at charges on the interface. A qualitative diagram of this behavior is given in Fig 2-1; the arrow-tipped curves represent the electric lines-of-force. The E-field components normal to the interface decay with distance from the interface. Thus, these surface

modes are confined to the interface. Fig 2-2 illustrates the phenomenon with the +/- z direction corresponding to the direction perpendicular to the interface. From a physical point of view, an SPP mode corresponds to the coupling of the incident radiation to an oscillating surface charge density wave (SCDW). When conducting structures have periodically patterned
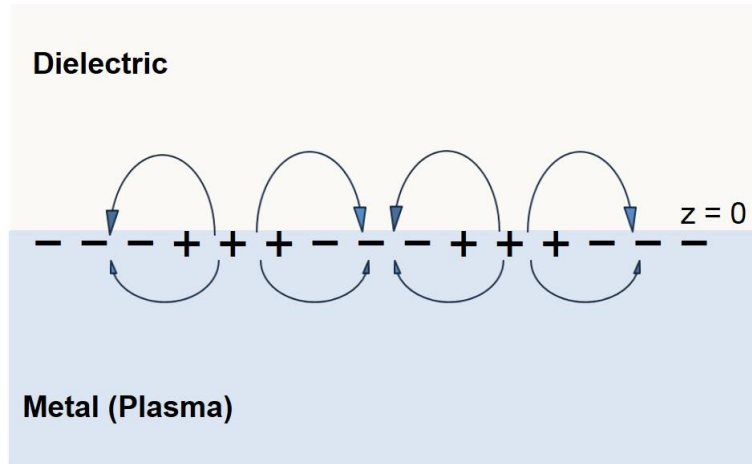
Fig 2-1: SPP modes can be represented by oscillating charge density waves at the dielectric-conductor interface. The interface is at $z = 0$.
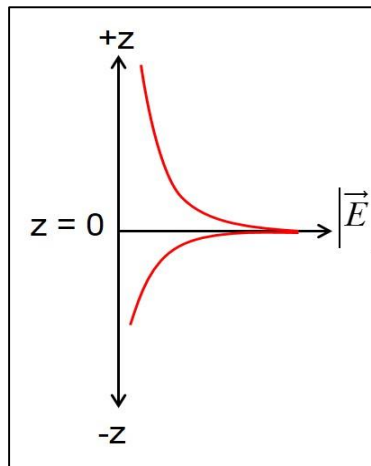
Fig 2-2: The magnitude of the normal component of the electric field associated with a SPP exponentially decays in the direction perpendicular to the dielectric-conductor interface.

apertures, the geometry can create SPP resonant frequencies at which the EM-wave-to-electron interaction is particularly strong. This resonant phenomenon greatly enhances local EM fields in and around the apertures. In fact, the electromagnetic energy is highly concentrated within the apertures during resonance. The apertures themselves then act like short electric dipole radiators. They become strong sources of electromagnetic re-radiation which are coupled to the incident radiation. The energy in these apertures is radiated out the opposite side of the structure and thereby creates the observed EOT phenomenon.

Let a plane EM wave, with its electric field parallel to the x-axis, be incident on an air (dielectric)-metal (conductor) interface with the interface at z = 0 as shown below in Fig 2-3.
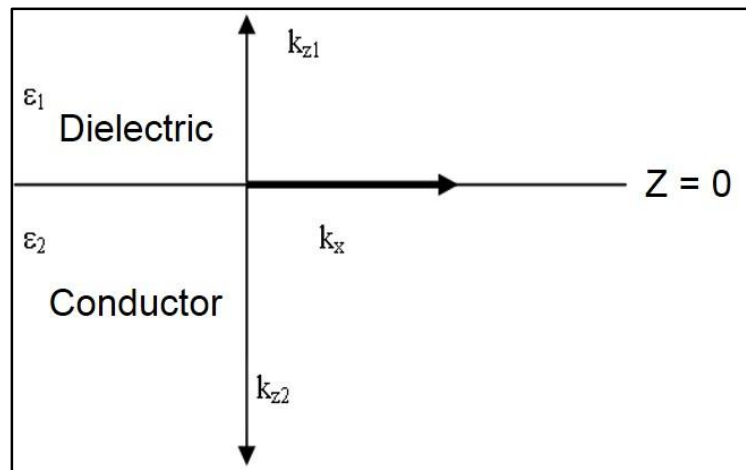
Fig 2-3: Interface between a dielectric and a conductor at z = 0. Arbitrary units are used.

Since most materials are non-magnetic ($\mu = \mu_0$), it is the discontinuity of the electric permittivity across the interface which determines the behavior of the radiation at the interface. To elucidate the physics of this situation, Maxwell's Equations are applied [43]. Here we view the metal as a highly polarizable dielectric (see Section 4.1), a valid assumption for $\omega \lesssim \omega_p$ [44]. Maxwell's Equations in matter without source terms are given below in Eqs. (2.3) –

(2.6). The boundary conditions for the electric and magnetic fields and the continuity requirement for the wavevector $\vec{k}$ are given in Eqs. (2.7) – (2.11).

Gauss's Law for $\vec{D}$ $\qquad\qquad\qquad$ $\nabla \cdot \vec{D} = 0$ $\qquad\qquad\qquad\qquad\qquad$ (2.3)

Gauss's Law for $\vec{B}$ $\qquad\qquad\qquad$ $\nabla \cdot \vec{B} = 0$ $\qquad\qquad\qquad\qquad\qquad$ (2.4)

Faraday's Law $\qquad\qquad\qquad$ $\nabla \times \vec{E} = -\dfrac{\partial \vec{B}}{\partial t}$ $\qquad\qquad\qquad\qquad\qquad$ (2.5)

Ampere's Law $\qquad\qquad\qquad$ $\nabla \times \vec{H} = \dfrac{\partial \vec{D}}{\partial t}$ $\qquad\qquad\qquad\qquad\qquad$ (2.6)

$E_{\parallel}$ continuous $\qquad\qquad\qquad$ $E_{x1} = E_{x2}$ $\qquad\qquad\qquad\qquad\qquad$ (2.7)

$H_{\parallel}$ continuous $\qquad\qquad\qquad$ $H_{y1} = H_{y2}$ $\qquad\qquad\qquad\qquad\qquad$ (2.8)

$D_{\perp}$ continuous $\qquad\qquad\qquad$ $D_{z1} = \varepsilon_1 E_{z1} = \varepsilon_2 E_{z2} = D_{z2}$ $\qquad\qquad\qquad\qquad\qquad$ (2.9)

$B_{\perp}$ continuous $\qquad\qquad\qquad$ $B_{z1} = B_{z2}$ $\qquad\qquad\qquad\qquad\qquad$ (2.10)

Continuity of k $\qquad\qquad\qquad$ $k_{x1} = k_{x2} = k_x$ $\qquad\qquad\qquad\qquad\qquad$ (2.11)

The instantaneous boundary conditions state that the tangential component of the electric field and the normal component of the magnetic flux density are continuous at the interface, Eqs. (2.7) and (2.10). Eq. (2.9) states that the normal component of the electric displacement field is continuous across the boundary, but the electric field is not. This discontinuity is caused by the change in electric permittivity from medium 1 (air) to medium 2 (metal). It implies that "bound" (polarization) surfaces charges are present at the interface. However, there are no "free" (source) surface charges present, see Eq. (2.3). The final boundary condition, Eq. (2.8), states that the tangential component of the magnetic field is

27

continuous across the interface. This implies that there are no "free" (source) surface currents; there is no source current term in Eq. (2.6). There are of course "bound" (polarization) currents. Since normal $\vec{D}$ is continuous, then by the curl operation in Eq. (2.6), so must tangential $\vec{H}$ be continuous. The continuity conditions for $\vec{k}$, in Eq. (2.11), are due to the conservation of energy.

The following trial solutions for the electric and magnetic fields, Eqs. (2.12) – (2.15), will satisfy Maxwell's Equations with the above boundary and continuity conditions [44].

$z \geq 0$ (dielectric):
$$\vec{E}_1 = \langle E_{x1}, 0, E_{z1} \rangle e^{i(k_x x - \omega t)} e^{ik_{z1} z} \tag{2.12}$$

$$\vec{H}_1 = \langle 0, H_{y1}, 0 \rangle e^{i(k_x x - \omega t)} e^{ik_{z1} z} \tag{2.13}$$

$z \leq 0$ (conductor):
$$\vec{E}_2 = \langle E_{x2}, 0, E_{z2} \rangle e^{i(k_x x - \omega t)} e^{ik_{z2} z} \tag{2.14}$$

$$\vec{H}_2 = \langle 0, H_{y2}, 0 \rangle e^{i(k_x x - \omega t)} e^{ik_{z2} z} \tag{2.15}$$

When these solutions are inserted into Maxwell's equations, and the boundary conditions applied, the dispersion relation can be calculated. Doing so yields (2.16)

$$k_x = k_{SP} = \frac{\omega}{c} \sqrt{\frac{\varepsilon_1 \varepsilon_2}{\varepsilon_1 + \varepsilon_2}} \tag{2.16}$$

where ε_1 is the relative permittivity of the dielectric (air) and ε_2 is the relative permittivity of the metal. The relative permittivity of air is simply unity:

$$\varepsilon_1 = 1 \tag{2.17}$$

On the other hand, real metals are lossy. Therefore, the relative permittivity of the metal is a complex number of the form:

28

$$\varepsilon_2 = \varepsilon'_2 + i\varepsilon''_2 \tag{2.18}$$

In addition, both the real and imaginary parts of the relative permittivity are dispersive, meaning that their values vary with frequency. This is shown in Fig 2-4 below.
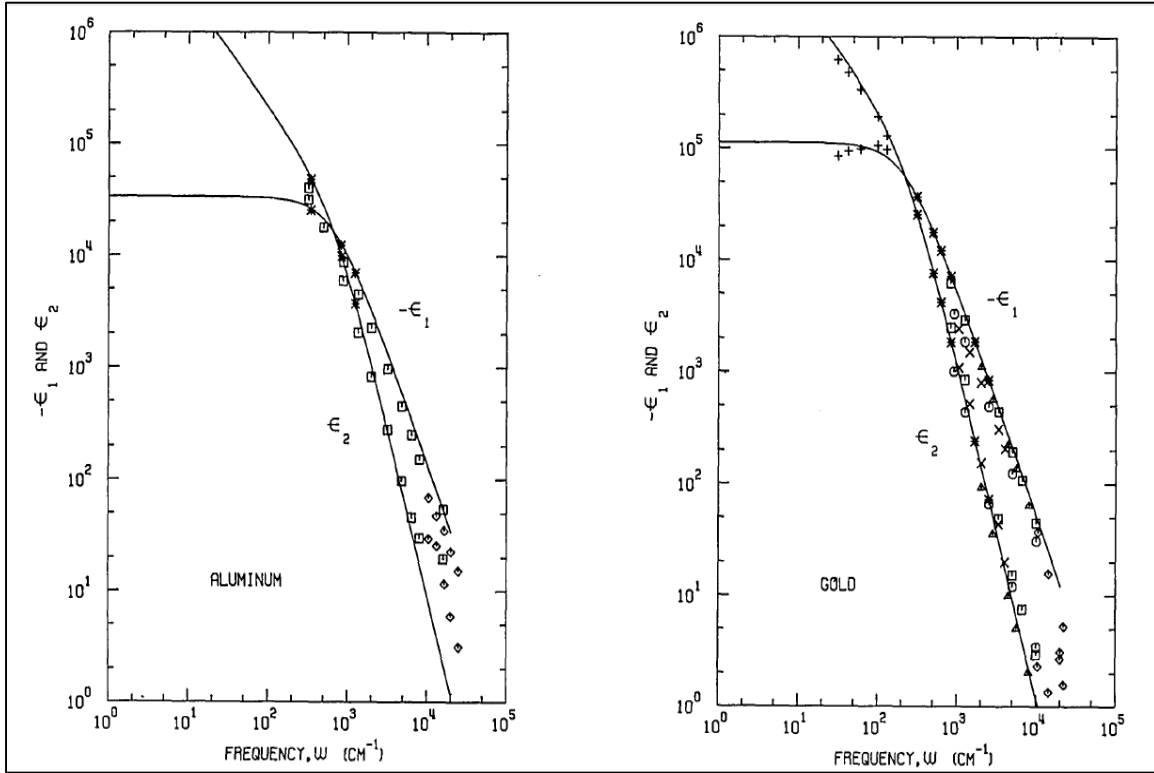
Fig 2-4: Frequency dependence of the real and the imaginary parts of the relative electric permittivity for aluminum (left) and gold (right). Solid line is the Drude model, points are measured data. From Ordal [45].

Below the metal's plasma frequency, the real part of its relative permittivity will be large and negative, $\varepsilon'_2 < 0$ and $|\varepsilon'_2| \gg \varepsilon_1$ (these conditions hold in the LWIR and THz regions). This behavior of ε_1 and ε_2 has the following effects. First, since ε_2 is complex, the wavevector for the surface plasmons will also be complex as shown in (2.19)

$$k_{SP} = k'_{SP} + ik''_{SP} \tag{2.19}$$

29

Second, the value under the radical sign in the dispersion relation, (2.16), will always be greater than unity. Therefore, the real part of the surface plasmon wavevector will be larger than the wavevector of the incident light (the light line).

$$k'_{SP} > k_0 = \frac{\omega}{c} \tag{2.20}$$

(2.20) asserts that there is a momentum difference between a surface plasmon wave and the incident light. Surface plasmons carry more momentum than light. In order for SPPs to be excited, the momentum difference must be matched. The final result from the SPP solution is that k_{z1} and k_{z2} must be imaginary [44]. Therefore, the components of the surface plasmon waves that are perpendicular to the interface decay exponentially with distance z. The dispersion relation for a surface plasmon wave is plotted in Fig 2-5.

One observation from the dispersion relation is that as k'_{SP} increases so does the deviation of the surface plasmon dispersion curve from the light line. This means that as k'_{SP} increases the surface plasmons become increasingly localized at the air-metal interface. In other words, they become more confined to the surface as the frequency of the incident light increases (wavelength decreases). Surface plasmons propagate along the surface more efficiently as k'_{SP} increases.

A propagation length can be defined for surface plasmons. The propagation length is the distance along the surface that SPPs can travel before their intensity decreases by a factor of 1/e. The propagation length is given by Ebbesen et al [46]:

$$l_{SP} = \frac{1}{2k_{SP}} = \frac{2}{(k_{SP}')^3} \frac{(2\pi\varepsilon_2')^2}{\lambda^2 \varepsilon_2''} \tag{2.21}$$

30
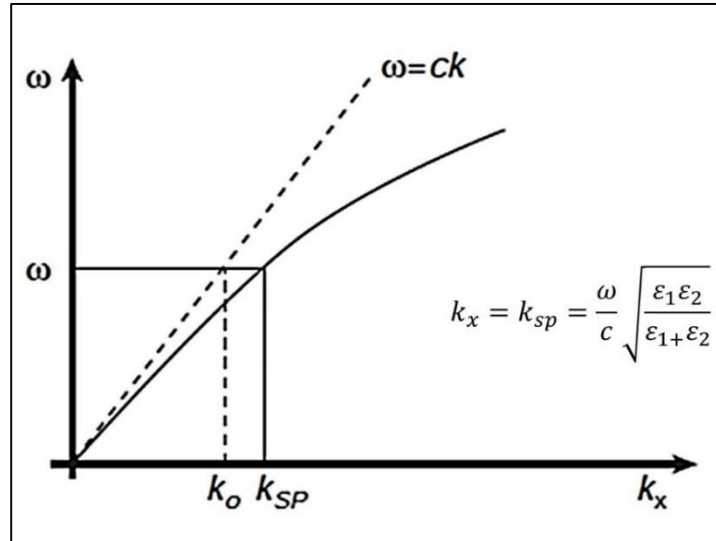
Fig 2-5: Dispersion relation for a surface plasmon wave. k_0 is the wavevector for light. k_{SP} is the real part of the wavevector for the surface plasmons. $\omega = ck$ is the light line. Plots from Barnes et al [47].

(2.21) asserts that propagation length decreases rapidly with increasing k'_{SP}. This is due to the increasing resistive damping effects in lossy metals for shorter wavelengths [46]. Therefore, even though surface plasmons become more confined with increasing k, they propagate shorter distances. Fig 2-6, shows this contrasting behavior. The intersection of the dispersion curve and the propagation length curve can be considered a "sweet spot" for SPP generation. For most metals, this "sweet spot" is in the visible region.

31
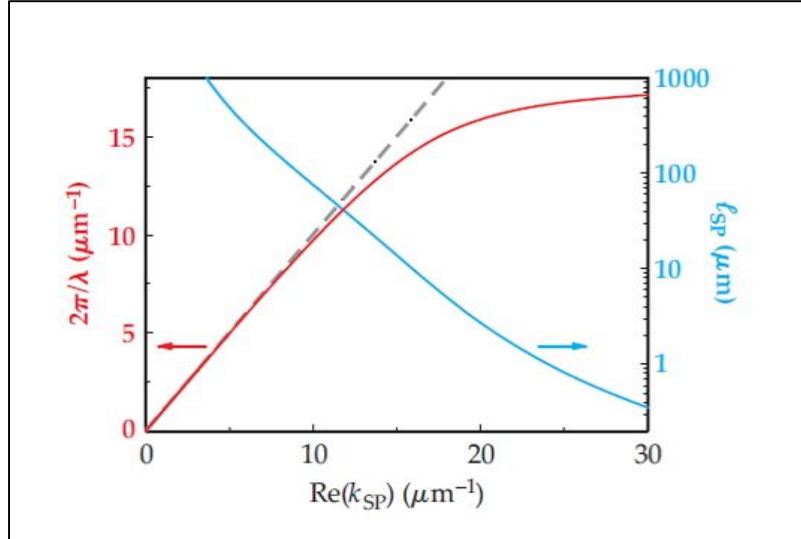
Fig 2-6: Dispersion relation (red) and propagation length (blue) of surface plasmon on a planar air-gold interface. Plots from Ebbesen [46].

2.3.   Methods for Generating SSPs

Attenuated Total Reflection (ATR) – the geometry for the ATR methods are shown in Fig 2-7. ATR is used to excite SPPs in the visible and IR regions. Panel (a) shows the Otto geometry, first demonstrated in 1968 [48]. In the Otto geometry, a prism is separated from a conducting metal by an air gap of less than a few wavelengths. The gap provides an electromagnetic tunnel barrier across which the radiation couples. The radiation is incident on the prism and is refracted. The radiation propagates through the prism until reaching the bottom side at angle of incidence θ_i. If this angle of incidence is greater than the critical angle ($\theta_i > \theta_c$), total internal reflection will take place inside the prism. Under these conditions, an evanescent field will form in the air gap. As long as the bottom surface of the prism is not too far from the top surface of the metal, radiation will couple across the gap and excite SPPs on the metal's surface. This occurs because the evanescent field has momentum in the x direction, which is greater than the momentum of any light that could propagate in the gap. Since [44]

32

$$\sin\theta_i > \sin\theta_c = n_2/n_1 \qquad (2.22)$$

then [44]

$$n_1 \hbar k \sin\theta_i > n_2 \hbar k \qquad (2.23)$$

Radiation incident at the bottom of the prism beyond θ_c produces more momentum along the surface of the metal than can be supported by the air. This excess momentum

$$\Delta p = n_1 \left(\sin\theta_i - \sin\theta_c\right)\hbar k \qquad (2.24)$$

provides the coupling to excite SPPs. Varying the angle of incidence of the P-polarized radiation at the prism-air interface varies the momentum in the x direction and thus allows for tuning of the device.
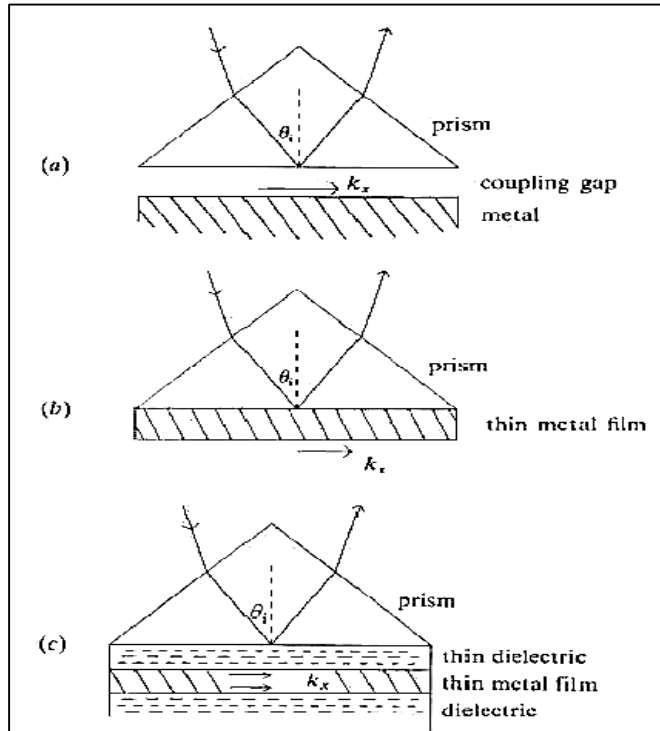
Fig 2-7: Geometry for generating SPPs using the ATR method. From Sambles et al [44].

33

The main weakness of this scheme is the air gap. The device's performance is very sensitive to the spacing as coupling strength varies with coupling gap. To make the method more robust, Kretschmann and Raether (K-R) eliminated the air gap altogether using the metal itself as the evanescent tunnel barrier [49]. A thin film (thickness < 50 nm) of metal was coated onto the bottom surface of a prism. Surface plasmons were then excited on the bottom side of the metal film. Fig 2-7 panel (b) shows the K-R geometry. The weakness of the K-R scheme is that the spacing between the prism and the metal surface on which the SPPs propagate is fixed by the metal film thickness. Once the coating is applied, no adjustments can be made. Fig 2-7 panel (c) shows a hybrid geometry that uses a thin dielectric spacer between the bottom surface of the prism and the thin metal film. This design provides an adjustment mechanism to the K-R method. One advantage of the ATR method over the others is that it can excite SPPs on non-periodic conducting surfaces.

1D Periodic Arrays – 1D periodic arrays also provide a coupling method for excitation of SPPs. 1D periodic arrays are often referred to as plasmonic wire gratings (PWGs) in the literature. PWGs can operate either in reflection or transmission. The geometry of these devices is shown in Fig 2-8 where the incident radiation has transverse magnetic (TM) polarization with respect to the plane of incidence or perpendicular (s) polarization with respect to the grating axis. Note that SPPs only exist for TM incident polarization on PWGs [42].

In this dissertation, we only study the responses from transmission gratings, Fig 2-8 panel (b). In transmission gratings, the slits at the grating surface break the translational invariance of the interface. SPPs are excited by incident radiation as long as momentum is matched.
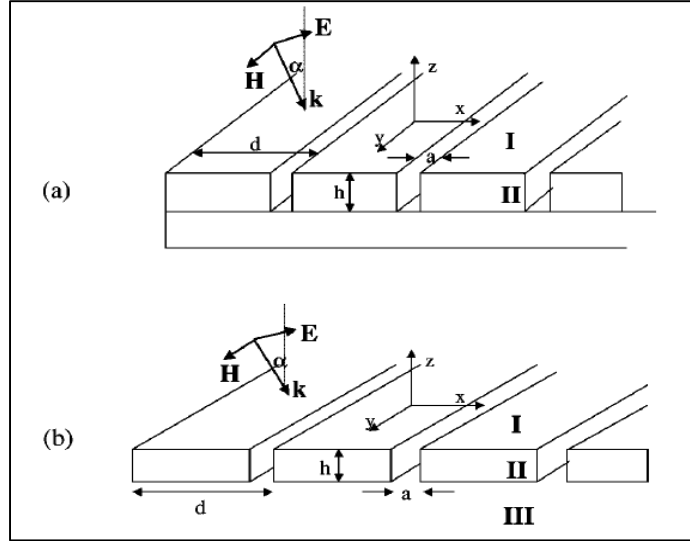
Fig 2-8: 1D grating couplers: (a) reflection gratings with period d, grove width a, and groove depth h. (b) Transmission grating with period d, slit width a, and thickness h. From Garcia-Vidal and Martin-Moreno [40].

Momentum matching occurs if the following relation is satisfied.

$$k_{SP} = k_0 \sin\theta \pm nG \tag{2.25}$$

where k_0 is the wavevector of the incident radiation, θ is the angle of incidence, n = (1, 2, 3…), and G = 2π/d is the reciprocal vector of the grating.

PWGs have several advantages over ATR devices. First, they allow for direct coupling of SPPs, no tunneling occurs so the interaction is stronger. Second, PWGs do not usually require as much space as ATR devices and therefore are more amenable to nanoscale applications. Third, PWGs have no film or spacer thickness constraints.

Coupling strength in PWGs is highly dependent on groove or slit depth h. Finally, for groove depths greater than or equal to one half a wavelength (h $\geq$ λ/2) waveguide modes develop (see Section 2.4). This is true even when the groove width $a \ll \lambda/2$. In a PWG, there

can always be a propagating TEM mode in the groove or slit. There are no cutoff wavelengths for TEM modes (there are for TM and TE modes) [40]. Through their support of waveguide modes, PWGs provide a second mechanism for EOT generation besides SPPs.

2D Periodic Hole Arrays − 2D periodic hole arrays provide the third method for exciting SPPs. An example of a 2D hole array is shown in Fig 2-9. We will not be covering 2D holes arrays in this dissertation except to comment that SPPs will be excited on the surface of a 2D hole array for radiation at normal incidence when the following relation is satisfied [50]

$$\lambda\sqrt{m^2 + n^2} = a\sqrt{\frac{\varepsilon_1\varepsilon_2}{\varepsilon_1 + \varepsilon_2}} \tag{2.26}$$

where λ is the wavelength of the incident radiation, m and n are integers, a is the array period (symmetric in x and y), and ε_1 and ε_2 are the relative permittivities of the dielectric (air) and the conductor (metal) respectively. 2D hole arrays also support TE and TM waveguide modes. But unlike TEM modes, which do not have cutoff wavelengths, TE and TM modes have cutoff wavelengths. Therefore, 2D hole arrays will have cutoff wavelengths beyond which propagation ceases. In addition, all modes in a 2D hole array cavity will become evanescent for hole diameters (d) smaller than one half a wavelength ($d < \lambda/2$)) [40].
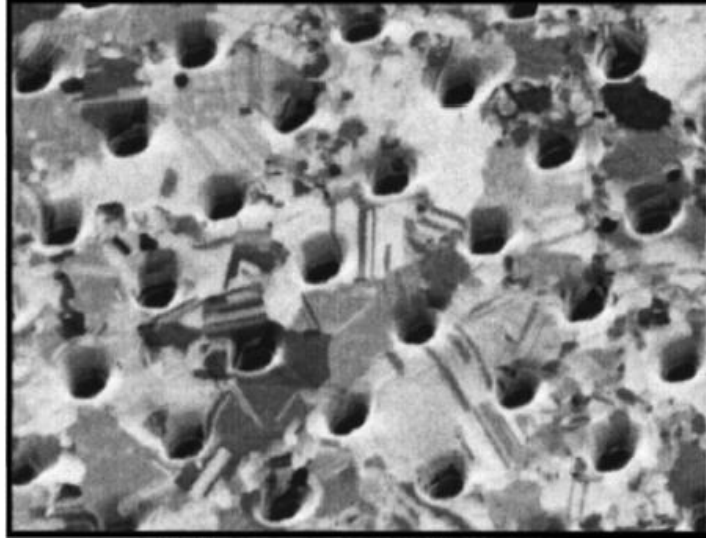
Fig 2-9: Focused ion beam image of a 2D hole array in a polycrystalline silver film. From Ghaemy et al [50].

2.4.   EOT due to Waveguide Resonances

Waveguide modes can develop in 2D and 1D structures respectively. Unlike SPPs, strong waveguide resonances can occur in both the THz and the IR regions whenever the wavelength of the incident light is larger than the period in a 1D grating coupler or a 2D hole array, and the metal is thick enough to support waveguide modes in the apertures but not too thick such that the modes are strongly absorbed by attenuation in the conductor.

As stated earlier, 1D gratings support the same type of waveguide modes as parallel plate waveguides: TE, TM, and TEM modes. Plots of these modes are given in Fig 2-10. The TEM mode can occur as long as the electric field vector is normal to the surface of the slit wall (TM polarization of a normally incident wave) but not when it is tangent to the slit wall (TE polarization of a normally incident wave). This is shown in Fig 2-10 (b) and (d). The TEM mode has a cutoff frequency of DC so it will always propagate. TE and TM modes occur when

the incident radiation is oblique to the grating surface and do have cutoffs frequencies. Therefore, they do not always propagate.
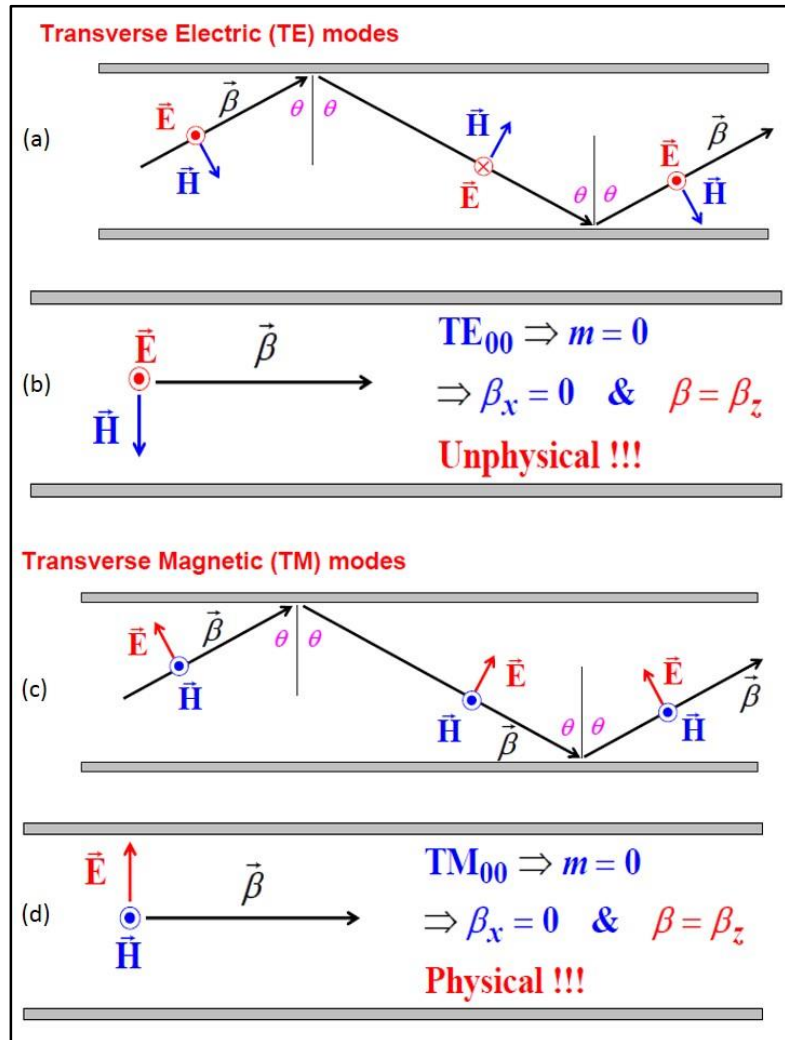
Fig 2-10: Possible propagation modes in a parallel plate waveguide and in a 1D grating structure from the solution of Maxwell's equations: (a) TE, (b) TE_{00} which exists mathematically but not physically, (c) TM, and (d) TM_{00} which is actually transverse electromagnetic (TEM). From Amanogowa.com [51].

A very good description of waveguide modes in 1D grating structures in the IR region is given by Porto et al [52]. Porto shows that resonances in IR transmission gratings are due to the excitation of two types of EM mechanisms: SPPs and waveguide modes. The type of

resonance that is excited depends on the relationship between the geometry of the grating, the wavelength of the incident radiation, and the angle of incidence of the incident radiation. These two types of resonances have also been reported by Garcia-Vidal and Martin-Moreno in the IR [40] and were seen in simulations performed in the IR region during this dissertation research. These results will be discussed in Sections 5.2 and 5.3.

As previously stated, SPP resonances can occur in 1D gratings in the visible and IR regions if $\lambda \cong d$ while waveguide resonances occur if $\lambda > d$ (d is the grating period). In addition, SPP resonances require a minimum slit width ($a > a_{min}$) while waveguide resonances only require a nonzero slit width ($a > 0$). Further, waveguide resonances require a minimum metal thickness ($h > h_{min} \cong \lambda/2$) while SPP resonances only require a nonzero thickness ($h > 0$). Higher order waveguide resonances may be excited depending on whether $h \gg \lambda/2$. The condition for a waveguide resonance to occur is given by [53], [54]

$$\lambda_N \lesssim \frac{2h}{N} \tag{2.27}$$

where N is the resonance order. Note that the approximation sign is necessary because the actual resonance wavelength is red-shifted by standing wave distortion at the two slit ends (fringing effects) [53]; h must be slightly greater than the free-space wavelength divided by two for Nth order. SPP resonances have a strong dependence on the angle of incidence while waveguide resonances do not as TEM modes occur at normal incidence and TM or TE modes occur at oblique incidence.

An excellent graphical representation of some of this behavior is given by Porto and is reproduced in Fig 2-11 below. The top panel (no letter label) shows the geometry of a 1D

transmission grating on a substrate and defines geometric parameters d (grating period), a (slit width), and h (grating thickness).

Panel (a) shows the calculated zero-order transmission versus wavelength at normal incidence for three different grating thicknesses (h = 0.2, 0.6, and 1.2 μm), while parameters d = 3.5 μm and a = 0.5 μm are held constant. Two sharp resonances are seen. They cannot be
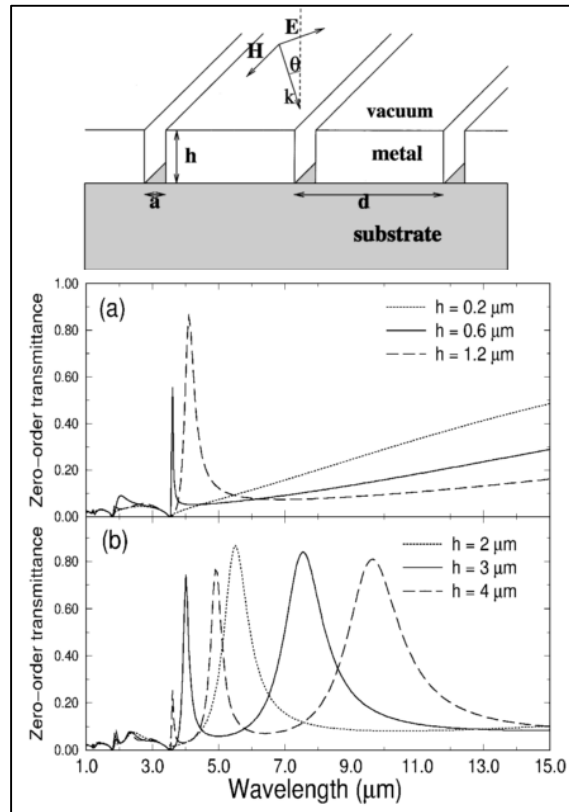
Fig 2-11: Schematic view of a 1D transmission grating. (a) Calculated zero-order transmission versus wavelength for grating thickness h = 0.2, 0.6, and 1.2 μm. (b) Calculated zero-order transmission versus wavelength for h = 2, 3, and 4 μm. From Porto et al [52].

waveguide resonances since (2.27) is not satisfied here (h is too small). They can be SPP resonances, since these occur whenever $\lambda \cong d$ for any nonzero value of h. An indeed Porto identifies them as such. These resonances are asymmetric in shape and indicative of Fano

40

resonances [41]. As the wavelength is increased, zero-order transmission increases monotonically. No waveguide resonances are observed in panel (a). This behavior is also reported by Huang [53].

Panel (b) shows the calculated zero-order transmission versus wavelength for h = 2, 3, and 4 μm, d = 3.5 μm, and a = 0.5 μm (again normal incidence). This time (2.27) is satisfied. The SPP resonances are still present for $\lambda \cong d$ but here new resonances emerge for $\lambda > d$. These are TEM mode waveguide resonances. Their shapes are broad and symmetric relative to the shapes of the SPP resonances. Both types of resonances widen as the slit width is increased [53]. A summary of the geometry requirements for both SPP and waveguide resonances in a 1D transmission grating is given in Table 2-1.

Resonance Type	Wavelength	Slit Width	Grating Thickness	Incident angle dependence
SPP	$\lambda \cong d$	$a > a_{min}$	$h > 0$	Yes
Waveguide	$\lambda > d$	$a > 0$	$h > h_{min} \cong \lambda/2$	No

Table 2-1: Summary of the geometry requirements for various EM resonances in 1D transmission gratings.

2.5. Structured Surface Plasmons (SSPs) – A Comprehensive Picture

EOT is also observed in the microwave, millimeter wave, and THz regions [55], [56]. Yet in these regions, the mechanism for EOT is not SPP coupling, strictly speaking [53], [42]. In good conductors, a high concentration of free electrons ensures that well-confined SPPs can exist only for frequencies relatively close to the plasma frequency (ω_p). For metals, SPPs are well supported in the visible and near-infrared regions. In order to have SPP propagation on

the air-conductor interface, the SPP propagation constant must be larger than the electromagnetic (EM) wavevector ($k_{SP} > k_0$). As stated in a Section 2.2, this condition leads to decaying fields perpendicular to the air-metal interface. The amount of the confinement increases with increasing k_{SP} and decreases significantly for $\omega \ll \omega_p$, where k_{SP} approaches k_0 asymptotically. In the THz region, the SPP wavevector k_{SP} is approximately k_0 ($k_{SP} \approx k_0$) in metal conductors. This is because there is a very large negative real part of the complex relative permittivity ($|\varepsilon| \sim 10^5$) for metals at these frequencies. Thus, metals behave like perfect electrical conductors (PECs) in the THz region. There can be no E-fields inside PECs. A substantial field amplitude inside the conductor is necessary for providing the non-zero tangential E-field component which generates the oscillating spatial charge distribution at the conductor's surface. With no significant field penetration into the conductor, SPPs become highly delocalized. As a consequence, SPPs at THz frequencies are not confined to the conductor's surface and act like grazing incidence light fields extending over a great number of wavelengths into the dielectric space above the interface [42]. Fig 2-5 and Fig 2-6 show this behavior graphically.

The question may be asked has to how this increasing field penetration reconciles with the classical skin effect. The classical skin depth is given by

$$\delta = \frac{1}{\sqrt{\pi \sigma \mu f}} \tag{2.28}$$

where σ is the electrical conductivity, μ is the magnetic permeability, and f is the frequency. Examination of (2.28) would lead one to conclude that skin depth decreases with increasing frequency and therefore decreases with increasing wavenumber k meaning there should be less

field penetration into a conductor in the optical and infrared regions than in the THz region. However, as will be discussed at some length in Section 4.1, the conductivity itself is frequency dependent (and complex valued). Therefore, $\sigma = \sigma(\omega)$. Further, electrical conductivity is related to electrical permittivity by (4.35) and (4.36) where $\varepsilon = \varepsilon(\omega)$. Therefore skin depth is also a function of electrical permittivity and in fact can be written as [57]

$$\delta = \frac{1}{\text{Re}\left\{\sqrt{-k_0^2 \varepsilon_r}\right\}} \tag{2.29}$$

where k_0 is the free space wavenumber and ε_r is the complex valued relative permittivity. Looking back to Fig 2-4, we see that the real part of ε_r falls sharply with increasing wavenumber (increasing frequency). Therefore, the tendency of δ to decrease with increasing f (or k) is mitigated by its tendency to increase with the decreasing real part of ε_r. This effect becomes quite significant for $k \geq$ 1e3 cm^{-1} ($\lambda \leq$ 10 μm) where the effect from ε_r dominates the effect from f. This explains how field penetration can increase with increasing f (or k).

Therefore, we will only observe SPPs for frequencies at or above the IR. Nevertheless, at THz and lower frequencies SPP-like behavior can be created by the coupling of incident electromagnetic radiation to free electron oscillations on conducting surfaces that can generate evanescent modes [53]. In the literature this SPP-like behavior has been referred to as "spoof surface plasmons" [58], [59] and "designer plasmons" [42]. A grid of periodically spaced apertures in a metal (even a perfect conductor) film can support spoof plasmons when apertures and aperture periods are sub-wavelength, in other words $a < d < \lambda$ (a = aperture dimension, d = grid period, and λ = radiation wavelength). This contradiction, SPP-like behavior (spoof plasmons) observed at THz frequencies where strong SPPs cannot exist, still causes significant misunderstanding, confusion, and arguments in field of surface plasmonics [53].

43

What is certain is that free-electron oscillations plays a fundamental role in all surface plasmon phenomena. Recently, Huang and Peng published detailed studies [53] and [58] which show that the different mechanisms used to explain extraordinary light emission and interference in all periodic and non-periodic conducting structures (including perfect conductors) are really part of the same basic model which they call the structured surface plasmon (SSP) picture. Huang shows that the SSP picture bridges the gap between SPPs in the visible and infrared wavelengths, and spoof plasmons in the microwave, millimeter wave, and THz regions.

What follows is an explanation of the SSP picture given by Huang and Peng. Metals have free conduction electrons that move and oscillate easily on their surfaces in response to incident electromagnetic waves. The oscillating electrons are linearly accelerated back and forth by the incident radiation. Accelerating electrons radiate. Thus, secondary radiation is emitted from the surface of the metal. Yet, SPPs are bound surface modes that do not radiate. If SPPs are caused by oscillating charges, what happens to the radiation? This paradox may be explained as follows using Fig 2-12. Fig 2-12 panel (a) shows the generation of SPPs on a plane surface using the Otto geometry to couple the incident radiation. The "+" and "-" symbols represent instantaneous positive and negative charges (the negative charges move, the positive do not). A SCDW is generated as a result of electron oscillations. SPP modes are sinusoidal SCDWs with period d. Since

$$d = 2\pi/\mathrm{Re}\left(k_{SP}\right) < \lambda \tag{2.30}$$

the SPP is a subwavelength charge pattern. Each period in the SCDW is an electric dipole associated with polarization P that emits secondary radiation. Adjacent dipoles have equal and

opposite phase (π phase difference). This is seen in Fig 2-12 panel (b). But for any

direction $\theta \neq 0$, two adjacent dipoles have a path difference ΔS, where ΔS is given by

$$\Delta s = d \sin \theta < d < \lambda \qquad (2.31)$$

Thus the phase difference between the secondary radiation emitted from the two adjacent

dipoles ($\overrightarrow{P_1}$ and $\overrightarrow{P_1}$ in Fig 2-12 panel (b)) is still close to π provided that d $\ll \lambda$. So, they tend
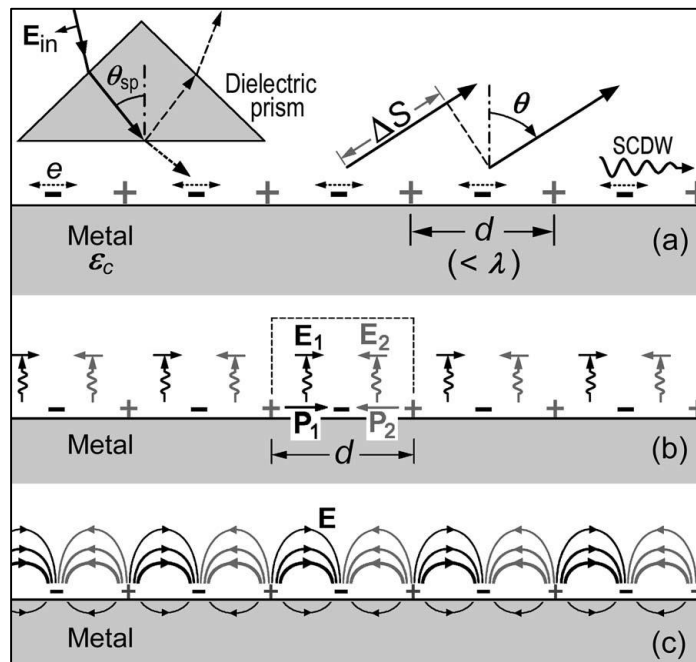
Fig 2-12: SPP on a plane metal surface using Otto geometry. From Huang and Peng [53].

to cancel at any oblique angle in the far field. Secondary radiations along $\theta = 0$ are in phase

($\Delta S = 0$). But, when viewed from a single period of the sinusoidal SCDW each secondary

radiation consists of two sub-secondary (tertiary radiation) radiations with anti-parallel electric

fields $\overrightarrow{E_1}$ and $\overrightarrow{E_2}$ that cancel each other in the far field. Therefore, destructive interference of

the secondary radiation cancels all far field radiation. The secondary radiations form an

45

evanescent wave above the surface as shown in Fig 2-12 panel (c) (compare with Fig 2-1). This is why SPPs correspond to bound surface modes.

Media with $Re(\varepsilon_c) > 0$ do not support SPPs as the wavevector defined in Eq. (2.16) does not satisfy Eq. (2.30). Perfect (or nearly perfect) conductors with $|Re(\varepsilon_c)| \to \infty$, for instance real metals in the microwave and THz regions, do not support SPPs either because as $k_{SP} \to \omega/c = k_0$ in Eq. (2.16), $d \to \lambda$ in Eq. (2.30). This causes $Re(k_{z1}) \to 0$ in Eqs. (2.12) and (2.13), and $Re(k_{z2}) \to 0$ in Eqs. (2.14) and (2.15). Thus, the scattered wave on the conductor surface tends to be non-evanescent. Confinement is lost and the electromagnetic energy radiates away before it can propagate as an SPP.

A plane wave normally incident on a conducting surface without the prism of the Otto geometry is shown in Fig 2-13 panel (a). In this situation free electrons move uniformly along the surface due to $\vec{E}_{in}$. There is no net charge and reflection obeys the Fresnel equations [60]. In Fig 2-13 panel (b), a slit or hole is added to the conductor geometry. Electron motion is now impeded by the corner of the gap edge. Most of the electrons will stop here (although some will continue down the vertical wall) as there is no driving force in normal direction. Negative charges will pile up on one side of the gap. Negative charges will vacate the opposite side leaving only the stationary positive charges. As can be seen, an electric dipole $\vec{P}_a$ is formed across the gap. $\vec{P}_a$ is coupled to the incident radiation and thus oscillates. Hence, $\vec{P}_a$ becomes a new light source and emits secondary radiation. Fig 2-13 panel (c) extends this scenario to a periodic 1D array of slits. The grating is assumed to be semi-infinite, there is no feedback from below (extension of this theory to finite thickness gratings will be covered shortly). The period of the grating is d and the width of each slit is W. Each slit now becomes a new light

46

source. Along oblique directions ($\theta \neq 0$) secondary radiations have a path difference of $\Delta S = d \sin \theta$, where d is now the grating period. For $\lambda > d$ Eq. (2.30) is again satisfied. Oblique
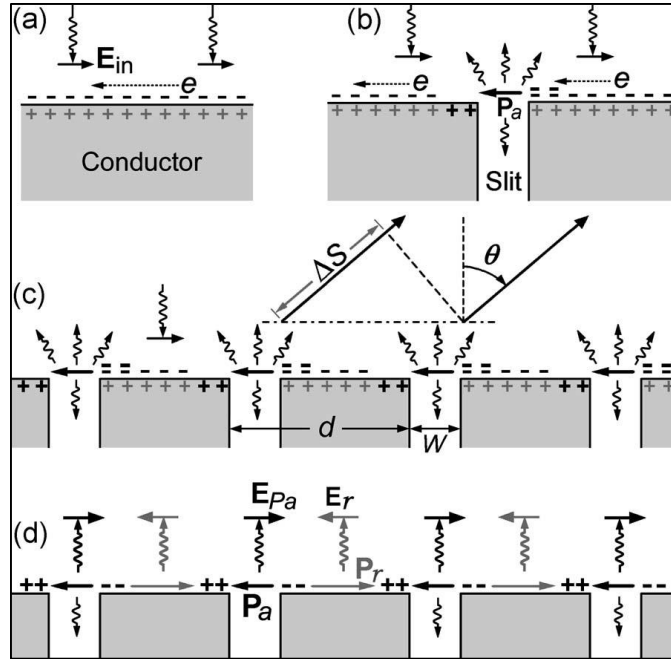
Fig 2-13: SPP on various plane metal surfaces. From Huang and Peng [53].

secondary radiation is cancelled in the far field because of destructive interference. An evanescent wave is formed at the surface.

The charge pattern in Fig 2-13 panel (c) is sub-wavelength, like that in Fig 2-12. Nonetheless, there are two fundamental and important differences. First, the SPP in Fig 2-12 is a propagating wave with a definite k value that is dependent on ε_c, an intrinsic property of the metal. Meanwhile, the SCDW in Fig 2-13 panel (c) is a standing wave with a period that is always equal to the grating period d. Thus, the SCDW's period is a geometrical effect that can occur for any incident wave with $\lambda > d$ and for any conducting media containing free electrons including perfect conductors and conductors with $Re(\varepsilon_c) > 0$. Second, the SPP is a

bound surface mode. In contrast, the SCDW is radiative along $\theta = 0$ ($\Delta S = 0$) as seen in Fig 2-13 panel (d). Here, electric dipole $\vec{P}_a$ emits secondary radiation $\vec{E}_a$. Electric dipole $\vec{P}_r$ emits secondary radiation $\vec{E}_r$ with a phase that is usually very close to the Fresnel reflected wave. If we let $\vec{E}_r$ include the Fresnel reflected wave, then the secondary radiation from each period is seen to have two sub-secondary radiations (tertiary radiations) with opposite directions and phases. Unlike the SPP, $\vec{E}_a$ and $\vec{E}_r$ generally have different strengths and do not fully cancel each other out in the far field. This leads to backward propagation and a strong resonant effect. Previously, these oscillating SCDWs have been called spoof plasmons. Huang and Peng use the term structured surface plasmons (SSPs) to describe them. For periodic structures, the periodicity of the SSP is controlled by the geometry of the structure itself instead of the material properties of the conductor. In this way, the mechanism behind the response of the SSP is similar to that of a metamaterial where the EM response is a function the underlying geometry of the structure rather than the properties of the constituent materials. The SSP effect can be thought of as a type of metamaterial response.

Fig 2-14 shows how the SSP picture extends to finite-thickness gratings (grating period d and slit width W). From Fig 2-14 we see that $\vec{P}_a$ emits a secondary radiation in the forward direction down into the slit. The slit acts like a parallel plate waveguide and secondary radiation $\vec{E}_a$ is constrained to be a plane wave. This plane wave creates oscillating SCDWs on the two slit walls. The SCDWs and $\vec{E}_a$ propagate down the slit walls but suffer some attenuation because of resistive damping from the metal conductor. If the grating is extremely thick, these waves can damp out before reaching the bottom. If the grating is thin enough, the waves will reach the bottom.

Upon reaching the bottom the motion of the electrons is again impeded by the bottom corners of the slit. This causes charges to pile up along the corners leading to another oscillating dipole like $\vec{P}_b$ in Fig 2-14. $\vec{P}_b$ can give strong feedback to the upper surface by emitting $\vec{E}_b$. $\vec{E}_b$ has associated with it two SCDWs propagating upward along the slit walls. If $\vec{E}_b$ is in phase with $\vec{E}_a$, then it enhances $\vec{P}_a$. This enhancement of $\vec{P}_a$ strengthens $\vec{E}_{Pa}$, $\vec{E}_a$, $\vec{P}_b$, $\vec{E}_b$, etc (regenerative feedback). A TEM waveguide resonance is formed. Under this condition, $\vec{E}_r$ is dominated by $\vec{E}_{Pa}$ in the far fields thus minimizing reflection.
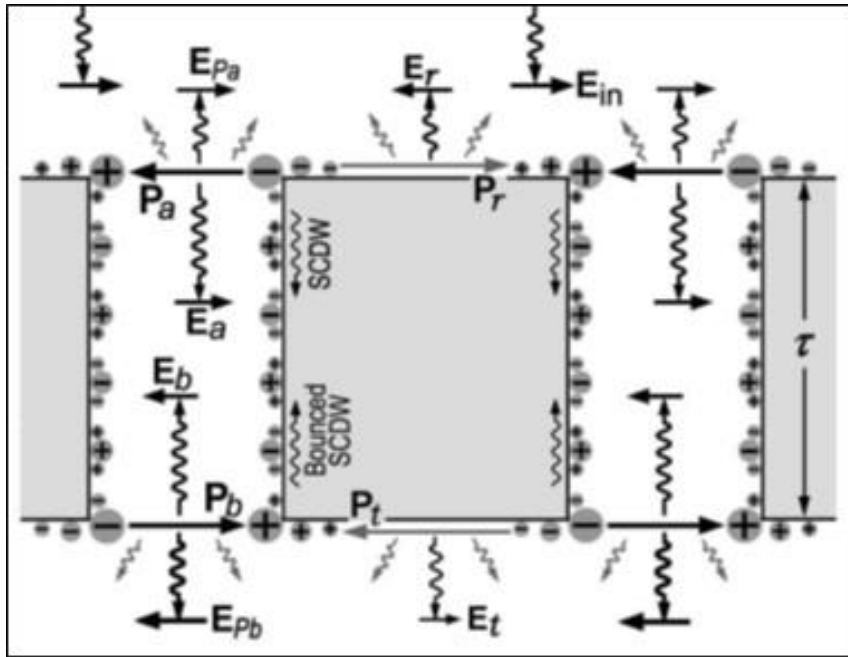
Fig 2-14: Charged oscillation induced light emission, resonance, and transmission through a conducting grating. From Huang and Peng [53].

At the bottom surface, dipoles $\vec{P}_b$ and $\vec{P}_t$ emit secondary radiation away from the slit. For $\lambda > d$, only $\vec{E}_{Pb}$ and $\vec{E}_t$ propagate while oblique secondary radiations are evanescent. Unlike on the top surface, where $\vec{E}_r$ contains specular reflection, $\vec{E}_t$ is emitted exclusively from

dipole $\vec{P}_t$. For $W < d/2$, the strength of $\vec{P}_b$ is much greater than $\vec{P}_t$ so that the transmitted wave is dominated by $\vec{E}_{Pb}$. The energy of the transmitted wave is highly concentrated at the slit openings. For long wavelengths ($\lambda \gg d$) this results in a near field focusing width $W \ll \lambda$ (focusing below the diffraction limit). In the far field, this effect disappears as the transmitted wave becomes a plane wave. At resonant wavelengths, $\vec{E}_{Pb}$ is maximized and therefore zero-order transmission is also maximized. Thus, the SSP picture offers an explanation for both SPP resonances and waveguide resonances. It also explains how SSP-like behavior occurs in the microwave and THz regions of the EM spectrum where good conductors act like perfect conductors.

3.   The Finite Element Method

3.1.   Finite Element Method – A Peak Under the Hood

The finite element method (FEM) is a numerical means for solving boundary value problems consisting of partial differential equations (PDEs) and system of PDEs. The basic idea behind FEM is to break the domain over which the problem is specified into many small connected pieces called elements. This is known as discretization. Then, the equations are numerically solved in each element to approximate the solution over the full domain. The idea is analogous to approximating a curve using many connected straight lines, each short compared to the length of the curve.

The mathematical principle behind FEM is that a problem formulated in what mathematicians call the weak form can yield an approximate solution to the problem in the strong form. Therefore, the first step in FEM is to state any constraints (PDEs and boundary conditions) on the field variables in the weak form [61]. To understand the weak form we first define the strong form. In the strong form, the field variables are required to be continuous and have continuous partial derivatives up through the order of the PDE throughout the domain. In the weak form, the continuity requirements are relaxed. Discontinuities are allowed as long as they are integrable throughout the domain. Restating a PDE in the weak form permits the application of linear algebraic techniques to derive an approximate solution to the original problem.

To see the equivalence of a PDE and its weak form consider Poisson's equation in three dimensions

$$-\nabla^2 u(x) = f(x) \tag{3.1}$$

Here x is a three dimensional dependent field variable in domain Ω. To convert from the strong to the weak form, we define a test function v(x) over Ω and restrict v(x) to a class of functions such that $v \in V$. (3.1) is then multiplied by v(x) and integrated over Ω

$$-\int_\Omega v(x)\nabla^2 u(x)dx = \int_\Omega v(x)f(x)dx \tag{3.2}$$

where dx is a volume element. This equation can be integrated by parts using Green's first identity to get

$$-\int_{\partial\Omega} v(x)\left[\nabla u(x) \cdot \hat{n}\right]dS + \int_\Omega \left[\nabla v(x) \cdot \nabla u(x)\right]dx = \int_\Omega v(x)f(x)dx \tag{3.3}$$

This is the weak form of (3.1). We can simplify this further if we apply the Neumann boundary condition

$$\nabla u(x) \cdot \hat{n} = \frac{\partial u(x)}{\partial \hat{n}} = 0 \tag{3.4}$$

and thus eliminate the boundary term from (3.3). We then have

$$\int_\Omega \left[\nabla v(x) \cdot \nabla u(x)\right]dx = \int_\Omega v(x)f(x)dx \tag{3.5}$$

Rearranging we get

$$\int_\Omega \left[\nabla v(x) \cdot \nabla u(x) - v(x)f(x)\right]dx = 0 \tag{3.6}$$

This equation must hold for all $v \in V$.

In general, a function w(x) can be decomposed into a series of basis functions ϕ_i such that

$$w(x) = \sum_i w_i \phi_i(x) \tag{3.7}$$

where w_i are the coefficients. In the FEM method, the basis functions ϕ_i are functions whose values are only non-zero within a single element referenced by i. This decomposition allows w(x) to be approximated to arbitrary accuracy with piecewise linear basis functions and sufficiently small elements [61]. Note that the basis functions may be of higher order if desired, in which case more than one unknown is needed per element. The number of unknowns and the number of basis function increases with order. We now take V to be the space of all functions that are linear combinations of the basis functions ϕ_i. This allows v(x) to be decomposed and written as [61]

$$v(x) = \sum_i v_i \phi_i(x) \tag{3.8}$$

The test function v(x) enters (3.6) linearly, so if (3.6) is satisfied for each basis function ϕ_i, then it is satisfied for all linear combinations of basis functions, (3.8), and thus for all $v \in V$. Therefore, (3.8) can be substituted into (3.6) to create a $(k+1)N \times (k+1)N$ system of equations in $(k+1)N$ unknowns where k is the order of the element (k = 1 is linear, k = 2 is quadratic, etc.) and N the number of elements. This system will approximate the solution to Eq. (3.1).

Commercial-Off-The-Shelf (COTS) FEM programs automatically assemble and solve these $(k+1)N \times (k+1)N$ systems of equations. In the assembling the matrices, the FEM method applies what is known as the Galerkin formulation which sets v(x) = u(x) [61]. One

method of solution to the above system is to use a nonlinear solver such as Newton's Method. The N-dimensional analogue of Newton's Method for vector equations is

$$L(U) = 0 \qquad (3.9)$$

where U is a vector of the unknowns. L(U) is a system of equations formed by substituting the basis functions ϕ_i for v and u in Eq. (3.6). Doing so yields [61]

$$K(U_0)(U - U_0) = L(U_0) \qquad (3.10)$$

where $K(U_0)$ is known as the stiffness matrix and $L(U_0)$ is the load vector. The stiffness matrix is the negative Jacobian of L

$$K(U_0) = -\frac{\partial L(U_0)}{\partial U} \qquad (3.11)$$

(3.10) gives a linear matrix equation for U in terms of a previous approximate solution U_0. If U_0 is reasonably close to U, Eq. (3.10) should converge to an acceptable accuracy of U in a finite number of iterations, with each iteration improving upon the accuracy of the solution [61]. COTS FEM programs automate the solution to these types of systems and can reach an approximate solution to an accuracy determined by the user and the computer resources available.

3.2. Finite Element Method – Element Types

There are number of basic element types used to discretize the domain in an FEM problem, classified according to shape and order. Various element shapes for one, two, and three dimensional geometries are shown below in Fig 3-1.
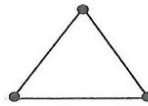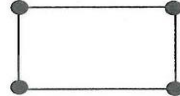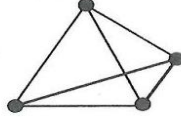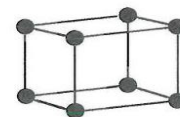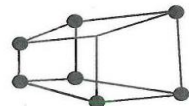
Fig 3-1: Basic finite element shapes. From Zimmerman [61].

For one dimensional problems, the element shape is always a line segment which resides within the interval on which the solution is sought. As can be seen, two and three dimensional problems offer more variety in element shapes.

The geometry of the element is an important factor and is one of the main advantages of FEM over other numerical PDE solving methods. This because when a domain is discretized into finite elements, the resulting mesh is conformal. This means that even problems with complex curved geometries may be discretized and that the solutions calculated using FEM cover the entire domain. This often leads to improved accuracy over other numerical methods such as the Finite Difference Method which uses a fixed grid point mesh.

The order of an element conveys the order of the interpolation polynomial (the basis function) used to mathematically define that element. There are three types of elements as categorized by order: Simplex, Complex, and Multiplex [61]. Simplex elements use polynomials with linear terms and constants and have nodes at the corners of the element. All

the elements shown in Fig 3-1 are simplex elements. Complex elements use higher order polynomials (quadratic, cubic, quartic, etc.) with corner nodes as well as edge and internal nodes. Multiplex elements also use higher order polynomials but are laid out such that their sides are parallel to the coordinate axis. Examples of complex elements with polynomial basis functions up to the third order are shown in Fig 3-2. Note that the accuracy of a solution increases with the use of higher-order-polynomial basis functions. However, higher order basis functions are more complicated and thus take more time and memory to compute. Thus, the advantage of higher order basis functions is often offset. There is a tradeoff between accuracy and computational time/resources. This is a common theme among all numerical methods.
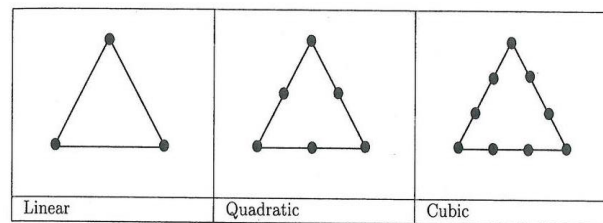
Fig 3-2: Complex finite elements with polynomial basis functions up to third order. From Zimmerman [61].

3.3.   Finite Element Method – Elements vs. Accuracy

There is a further trade-off between the accuracy, computational time, and resources required to arrive at the solution and the number of elements in the discretization. There is no formula for choosing the optimum number of elements. Nominally, the accuracy of the solution increases with the number of elements N. Nevertheless, there is a certain number, known as the critical number (N_c), beyond which increasing the number of elements does not significantly increase solution accuracy. This is shown in Fig 3-3. Increasing the resolution

of the mesh beyond N_c elements will increase computational time and memory requirements. It does not provide any meaningful increase in accuracy of the solution.
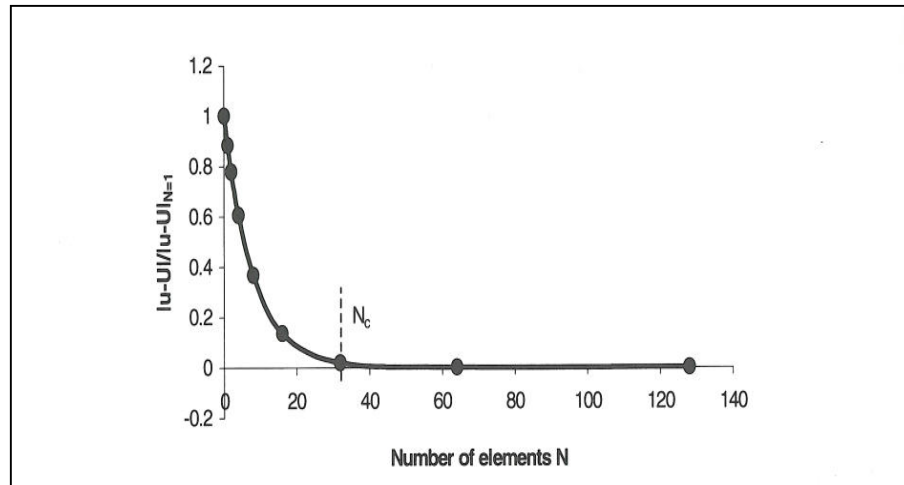
Fig 3-3: Normalized error versus number of elements N. From Zimmerman [61].

3.4.   HFSS and COMSOL

Two FEM packages were used to perform the simulations in this dissertation. High Frequency Structure Simulator (HFSS) was used to simulate THz and LWIR components while COMSOL Multiphysics was used to simulate LWIR components. The choice of these tools was based on availability. The THz simulation work was started in 2011 at Wright State University's THz Sensors Laboratory. At that time, HFSS was the only package available. The initial LWIR simulations were done at the Air Force Research Laboratory's Sensors Directorate at Wright Patterson Air Force Base in the summer of 2012. Again, HFSS was the only available package at that time. Later, LWIR simulations were done using COMSOL when it became available in the summer of 2013.

HFSS is an FEM software package from Ansys Inc., formally Ansoft. It provides full wave solutions to the Helmholtz wave equation within a user defined 3D solution domain. It

provides a large library of material models to use in electromagnetic simulations. Both dielectrics and conductors are included in the HFSS material model library. The dielectrics are defined by real-valued dielectric constants and in many cases dielectric loss tangents. Conductors are defined by real-valued conductivities and real-valued dielectric constants of value unity. All electrical parameters defined in the HFSS material library are constant with respect to frequency. Therefore, HFSS material library dielectrics and conductors are dispersionless. However, HFSS allows users to define their own material models characterized by user defined permittivities, conductivities, and loss tangents. User defined material models may be frequency dependent. In this dissertation they were entered as look-up tables that the HFSS computation engine referenced as needed during simulation calculations.

HFSS has an adaptive meshing algorithm that builds the mesh through iterative discretization of the solution domain. An initial mesh is generated based upon a user defined solution frequency and a user defined error value Δs. Both of these values are entered by the user during the simulation set up. HFSS calculates the S-parameters from the initial mesh. The mesh is then refined. The S-parameters are calculated again. The differences between the S-parameters from the first and second meshes is Δs. If Δs is less than or equal to the user provided value, the adaptive mesh engine considers the mesh converged and uses the second mesh for all further calculations. If Δs is greater than the user defined value, another mesh refinement and S-parameter calculation is executed. Another Δs is calculated using the third and second mesh S-parameters. If this Δs is less than or equal to the user provided value, the adaptive mesh engine considers the mesh converged and uses the third mesh for all further calculations. Otherwise, another mesh refinement is generated. This process continues until a Δs is found that is less than or equal to the user defined accuracy goal or until an iteration

limit is reached. In HFSS, the user has some control over the initial mesh parameters and the meshing algorithm that is used. However, this control is limited relative to other solvers. HFSS's adaptive mesh algorithm is a "smart" algorithm that removes a significant amount of the set up from the user's hands. But, it also takes much of the control out of the user's hands in accomplishing this.

HFSS works very well in the THz, microwave, and RF regions of the EM spectrum. It has a desktop interface that is relatively straight-forward to use. It has a good reputation in the modeling of RF and microwave antennas as well as microwave devices and components. Nonetheless, HFSS is strictly an electromagnetics solver. It only solves the Helmholtz wave equation. No other physical problems may be solved with it. The user cannot add to or change any of the physics as it is embedded into the package. In this dissertation, HFSS struggled with electromagnetic components and structures when their dimensions were comparable to the wavelength of the incident radiation. This is because these geometries physically generate higher diffraction orders, all of which must be accounted for in the simulation's energy calculations. This led to significantly more elements and electromagnetic modes in the simulation and thus significantly more computational time and resource requirements to solve those problems. To be fair to HFSS, this is an issue with any FEM solver.

COMSOL Multiphysics is an FEM solver from COMSOL Inc. COMSOL was formally known as FEMLAB. Like HFSS, COMSOL provides full wave simulation solutions to the Helmholtz wave equation through its RF module, as well as library or user defined material models. Unlike HFSS, COMSOL provides physics based modeling. This reveals itself most markedly in multiphysics simulations. Multiphysics simulations have two important characteristics. First, they provide the user with the ability to perform different

physical simulations with the same software package and the same workflow. COMSOL Multiphysics is a modular software package. Different modules can be purchased and installed to model different physical phenomena such as electromagnetics, thermal physics, structural analysis, semiconductor physics, plasma physics etc. Second, COMSOL Multiphysics provides the user with the ability to couple these different physics models together into one simulation. For example, thermal physics and electromagnetics may be coupled together to model current flow in a copper wire. The current will cause a change the wire's temperature. Since the change in the wire's temperature will then affect the wire's conductivity, the current will change. This will further change the temperature which will further change the conductivity and so on. These interactions can be defined and mutually coupled into one study and solved self-consistently to deliver a more realistic simulation result.

COMSOL gives the user the ability to set up simulations by using the built-in physics interface or by using Equation Based Modeling. Both methods are accessed from the desktop interface. With the physics interface, the user selects the type of physics problem(s) to solve via a menu driven process. The standard COMSOL workflow then leads the user into creating the geometry, assigning materials, defining boundary conditions, and defining excitation sources. The simulation is then executed. The results can then be viewed in a number of tabular, file, and visual formats. Alternatively, with Equation Based Modeling, the user may directly enter the PDE(s) governing the physical phenomenon into the model. Homogeneous or non-homogeneous equations (PDEs, ODEs, and algebraic) and systems of equations may be entered manually. Boundary conditions and excitation sources are manually entered as well. The simulation is then executed. The same options for viewing the results that are offered with the physics interface are offered with Equation Based Modeling. The two

approaches may be combined to give the user extra flexibility if new physics needs to be injected into a simulation already using a physics interface. COMSOL also allows users to build their own desktop physics interface templates from the Equation Based Modeling process. These features give the user the ultimate in control and flexibility in FEM modelling. Finally, COMSOL allows the user significant control over the meshing details and the computational algorithms used to mesh and simulate the problem. COMSOL essentially gives users an FEM toolbox for scientific and engineering analysis with significant flexibility and control. On the other hand, all these features and capabilities come with a price. COMSOL Multiphysics is much more difficult to learn than HFSS. However, due to the sophistication of COMSOL's approach to FEM modeling, one can certainly argue that it is worth the effort in the long-run for anyone wishing do serious simulation studies.

4.   Full Wave Simulations of THz Wire-Grid Polarizers

4.1.   The Drude Model for Metals and the Dielectric Function

In this dissertation, the Drude model [62] for AC conductivity in metals and the dielectric function were both used to describe the electromagnetic response of metals in THz simulations. This was done to improve the accuracy of the simulations relative to real-world results. We did not believe that the library material models for metals provided by HFSS were adequate for this task as they are dispersionless and use real-valued conductivities and permittivities. This is a satisfactory approximation in the common RF bands where HFSS is most often used, but becomes increasingly inaccurate at THz frequencies and above.

Paul Drude constructed his theory of electrical conductivity in metals by applying the kinetic theory of gases [43]. The Drude model treats a metal as a free electron gas in which the negatively charged valence electrons detach from their respective atoms. These electrons then move freely throughout the interior of the metal. The atoms that have given up their valence electrons are positively charged ions which are stationary. The major assumptions in the Drude model are as follows [43]:

- *Independent electron approximation* – The interaction between the electrons moving through the metal is neglected.

- *Free electron approximation* – Other than collisions, the interaction between the electrons and the ions in the metal is neglected.

- *Collisions are instantaneous* – The collisions between the electrons and the ions are instantaneous and elastic, abruptly altering the velocity of the electron. The positions of the ions are unaffected by the collisions.

- *Mean time between collisions* – There is a mean time between collisions, τ. This time (also known as the electronic relaxation time or simply the relaxation time), is of the order of 10^{-14} s for most metals at room temperature. There is a damping frequency, γ, that is the multiplicative inverse of the relaxation time, $\gamma = 1/\tau$. Therefore, $\gamma \sim 100$ THz at room temperature.

- *Thermal equilibrium* – The electrons achieve thermal equilibrium with their surroundings only through collisions. There is no memory of the pre-collision state. After each collision, the electron has a velocity vector that is not related to its velocity vector before the collision. The magnitude of the post-collision velocity vector is a function of the temperature at the location of the collision.

The DC conductivity of a metal can be described by two important equations:

$$\vec{J} = \sigma_0 \vec{E} \tag{4.1}$$

and

$$\sigma_0 = \frac{ne^2\tau}{m} \tag{4.2}$$

where (4.1) is a vectorial form of Ohm's Law. It equates the current density $\vec{J}$ with the product of the DC conductivity of the material (σ_0) and the applied electric field $\vec{E}$. The DC conductivity is given by (4.2) where n is the electron concentration, e is the electronic charge, τ is the relaxation time, and m is the mass of an electron.

The basic derivation of the AC conductivity of a metal is given in Ashcroft and Mermin [43]. First, the applied electric field is written in phasor form as

$$\vec{E}(t) = \mathrm{Re}\left\{\vec{E}(\omega)e^{-i\omega t}\right\} \qquad (4.3)$$

where the physics sign convention exp(-iωt) is used in this derivation. HFSS uses the electrical engineering sign convention exp(iωt). Use of the electrical engineering sign convention would change the signs of the imaginary parts in the results that follow. The equation of motion for a free electron in a metal driven by an applied electric field and written in terms of its momentum is

$$\frac{d\vec{p}}{dt} = -\frac{\vec{p}}{\tau} - e\vec{E} \qquad (4.4)$$

The steady state solution to (4.4) is of the form

$$\vec{p}(t) = \mathrm{Re}\left\{\vec{p}(\omega)e^{-i\omega t}\right\} \qquad (4.5)$$

Substitution of (4.3) and (4.5) into (4.4) gives

$$-i\omega\vec{p}(\omega) = -\frac{\vec{p}(\omega)}{\tau} - e\vec{E}(\omega) \qquad (4.6)$$

The current density is

$$\vec{J} = -ne\vec{v} = -\frac{ne\vec{p}}{m} \qquad (4.7)$$

and may also be written as

$$\vec{J}(t) = \mathrm{Re}\left\{\vec{J}(\omega)e^{-i\omega t}\right\} \qquad (4.8)$$

Solving (4.6) for p(ω) and substituting this into (4.7) and then writing the current density as in (4.8) we finally get

$$\vec{J}(\omega) = -\frac{ne\,\vec{p}(\omega)}{m} = \frac{\left(ne^2/m\right)\vec{E}}{\left(1/\tau\right)-i\omega}$$
(4.9)

(4.9) is usually written

$$\vec{J}(\omega) = \sigma(\omega)\vec{E}(\omega)$$
(4.10)

where σ(ω) is known as the frequency dependent AC conductivity of the metal and is given by

$$\sigma(\omega) = \frac{\sigma_0}{1-i\omega\tau}$$
(4.11)

This is the Drude result for AC conductivity in a metal. This result can be decomposed into

$$\sigma(\omega) = \sigma_1(\omega) + i\sigma_2(\omega)$$
(4.12)

There is an important implicit assumption underlying this derivation. That assumption is that the force on each electron due to the applied electric field is the same. In other words, the electric field is uniform. This assumption will be true only if the wavelength of the radiation is much larger than the mean free path of the electrons ($\lambda \gg l$). This requirement is normally satisfied in metals by radiation at visible wavelengths and by all radiation of longer wavelengths.

We also need the dielectric function. We start with the following four equations which represent the relationships between the electrical polarization and the electric field (4.13), internal charge and internal charge density (4.14), and the constitutive relations in the frequency domain (4.15) and (4.16), all as given in Maier [42].

$$\vec{D} = \varepsilon_0 \vec{E} + \vec{P} \tag{4.13}$$

$$\vec{J}_{\text{int}} = \frac{\partial \vec{P}}{\partial t} \tag{4.14}$$

$$\vec{D}(\vec{k}, \omega) = \varepsilon_0 \varepsilon(\vec{k}, \omega) \vec{E}(\vec{k}, \omega) \tag{4.15}$$

$$\vec{J}_{\text{int}}(\vec{k}, \omega) = \sigma(\vec{k}, \omega) \vec{E}(\vec{k}, \omega) \tag{4.16}$$

By substituting (4.13) into (4.15) we get

$$\varepsilon_0 \vec{E}(\vec{k}, \omega) + \vec{P}(\vec{k}, \omega) = \varepsilon_0 \varepsilon(\vec{k}, \omega) \vec{E}(\vec{k}, \omega) \tag{4.17}$$

We can rewrite (4.14) as

$$\vec{J}_{\text{int}}(k, \omega) = \frac{\partial \vec{P}(k, \omega)}{\partial t} = -i\omega \vec{P}(\vec{k}, \omega) \tag{4.18}$$

Then, substituting (4.18) and (4.17) into (4.16) we have

$$-i\omega \vec{P}(\vec{k}, \omega) = \sigma(\vec{k}, \omega) \vec{E}(\vec{k}, \omega) \tag{4.19}$$

$$-i\omega \left[\varepsilon_0 \varepsilon(\vec{k}, \omega) \vec{E}(\vec{k}, \omega) - \varepsilon_0 \vec{E}(\vec{k}, \omega) \right] = \sigma(\vec{k}, \omega) \vec{E}(\vec{k}, \omega) \tag{4.20}$$

$$-i\omega \varepsilon_0 \varepsilon(\vec{k}, \omega) + i\omega \varepsilon_0 = \sigma(\vec{k}, \omega) \tag{4.21}$$

$$-i\varepsilon(\vec{k}, \omega) = -i + \frac{\sigma(\vec{k}, \omega)}{\varepsilon_0 \omega} \tag{4.22}$$

$$\varepsilon(\vec{k}, \omega) = 1 + i \frac{\sigma(\vec{k}, \omega)}{\varepsilon_0 \omega} \tag{4.23}$$

For $\lambda \gg l$ a homogeneous spatially local response can be assumed, $\varepsilon(\vec{k}, \omega) \to \varepsilon(\omega)$, and we get our final result

66

$$\varepsilon(\omega) = 1 + i\frac{\sigma(\omega)}{\varepsilon_0\omega} \tag{4.24}$$

(4.24) is known as the dielectric function [42] which can be decomposed into real and imaginary parts

$$\varepsilon(\omega) = \varepsilon_1(\omega) + i\varepsilon_2(\omega) \tag{4.25}$$

Since the refractive index of a material is given by $\hat{n}(\omega) = \sqrt{\varepsilon(\omega)}$, the refractive index will also be complex and frequency dependent

$$\tilde{n}(\omega) = n(\omega) + i\kappa(\omega) \tag{4.26}$$

with

$$\varepsilon_1 = n^2 - \kappa^2 \tag{4.27}$$

$$\varepsilon_2 = 2n\kappa \tag{4.28}$$

and

$$n^2 = \frac{\varepsilon_1}{2} + \frac{1}{2}\sqrt{\varepsilon^2_1 + \varepsilon^2_2} \tag{4.29}$$

$$\kappa = \frac{\varepsilon_2}{2n} \tag{4.30}$$

In (4.27), (4.28), and (4.30) κ is the extinction coefficient. The extinction coefficient characterizes the decay of the electric field propagating through an attenuating medium. It can be linked to the absorption coefficient in Beer's law by

$$\alpha(\omega) = \frac{2\kappa(\omega)\omega}{c} \tag{4.31}$$

where c is the speed of light in vacuum and Beer's law describes the decay of the electromagnetic intensity as

$$I(x) = I_0 e^{-\alpha(x)x} \tag{4.32}$$

Consequently, the imaginary part of the dielectric function, ε_2, determines the loss in a material from absorption through κ. For $|\varepsilon_1| \gg |\varepsilon_2|$, the real part of $\tilde{n}$, which determines the phase velocity of light propagating through a medium as affected by internal electric polarization (the creation of electric dipoles), is predominantly determined by ε_1. In looking at (4.24) we see that there is a linkage between conductivity, as given by the Drude model, and the dielectric function. Using (4.11) and (4.12) we can develop the following relationships for the real and imaginary parts of the conductivity as functions of the DC conductivity, the frequency, and the relaxation time

$$\sigma_1(\omega) = \frac{\sigma_0}{1 + \omega^2 \tau^2} \tag{4.33}$$

$$\sigma_2(\omega) = \frac{\sigma_0 \omega \tau}{1 + \omega^2 \tau^2} \tag{4.34}$$

The real and imaginary parts of the dielectric function can be written in terms of the real and imaginary parts of the conductivity

$$\varepsilon_1(\omega) = 1 - \frac{\sigma_2}{\varepsilon_0 \omega} \tag{4.35}$$

$$\varepsilon_2(\omega) = \frac{\sigma_1}{\varepsilon_0 \omega} \tag{4.36}$$

Thus, the imaginary part of the complex conductivity contributes to the real part of the complex relative permittivity. Therefore, σ_2 determines the amount of polarization in a

material and hence the phase velocity of light passing through that material. The real part of the complex conductivity contributes to the imaginary part of the complex relative permittivity. Thus, σ_1 determines the amount of loss due to absorption. At low frequencies, we usually associate ε with the response of bound electrons to an applied electric field. This leads to the phenomenon of electric polarization. We associate σ with the response of free electrons to an applied electric field leading to electric current. Both of these phenomena result in the loss of electrical energy. This derivation shows that, at higher frequencies, the distinction between losses due to permittivity and conductivity and therefore between bound and free electrons is less clear (this justifies treating a metal as a highly polarizable dielectric in Section 2.2).

Dielectric loss in a material may be quantified by either the loss angle or the corresponding loss tangent. A dielectric can be represented as a lumped circuit model in the form of a capacitor whose impedance can be plotted as a phasor on the complex impedance plane. A diagram is shown in Fig 4-1. If the dielectric is lossless, the capacitor representing it will only have a reactive component and thus its impedance phasor will be collinear with the negative imaginary axis. If the dielectric has loss, the lumped circuit model will be an ideal capacitor in series with an Equivalent Series Resistor (ESR). The impedance phasor for the ESR will be collinear with the positive real axis. The impedance phasor of the lossy dielectric will be the vector sum of the reactive component and the ESR component. Thus, it will no longer be collinear with the negative imagery axis. The angular difference between the negative imaginary axis and the impedance phasor is known as the loss angle of the dielectric (δ). The loss tangent is the tangent of the loss angle.
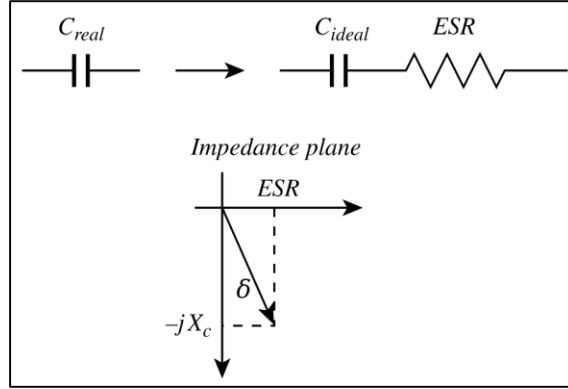
Fig 4-1: A real dielectric can be thought of as a real capacitor which is represented by a lumped circuit consisting of an ideal lossless capacitor and an Equivalent Series Resistance (ESR). The loss angle is the angle between the impedance phasor of the real capacitor and the negative imaginary axis. From [63].

In practical terms, the loss tangent is a ratio of the lossy reaction of the material to an applied electric field to the lossless reaction of the material to the applied electric field. The loss tangent can be mathematically defined as

$$\tan(\delta) = \frac{\varepsilon_2(\omega)}{\varepsilon_1(\omega)} \tag{4.37}$$

The Drude model and the dielectric function are accurate at predicting the optical response in metals for frequencies whose corresponding energies are below the threshold for transitions between electronic bands, i.e., "interband" transitions [42]. For alkali metals these transitions are in the ultraviolet region of the electromagnetic spectrum. However, for the noble metals (gold, silver, and copper), interband transitions start to occur for energies of approximately 1 eV ($\lambda \cong 1.24$ μm). Electronic interband transitions are quantum effects and are not taken into account in a free electron model. Therefore, the optical responses of real metals deviate from what the Drude model predicts in these regions. Plots of these deviations are shown below in Fig 4-2 for silver. Nonetheless, the region of interband transitions is far

70

above the THz and LWIR regions. Lucyszyn has established that the Drude model is valid for frequencies ranging from 30 GHz to 12 THz ($\lambda = 25$ μm) [64]. Therefore, it is quite appropriate to use the Drude model in the THz region of the electromagnetic spectrum. Study of Fig 4-2 leads to the conclusion that this should be true for LWIR as well.
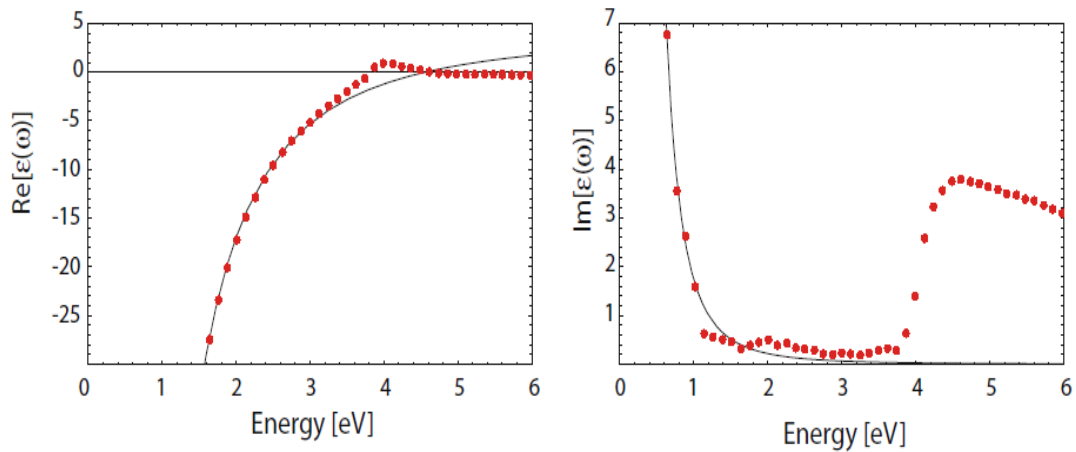
Fig 4-2: The real and imaginary part of ε(ω) for silver as measured by Johnson and Christy (dots) [65] and the smooth Drude model curve over the same region.

As shown above, the dielectric function of a metal can be calculated using the Drude model starting from nothing more than the DC conductivity (or resistivity ρ) and the relaxation time. Using ρ = 28.3 nΩ·m (σ = 1/ ρ) and τ = 8.0 ps for aluminum (Al) [43] and ρ = 22.14 nΩ·m and τ = 30 ps for gold (Au) [43], Eqs. (4.33) - (4.36) were used to build custom HFSS material models for metals in the THz region. A MATLAB program was developed to calculate the real and imaginary parts of the relative permittivities and the conductivities, as well as the loss tangents for Al and Au for frequencies from 100 GHz to 4000 GHz (4 THz). The output of these programs was a set of .tab files in which the frequencies and the calculated electrical parameters were stored. The data values in these files were then loaded into HFSS

as lookup tables. Thus, custom materials were created for use in HFSS that exhibited both loss and dispersion. The name of the MATLAB program files are drude_al.m and drude_au.m. Printouts of both are shown in the Appendix. Plots of the outputs of drude_al.m are shown in Fig 4-3 through Fig 4-7. From these figures we see that the real part of the conductivity and the imaginary part of the relative permittivity for Al both decrease with increasing frequency. Al becomes a poorer conductor as frequency increases. The imaginary part of the conductivity and the real part of the relative permittivity both increase with increasing frequency. The real part of the relative permittivity is large and negative from 100 GHz to 4 THz. All of the other relative permittivity and conductivity values are large and positive over this frequency range. The loss tangent for Al decreases with increasing frequency from a value of approximately 200 at 100 GHz to a value of approximately 5 at 4 THz. This program was later modified to calculate the same electrical parameters for Au. The only change that was made to the program was to modify the DC conductivity and the electronic relaxation time from those used for Al to those used for Au and given in the text above.
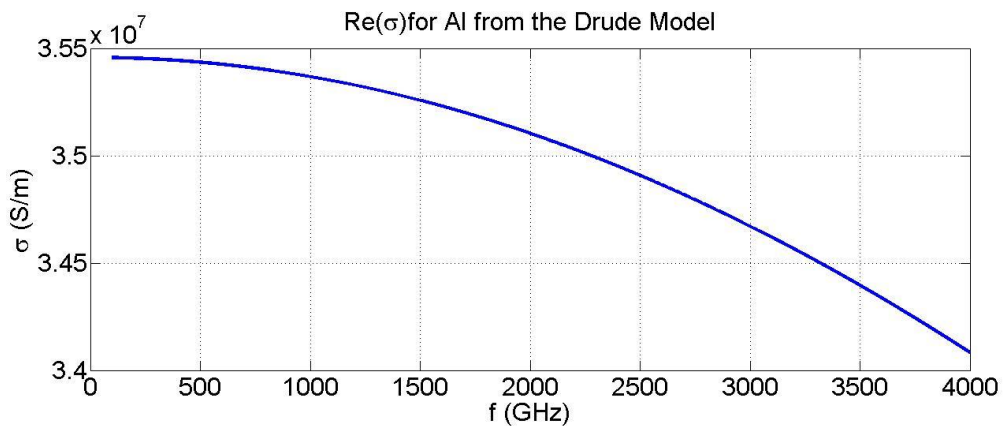
Fig 4-3: Real part of the complex conductivity of Al as calculated from the Drude model.
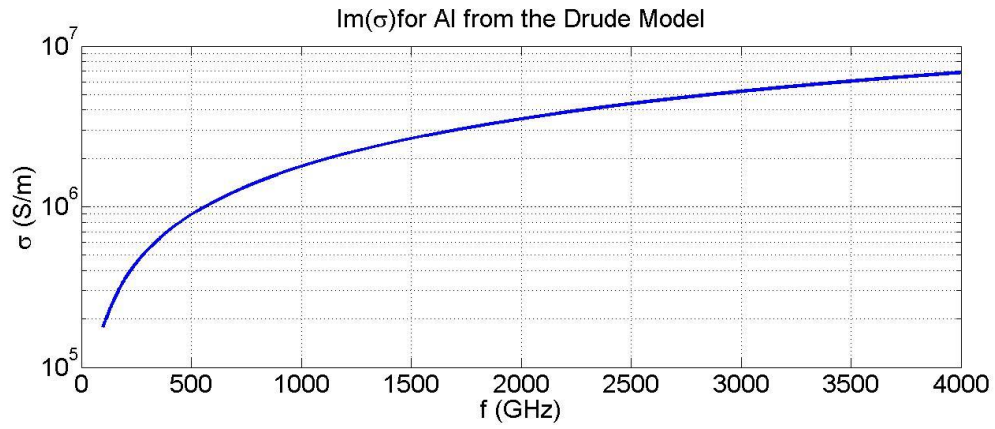
Fig 4-4: Imaginary part of the complex conductivity of Al as calculated from the Drude model.
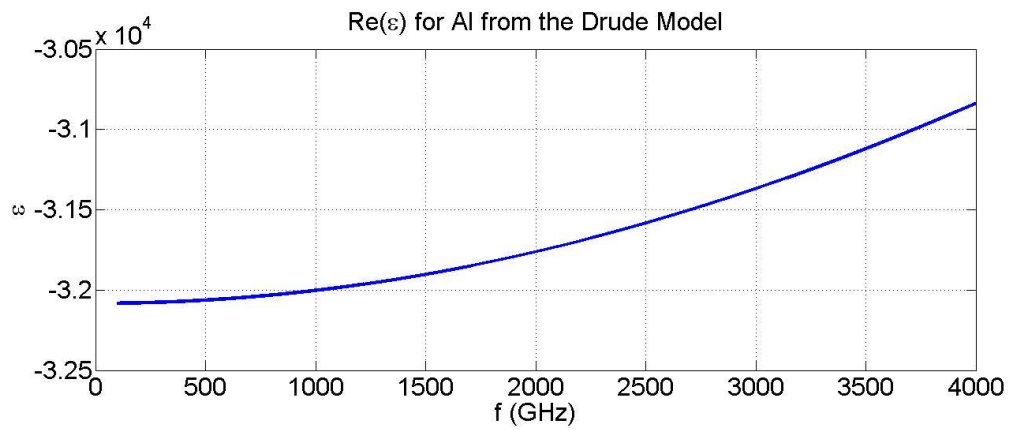
Fig 4-5: Real part of the complex relative permittivity of Al as calculated from the Drude model.
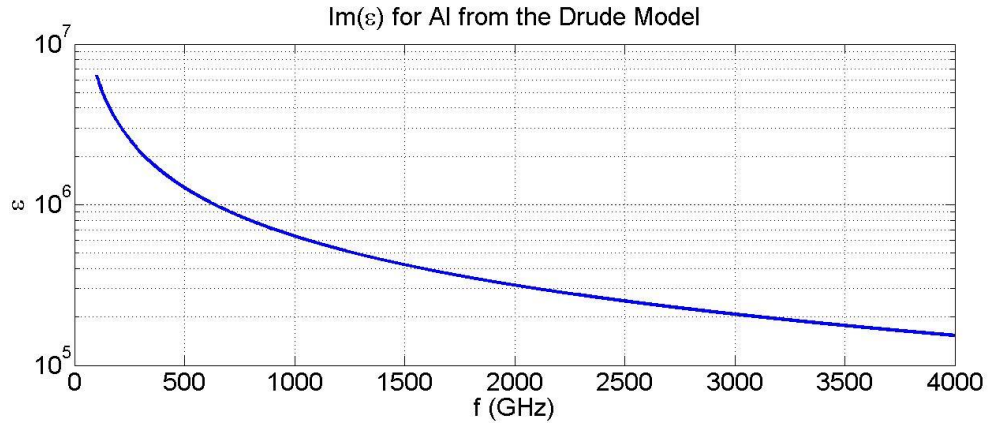
Fig 4-6: Imaginary part of the complex relative permittivity of Al as calculated from the Drude model.
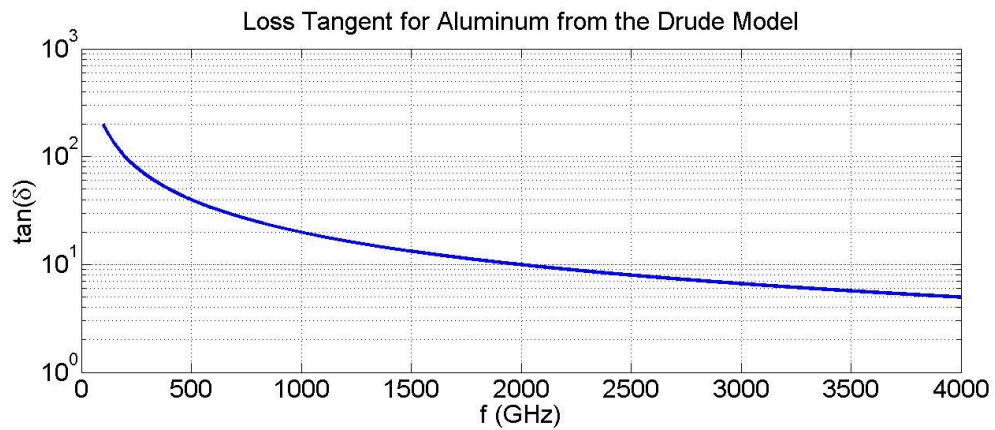
Fig 4-7: Loss tangent for Al as calculated from the Drude model.

When creating a custom material, HFSS requires the entry of the real part of the relative permittivity and either the real part of the conductivity or the loss tangent. One of these latter two parameters is entered at the exclusion of the other. The unselected parameter is then entered as zero because the HFSS software uses the two entered parameters to calculate the third. Entry of the conductivity automatically enables the HFSS solve inside feature in the mesh engine. This will result in HFSS meshing the inside of a metal domain to a very high

degree of resolution. Because of the skin effect, high resolution meshing is unnecessary and undesirable. Therefore, the loss tangent is always entered instead of the conductivity. In this study, the real part of the relative permittivity and the loss tangent are the two parameters used to create custom models for Al and Au in HFSS.

4.2. A THz Wire-Grid Polarizer with EOT

Wire-grid polarizers have been important passive optical devices for over one hundred years. They were initial used in 1888 by Heinrich Hertz to investigate the properties of radio waves [66]. Wire-grid polarizers have been demonstrated throughout a large portion of the electromagnetic spectrum, from radio frequencies through ultraviolet [67], [68], [69], [68], [70], [71], [72], [73], [74]. Wire-grid polarizers typically consists of a regular periodic array of fine parallel metallic wires in free space or mounted on a low loss dielectric substrate. The wire array is oriented in a plane that is perpendicular to the incident radiation. The wire-grid polarizer transmits light with perpendicular (S) polarization and blocks light with parallel (P) polarization. Fig 4-8 shows a schematic of a wire-grid polarizer and its function. A THz wire-grid polarizer was the first THz component to be studied in detail for this dissertation. This component was simulated, optimized, fabricated and then characterized.

As already discussed, SPP-like behavior that generates EOT can be observed at THz and lower frequencies. The behavior can be explained using the SSP picture [53]; the mechanism is also known as a "spoof plasmon" [59]. A grid of periodically spaced apertures in a metal film can support spoof plasmons when $d < a \ll \lambda$ (d = aperture diameter, a = grid period, and λ = radiation wavelength). This is basically the same mechanism that produces the
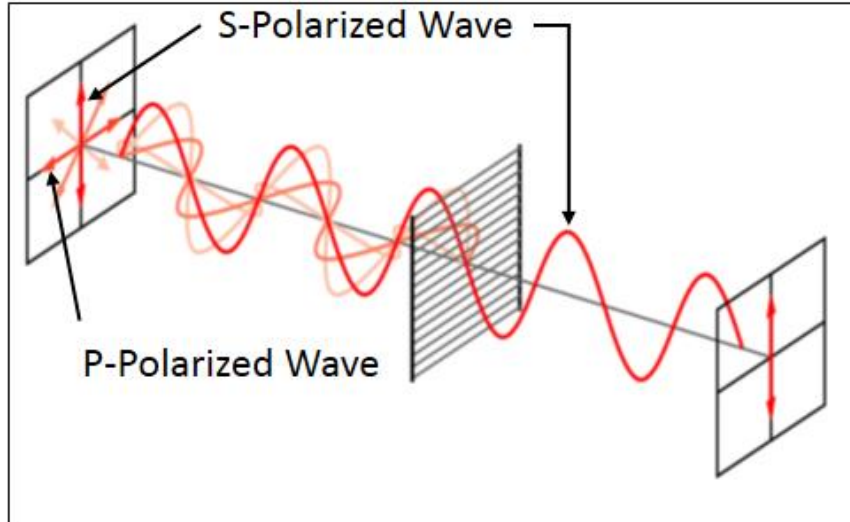
Fig 4-8: Wire-grid polarizer. Light with perpendicular polarization (S) is transmitted through the polarizer. Light with parallel polarization (P) is blocked. From Wikipedia [75].

effects seen in metamaterials, and has been described using periodic arrays of circular-holes by Pendry [59]. In this section, the EOT effect is demonstrated in a THz wire-grid polarizer 0by numerical simulation and experiment.

The THz wire-grid polarizer consists of an array of aluminum strips of width w and separations (gaps) d patterned on an insulating substrate of polycarbonate - a plastic with high RF transparency which can be made flat and smooth enough for micron-scale lithographic fabrication. The objective was to study this basic design to large values of fill factor, FF = w/(w+d) > 90%. The device's period (w+d) was held constant at 40 μm, and its thickness at 0.2 μm to match the experimental value determined by evaporation. Single layer millimeter-wave and THz strip-on-substrate polarizers have been studied previously [76], [77], [78], [79] but not at the large fill factors (FF ≥ 90%) investigated here.

The numerical simulations were carried out using HFSS. The power transmissivity (T) and phase angle were calculated for incident radiation polarized perpendicular (S) and parallel (P) to the strip axis at frequencies from 100 GHz to 1000 GHz in steps of 1 GHz. The fill factor was varied by changing the strip width from 0 to 39.9 μm. All geometries were sub-wavelength relative to the range of simulated frequencies. The geometry was simulated at the unit cell level, shown in Fig 4-9. Periodic boundary conditions, known as Master/Slave conditions in HFSS, were applied. Floquet ports were used to excite the unit cell with electromagnetic radiation. For all simulations the incoming radiation was at normal incidence. In addition, the electric and magnetic fields were calculated throughout the simulation domain. This allowed for the viewing and analysis of field strengths and directions at critical locations in the simulation domain, especially in the air gaps between the wires. To enhance the accuracy, losses in the aluminum were incorporated using a look-up table for the metal dielectric function based on the Drude model for AC conductivity. Absorptive losses in the polycarbonate were also simulated using a separate look-up table containing the frequency-dependent dielectric function derived from broadband transmission data taken with a THz photomixing spectrometer.

The transmissivity values for fill factors ranging from 0 to 99.75 % were calculated from 100 GHz to 1000 GHz. Spot frequencies of 100, 275, 530, and 1000 GHz are plotted on a linear and log scale in Fig 4-10(a) and Fig 4-10(b), respectively. As can be seen, the S-polarized transmissivity at each frequency is relatively flat for fill factors up to approximately 98% and then drops precipitously. In contrast, the P-polarized transmissivity drops steadily with FF. For wire grid polarizers the insertion loss ($IL = 10 \cdot \log_{10} T$) and the extinction ratio (ER) are the two most important figures-of-merit. ER is the ratio of the S-polarized
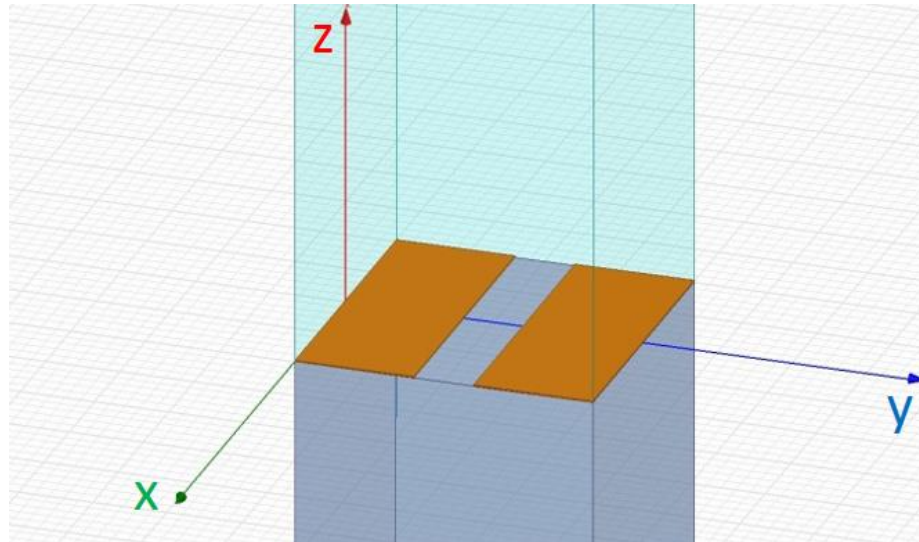
Fig 4-9: THz wire grid polarizer unit cell geometry for 80 % fill factor.

transmissivity to the P-polarized transmissivity, and is plotted vs. fill factor in Fig 4-11(a). As

can be seen in Fig 4-11(a), the ER increases with increasing fill factor up to peaks of about 60

dB at fill factors between 90 and 100%. The exploded view in Fig 4-11(b) shows that the peak

ER fill factor decreases with increasing frequency. Beyond each respective peak both the S-

polarized transmissivity and the ER drop precipitously, indicative of a critical effect. This

makes sense physically because the S-polarized radiation is expected to display the strongest

concentration effect by driving the SCDWs into the gap (not parallel to the gap) thereby

creating electric dipoles across the gaps. It is also consistent with the great enhancement of

the S-polarized transmissivity above the prediction of geometric optics [dashed line in Fig

4-10(a)], which justifies the label "EOT" for all spot frequencies except 1000 GHz. However,

note that EOT only occurs beyond a threshold fill factor value that rises with increasing

frequency: FF = 25% for 104 GHz, 45% for 275 GHz, and 75% for 530 GHz. This is caused

by the continuous drop in transmissivity with frequency, independent of fill factor, associated with absorptive loss in the polycarbonate substrate – see Fig 4-10(a).
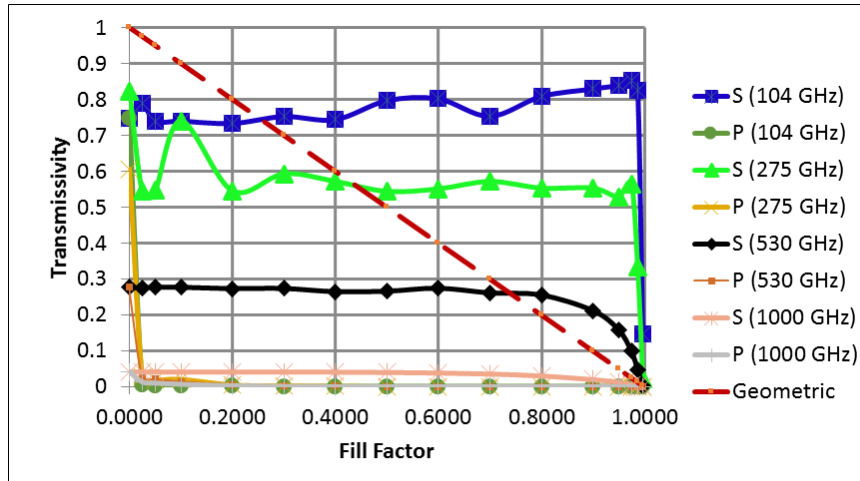
(a)
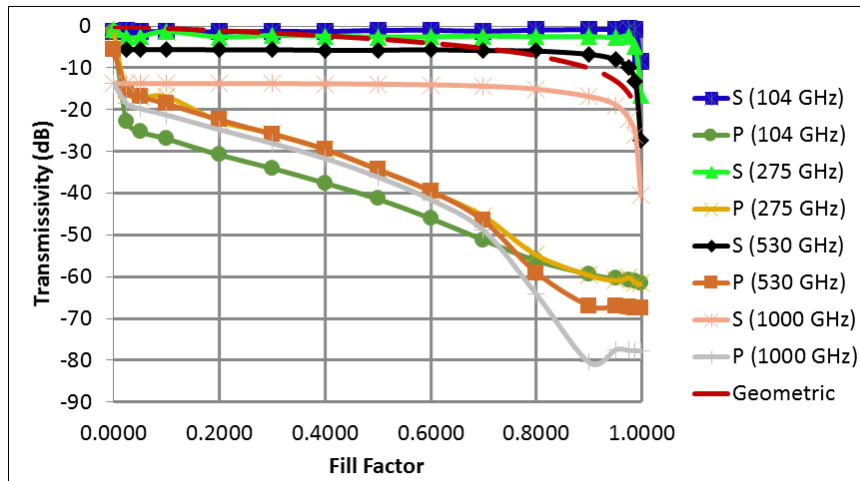
(b)

Fig 4-10: (a) Calculated transmittance versus fill factor for 104 GHz, 275 GHz, 530 GHz, and 1000 GHz.   The dashed line is the prediction from geometric optics. (b) Expanded view of (a) plotted in dB units on vertical axis to see the large difference between S- and P-polarizations.
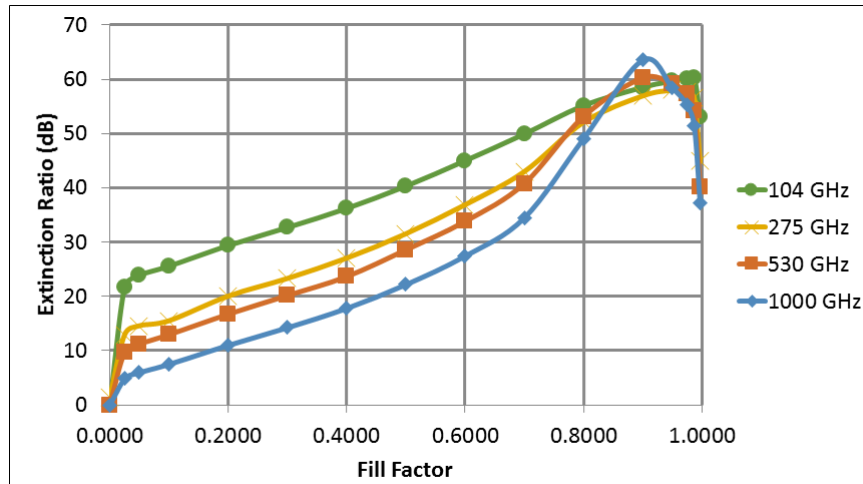
(a)
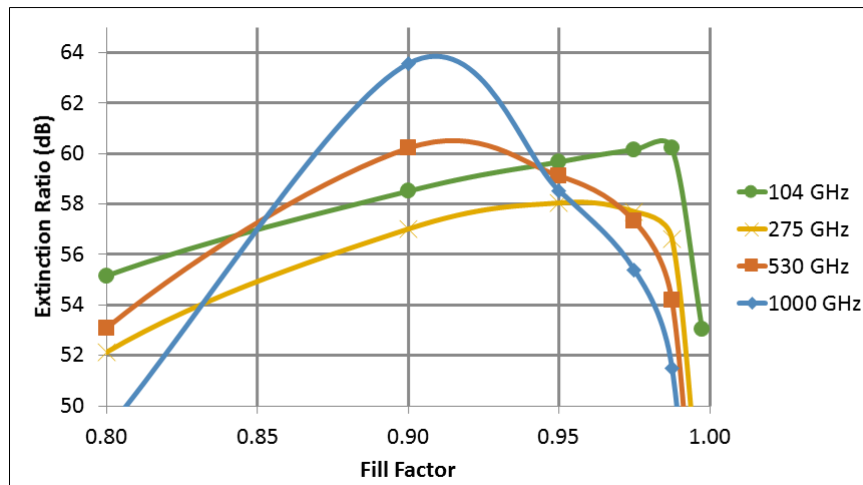
(b)

Fig 4-11: (a) Calculated extinction ratio (dB) versus fill factor for 104 GHz, 275 GHz, 530 GHz, and 1000 GHz. (b) Exploded view of (a) in the region of the extinction-ratio peak.

The phase angles were also calculated and the phase angle differences plotted. Phase angle difference is the phase difference between the two waveports with the wire grids and substrate in place minus the phase difference between the two waveports with only the substrate in place (i.e. FF = 0%). Essentially, this means that the plots have been normalized to the 0% fill factor phase difference.

The phase angle difference was observed to decrease with frequency for all fill factors. Fig 4-12 and Fig 4-13 show this behavior for S- and P-polarization respectively. For S-polarization, the phase angle differences are all negative and decreases linearly for low fill factors. At higher fill factors, higher order terms become noticeable. This may be interpreted as the phases of the currents generated on the wire surfaces leading the phases of the voltages generated across the gaps. The currents lead the voltages and hence also lead the electric fields, thus the presence of the wire grid is generating a negative phase difference similar to that seen in a capacitor. This makes sense physically for S-polarization as the surface currents flow across the wires and along the gap walls. For P-polarization, the phase differences are positive for fill factors of 90% or less. The positive phase difference indicates the surface currents generated on the wires lag the gap voltage and hence also the electric fields. This is indicative of an inductive effect. At very high fill factors a phase shift occurs and the phase differences become negative (capacitive). This is the behavior seen in LC tank circuits.
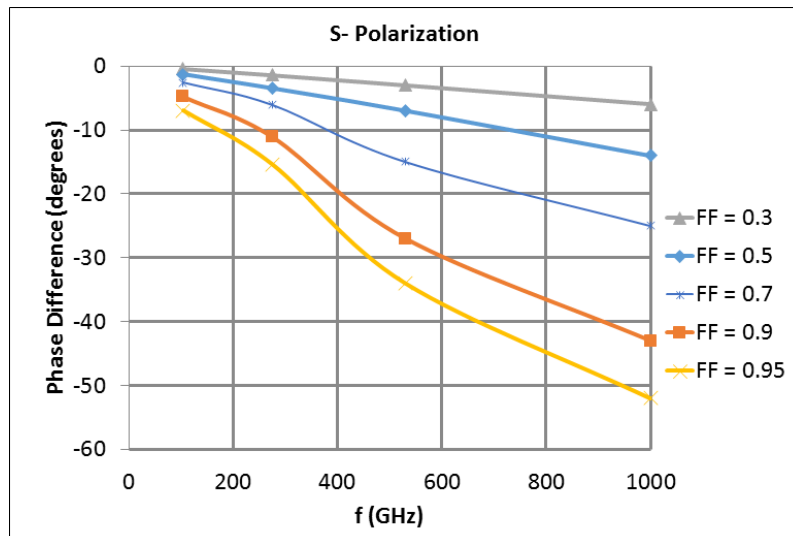
Fig 4-12: Phase angle differences for various fill factors versus frequency, S-polarization

81
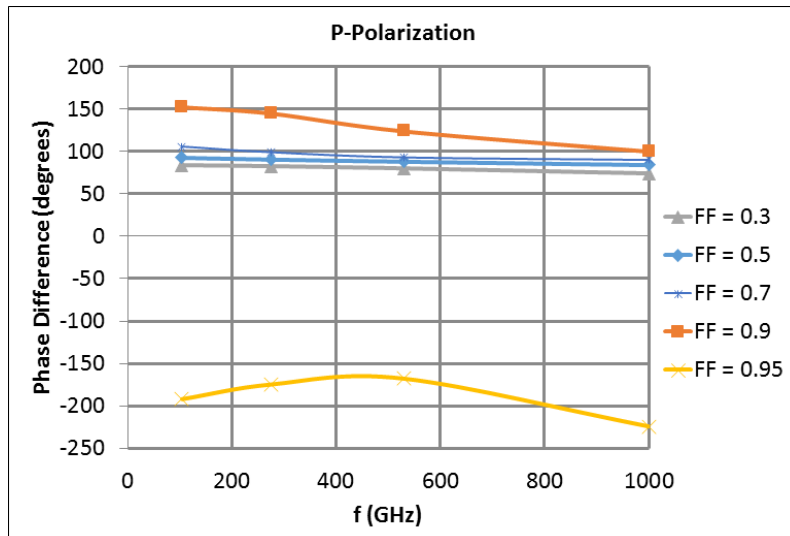
Fig 4-13: Phase angle differences for various fill factors versus frequency, P-polarization.

The behavior of the phase angle with changing fill factors was also calculated and plotted. Fig 4-14 shows the phase angle difference versus fill factor. Fig 4-15 and Fig 4-16 show the phase difference versus fill factor for the S- and P-polarizations separately. For S-polarization, the phase difference increases monotonically in the negative sense with increasing fill factor. Again this is the capacitive effect noted earlier for S-polarization. The effect increases with increasing fill factor since the capacitance across the gaps increases as the gaps get smaller. Phase difference also increase in the negative sense with increasing frequency in agreement with Fig 4-12. For P-polarization, the phase difference initially increases with increasing fill factor. Then, between 90 and 95% fill factor, a large negative phase shift occurs. This is in agreement with Fig 4-13. Evidently, at somewhere between 90 and 95% fill factor, a resonance point is reached where the impedance effect switches from inductive to capacitive and the currents no longer lag but lead the voltages and electric fields. Again, this is the behavior seen LC tank circuits.

82
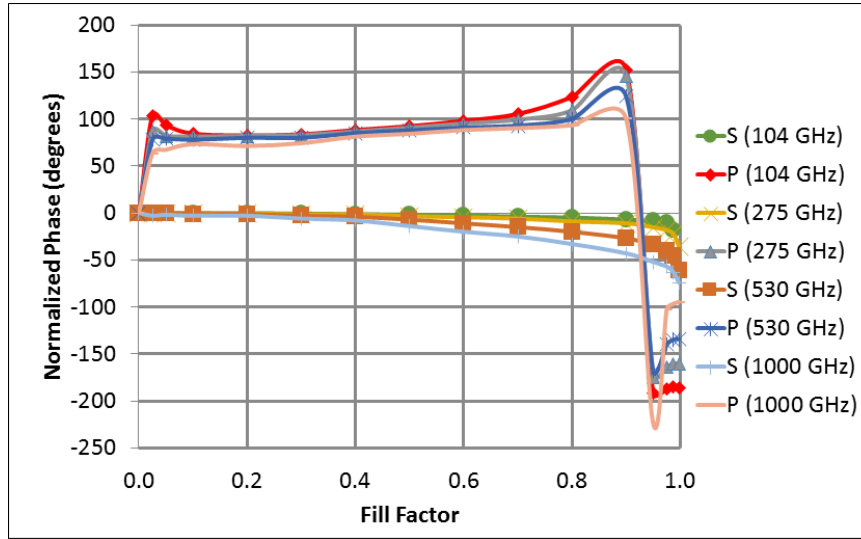
Fig 4-14: Calculated phase angle difference versus fill factor for 104 GHz, 275 GHz, 530 GHz, and 1000 GHz S- and P-polarizations.
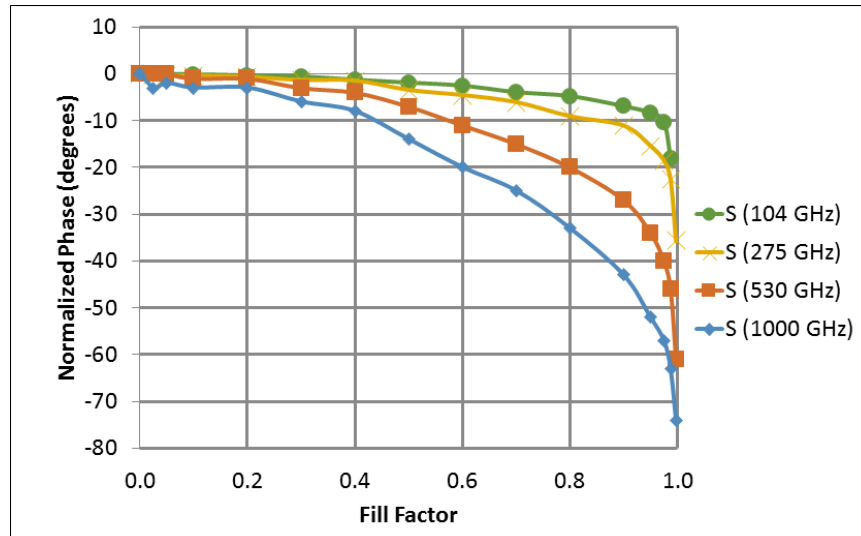
Fig 4-15: Calculated phase angle difference versus fill factor for 104 GHz, 275 GHz, 530 GHz, and 1000 GHz S-polarization.
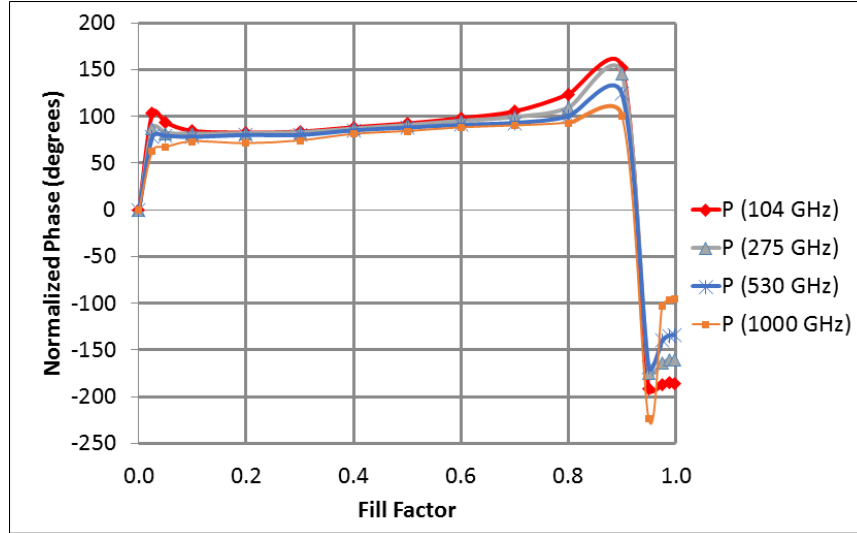
Fig 4-16: Calculated phase angle difference versus fill factor for 104 GHz, 275 GHz, 530 GHz, and 1000 GHz P-polarization.

The resonant behavior of the phase for P-polarization, as seen in Fig 4-16, motivated some further investigation. The wire grid self-resonant frequency was calculated for various fill factors. Self-resonance was modelled using the lumped circuit parameters of specific sheet inductance and specific gap capacitance as given by

$$f_0 = \frac{1}{2\pi\sqrt{L_s C_g}}$$

(4.38)

where L_s and C_g are the specific sheet inductance and the specific gap capacitance respectively.

The specific sheet inductance was modelled by adapting the formula given by Ulaby [80] for a solid transmission line conductor. The formula was normalized to H/m^2 units to give the specific sheet inductance and was made proportional to the fill factor since the wire grid as a whole is not a solid conductor. The end result was

$$L_s = \frac{ff}{2l^2}\sqrt{\frac{\mu_0}{\pi\sigma f}}$$

(4.39)

84

where ff is the fill factor, l is the wire grid period, μ_0 is the permittivity of free space, σ is the conductivity of the metal, and f is the frequency. The units are H/m^2. The use of a constant conductivity is justified because the change in σ is negligible over the frequencies of interest (see Fig 4-3). The specific sheet inductance was calculated and plotted versus fill factors from 0 to 99.75% for four spot frequencies: 104 GHz, 275 GHz, 530 GHz, and 1000 GHz. The results are shown in Fig 4-17. As is expected, the relationship between the specific sheet inductance and the fill factor is linear and increases with increasing fill factor. This makes sense physically since increasing the fill factor means increasing the metal content thus increasing inductance. In the limit of FF = 100%, the wire grid would no longer be a grid but a solid plate and (4.39) would correspond to Ulaby's formula normalized to specific sheet inductance.
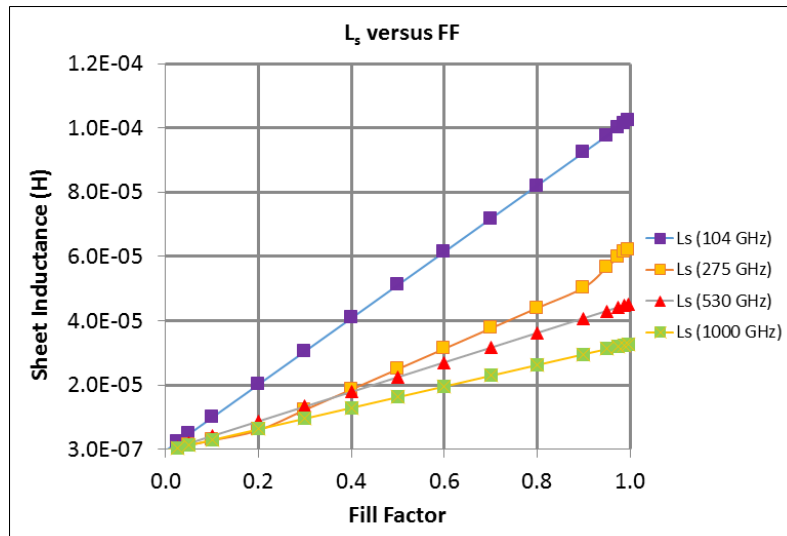
Fig 4-17: Specific sheet inductance versus fill factor for spot frequencies of 104 GHz, 275 GHz, 530 GHz, and 1000 GHz.

The specific gap capacitance was derived as follows. From transmission line theory, the resonant frequency of a transmission line is given by [80]

$$\omega = \frac{1}{\sqrt{L'C'}} \tag{4.40}$$

where L' and C' are the transmission line inductance parameter (in H/m) and capacitance parameter (in F/m). In addition, the characteristic impedance of a transmission line can be written as

$$Z_0 = \sqrt{\frac{L'}{C'}} \tag{4.41}$$

Further, the velocity of propagation is given by [80]

$$v = \frac{1}{\sqrt{L'C'}} = c\frac{\lambda'}{\lambda_0} = \frac{c}{\sqrt{\varepsilon_e}} \tag{4.42}$$

where λ_0 is the free space wavelength, λ' is the transmission line wavelength, c is the vacuum speed of light, and ε_e is the effective dielectric constant. From (4.41) and (4.42), L' can be eliminated allowing us to solve for C'

$$(C')^2 = \frac{1}{Z_0^2 v^2} \tag{4.43}$$

Further combination with (4.42) yields

$$C' = \frac{\sqrt{\varepsilon_e}}{Z_0 c} \tag{4.44}$$

Dividing by the wire grid period transforms (4.44) into the specific gap capacitance

$$C_g = \frac{\sqrt{\varepsilon_e}}{Z_0 c l} \tag{4.45}$$

with units of F/m².

86

To determine the effective dielectric constant, ε_e, the wires in the wire grid polarizer were treated like microstrip transmission lines. From microstrip line theory [81], the effective dielectric constant can be interpreted as the dielectric constant of a homogeneous medium that would equivalently replace the air and substrate around a microstrip line. At high frequencies, such as dealt with here, the effective dielectric constant is frequency dependent. An approximation formula, developed from numerical computing, is given in Pozar [81]

$$\varepsilon_e(f) = \varepsilon_r - \frac{\varepsilon_r - \varepsilon_e(0)}{1 + G(f)} \tag{4.46}$$

where $\varepsilon_e(f)$ is the frequency dependent effective dielectric constant, ε_r is the relative permittivity of the substrate ($\varepsilon_r = 2.75$ for polycarbonate), and $\varepsilon_e(0)$ is the effective dielectric constant at DC, also given by Pozar as

$$\varepsilon_e(0) = \frac{\varepsilon_r + 1}{2} + \frac{\varepsilon_r - 1}{2} \frac{1}{\sqrt{1 + 12 d/W}} \tag{4.47}$$

where d is the thickness of the substrate (0.15 cm in this case) and W is the gap-width which varies with fill factor. In (4.46) the function $G(f)$ is a curve fitted function given by

$$G(f) = g \left(\frac{f}{f_p} \right)^2 \tag{4.48}$$

with

$$g = 0.6 + 0.009 Z_0 \tag{4.49}$$

and

$$f_p = \frac{Z_0}{8\pi d} \tag{4.50}$$

where Z_0 is the characteristic impedance and d is again the substrate thickness. For W/d > 1, which is true in all cases for this analysis, Pozar gives the follow empirical expression for the characteristic impedance

$$Z_0 = \frac{60}{\sqrt{\varepsilon_e(0)}} \ln\left(\frac{8d}{W} + \frac{W}{4d}\right) \tag{4.51}$$

Z_0 is in ohms and in all cases d and W are in to be entered in cm. Based upon these approximations, (4.46) – (4.51), the specific gap capacitance (4.45) was calculated and plotted versus fill factors from 2.5 to 99.75% for four spot frequencies: 104 GHz, 275 GHz, 530 GHz, and 1000 GHz. Fig 4-18 shows the results.
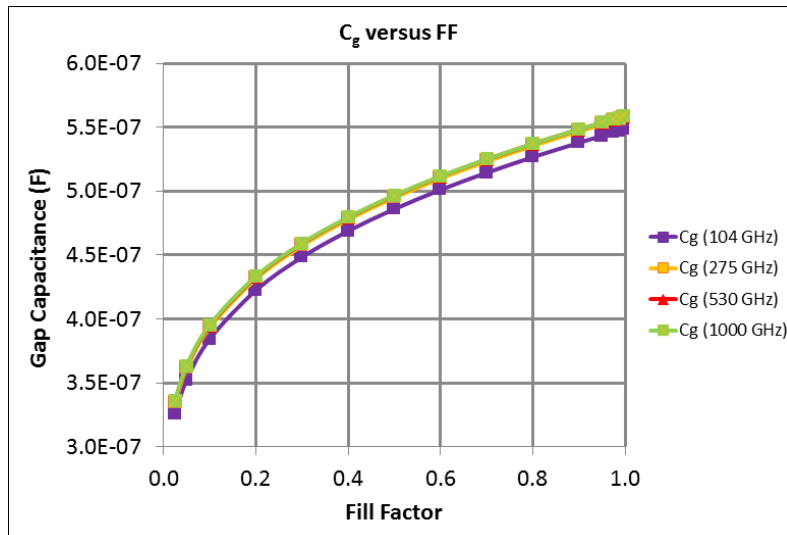
Fig 4-18: Specific gap capacitance versus fill factor for spot frequencies of 104 GHz, 275 GHz, 530 GHz, and 1000 GHz.

The specific gap capacitance increases monotonically with fill factor and increases with frequency. This makes sense physically as increasing the fill factor decreases the gap and thus increases the gap capacitance in manner similar to a parallel plate capacitance.

The combination of the calculated specific sheet inductance and the calculated specific sheet capacitance were then used to calculate the self-resonance of the structure via (4.38). Since L_s and C_g were themselves frequency dependent, the expression for f_0 was implicit. The Goal Seek function in Microsoft Excel was used to solve for f_0 at fill factors ranging from 2.5 to 99.75 %. The results are shown below in Fig 4-19. Fig 4-19 shows that the self-resonant frequency of the wire grid polarizer decreases monotonically with fill factor. This again makes sense physically because as fill factor increase, both the specific sheet inductance and the specific gap capacitance increase. Self-resonant frequencies at low fill factors are fairly high,
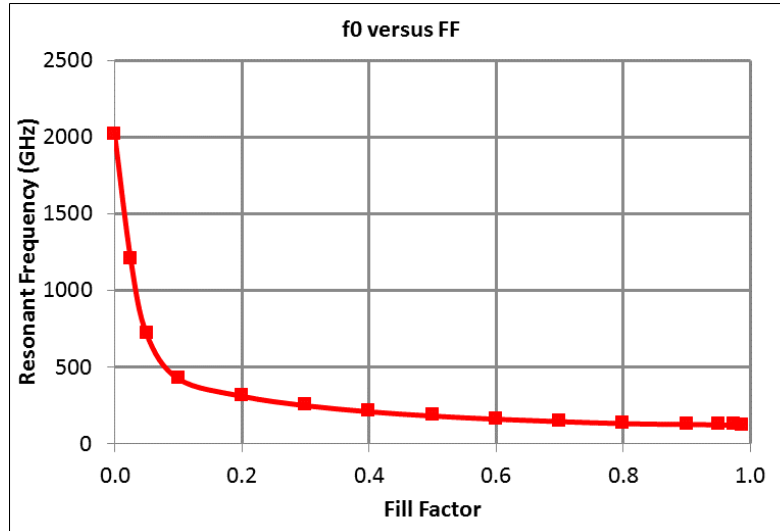
Fig 4-19: Wire grid self-resonance frequency versus fill factor calculated using the specific sheet inductance and the specific gap capacitance.

reaching over 2000 GHz for FF = 2.5%. At first, the self-resonant frequency drops sharply for low but increasing fill factors. As fill factors become larger, the self-resonant frequency changes less and less with increasing fill factor and seems to approach a constant of approximately 125 GHz at very high fill factors.

The magnitudes of the fields across the gap were also computed. An example of the calculated field magnitude for a 90% fill factor at 530 GHz is displayed in Fig 4-20. Note the increased field strength in and around the gap particularly near the gap inner walls.
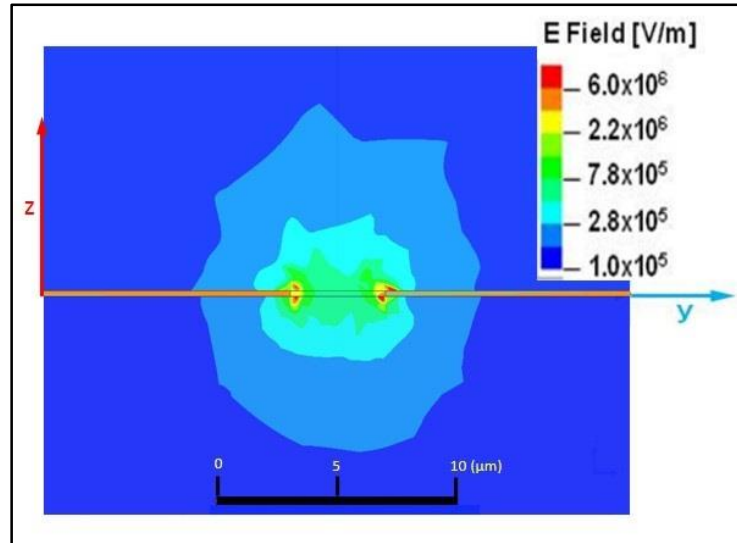
Fig 4-20: Electric field magnitude across the gap at 530 GHz, FF = 90% (4 um gap).

In addition, the enhancement of the Poynting vector magnitude, electric field magnitude, and the wave impedance at the center of the gap (x = 0, y = 20 μm center of the gap, and z = 100 nm - see Fig 4-9), was calculated for 530 GHz. The FFs ranged from 0% to 99.9%. A plot of these enhancements is shown in Fig 4-21. Note the high enhancements at high FFs. This is due to the very high energy densities confined to the gap at high FFs. The electric field energy enhancement factor reaches a maximum of more than 160, the electric field magnitude enhancement factor more than 24, and the wave impedance enhancement factor more than 13 compared to the incident free-space field.
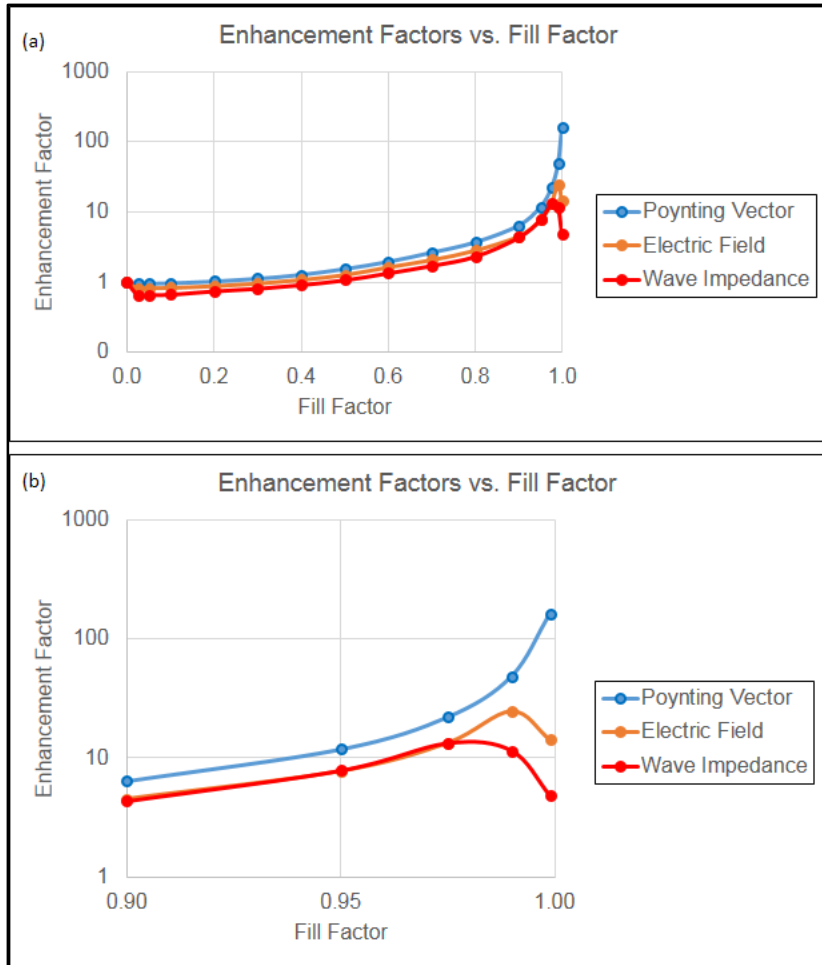
Fig 4-21: Calculated enhancement factors versus fill factor at 530 GHz for fill factors from (a) 0 to 1.0 and (b) from 0.90 to 1.0.

In addition, the fields were calculated across the gap. Fig 4-22 shows the profile of the electric field across the gap for 90% fill factor (4 um gap). The profiles for the Poynting vector magnitude and the wave impedance have a similar shape, peaking at the edges (near the metal) and having a minimum in the center of the gap. This implies that the largest field enhancements actually occur near the metal surface, at the conductor-dielectric interface, not at the center of the gap. This corresponds to the ideas presented in the SSP picture of EOT

(Section 2.5). Oscillating SCDWs on the two slit walls create the high fields in the gaps and are the main driving mechanism behind EOT in the THz region.
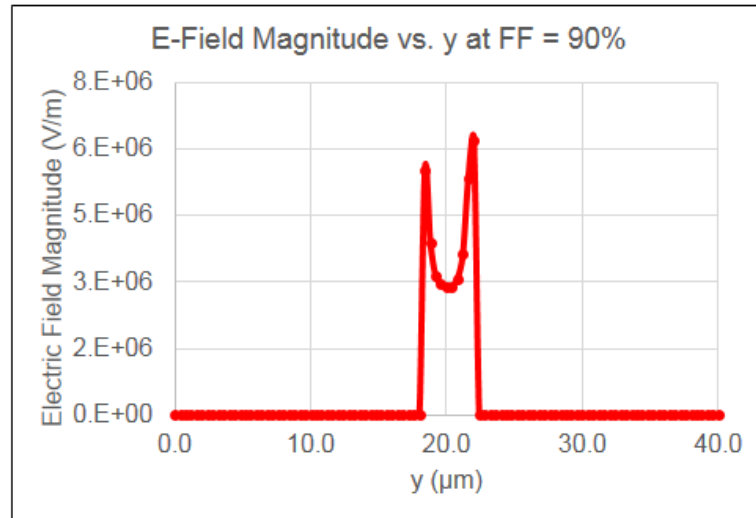
Fig 4-22: Profile of the electric field magnitude across the gap at 530 GHz, FF = 90% (4 um gap). Asymmetry of the peaks is due to asymmetric meshing in the FEM algorithm.

To investigate the predicted behavior experimentally, two wire-grid polarizers were fabricated on polycarbonate substrates with aluminum strips and fill factors of 80 and 95%.

The fabrication was done by John Mittendorf using an evaporation and etch-back process [82].

A schematic showing the steps in the process is given in Fig 4-23. The fabrication is done using a Denton DV-502B high-vacuum evaporator at a pressure of approximately 5 x 10^{-6} Torr.

The substrate is mounted at the top of the chamber. The Al is mounted at the bottom in a tungsten filament. Therefore, the substrate and the Al are in a face-to-face orientation. The initial step is to heat the Al to a temperature of approximately 1100 K, thus evaporating the Al.

The gaseous Al drifts upward contacting and sticking to the substrate. The thickness (evaporation rate) is controlled by a calibrated piezoelectric sensor. A photoresistive layer is then spun on to the sample. Next, a photo-mask is used to pattern the photoresist. The
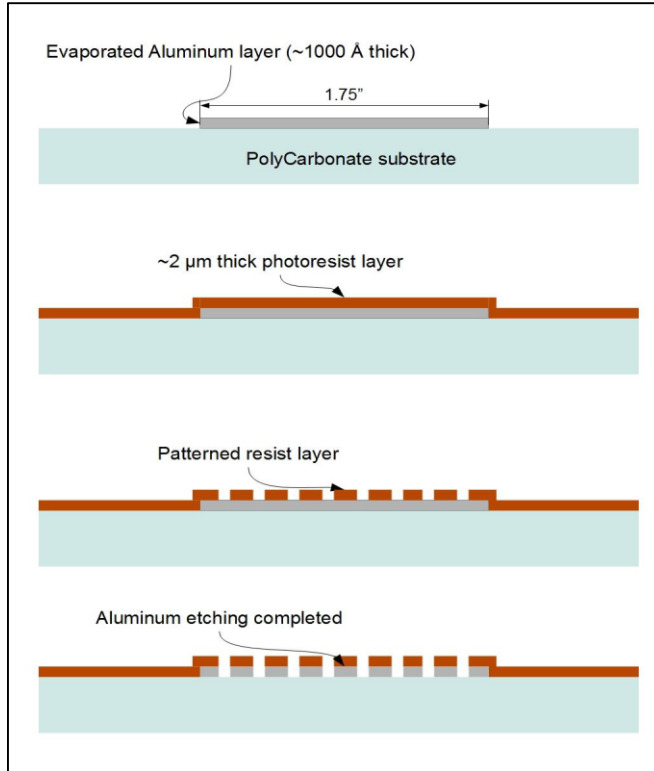
Fig 4-23: Evaporation and Etch-back process.

photoresist is then developed to remove the exposed photoresistive material. The sample is then etched to remove the exposed Al down to the substrate. Finally, the photoresist is removed to reveal the patterned Al wire-grid on top of the substrate. Two different fill factor (80% and 95%) wire-grid polarizers were fabricated using this process on a single substrate. Micrographs of the two fill factors are shown in Fig 4-24 and Fig 4-25. This multi-fill factor polarizer was mounted in an optical rotation stage as shown in Fig 4-26. Measurements of the IL and ER were carried out at spot frequencies of 104, 275, and 530 GHz using solid-state oscillators coupled to free space with linearly-polarized horn antennas, and waveguide-mounted zero-bias Schottky rectifiers also coupled by horn antennas. The experimental results for ER and IL are plotted in Fig 4-27. The experimental results are qualitatively consistent

with the calculations. The ER in Fig 4-27 increases with fill factor at each of the three frequencies, and also increases with frequency at a given fill factor.
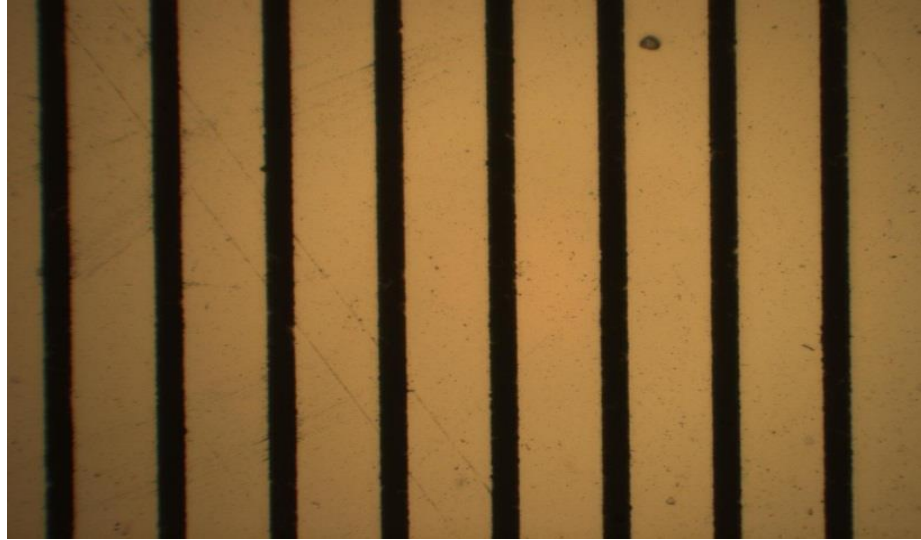
Fig 4-24: 80% fill factor. Wire-grid period is 40 μm. Strip width is 32 μm. Acknowledgement to John R. Middendorf for fabrication.
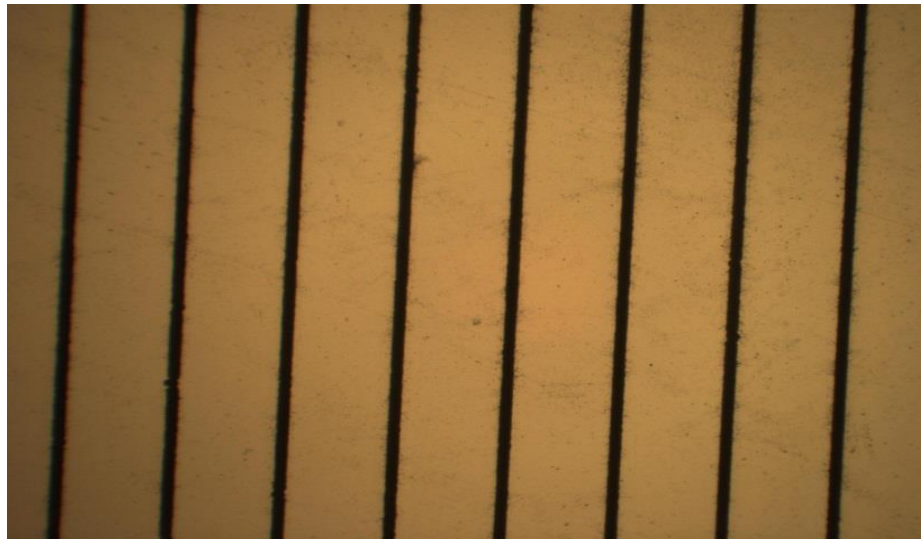
Fig 4-25: 95% fill factor. Wire-grid period is 40 μm. Strip width is 38 μm. Acknowledgement to John R. Middendorf.

Fig 4-26: Fabricated wire grid polarizer mounted in an optical rotation stage. Acknowledgement to John R. Middendorf.
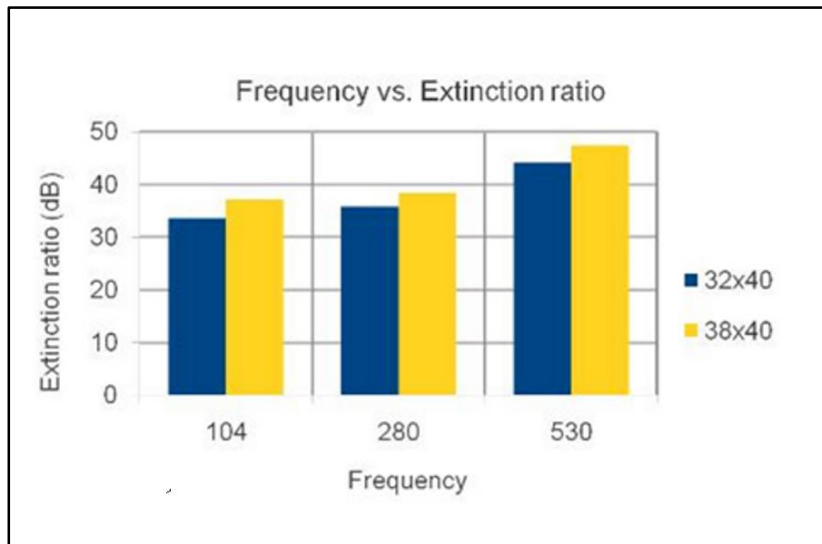
Fig 4-27: The experimental extinction ratios of two different fill factors measured at three spot frequencies.

Quantitatively the experimental ER data is lower than the simulated values by roughly 20 dB, depending on fill factor and frequency. This is most likely attributed to materials effects such as excess sheet resistance in the aluminum strips used for the present structures. Aluminum oxidizes rather quickly. The sheet resistance of the Al is increased by oxidation. It is assumed that some oxidation did occur on the present structures. Nevertheless, the

extinction ratios that we have demonstrated are, to the best of our knowledge, the highest values ever reported for a substrate-mounted polarizer in the 100-530 GHz region.

In conclusion, even in the MM-Wave and THz regions, where surface plasmons cannot be excited directly, plasmon-like surface waves (SSPs or "spoof" plasmons) are allowed by Maxwell's equations and the boundary conditions which when properly designed for, lead to huge improvement in the performance of passive components like wire-grid polarizers. The "proper design" appears to utilize a very high fill factor of metal to get high concentration of the E-fields in the dielectric gaps. This runs against conventional wisdom and perhaps intuition but is proven to be true.

4.3.   The Effective Fill Factor Phenomenon

The Effective Fill Factor (EFF) concept was the product of several discussions between John Middendorf and this author. The general idea was to explore whether there was a way to reduce the fill factor but still maintain the high extinction ratios seen in wire-grid polarizers [83], [84], [85] as described in the Section 4.2.

A baseline wire-grid polarizer design was defined as a 1D structure with translational symmetry such as shown in back in Fig 4-9. The alternative approach was the effective fill factor or compound [86] design by which each metal strip comprising the baseline design is replaced with several thinner strips separated by small air gaps, such as shown in Fig 4-28.

THz wire-grid polarizer designs consisted of aluminum strips lying on single-crystal quartz which replaced the polycarbonate as the substrate material. Single-crystal quartz has a lower insertion loss than polycarbonate in the frequencies investigated. In addition, the
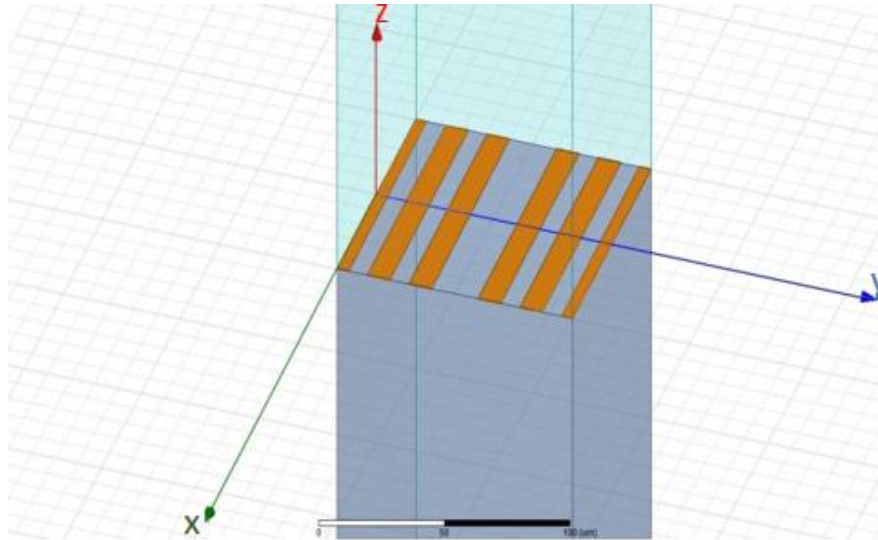
Fig 4-28: EFF design wire-grid polarizer unit cell, 80% effective fill factor, 48% actual fill factor. Compare to Fig 4-9.

insertion loss in polycarbonate increases with frequency [83] while that of crystal quartz is relatively flat throughout this frequency band [82]. Thus, crystal quartz offers better performance than the polycarbonate in the frequencies of interest.

The four baseline designs and two EFF designs used a period of 100 μm. The first baseline designs used 80% (Fig 4-9) and 48% (Fig 4-29) fill factors. The EFF design used an 80% EFF, the actual FF being only 48% (Fig 4-28). The second EFF design used a 50% EFF, the actual fill factor being only 30%. Full-wave numerical simulations using HFSS were performed on these designs from 100 to 1000 GHz in steps of 5 GHz. The Drude model from Section 4.2 and the Palik data [87] (see Section 4.4 for a detailed discussion) were used in HFSS for modeling Al and single-quartz crystal respectively.

The simulation results predicted that the same physical effects (EOT, high extinction ratios, and E-field enhancements) can be realized in both the baseline and the EFF components. The EFF component's actual fill factor is reduced to 48% (30%). Nevertheless, its extinction

97

ratio is very close to that seen in the 80% (50%) fill factor baseline design and exceeds that of the 48% (30%) fill factor baseline design, particularly at higher frequencies. This is shown in Fig 4-30 (Fig 4-31). This is explained with the help of Fig 4-32 through Fig 4-35.
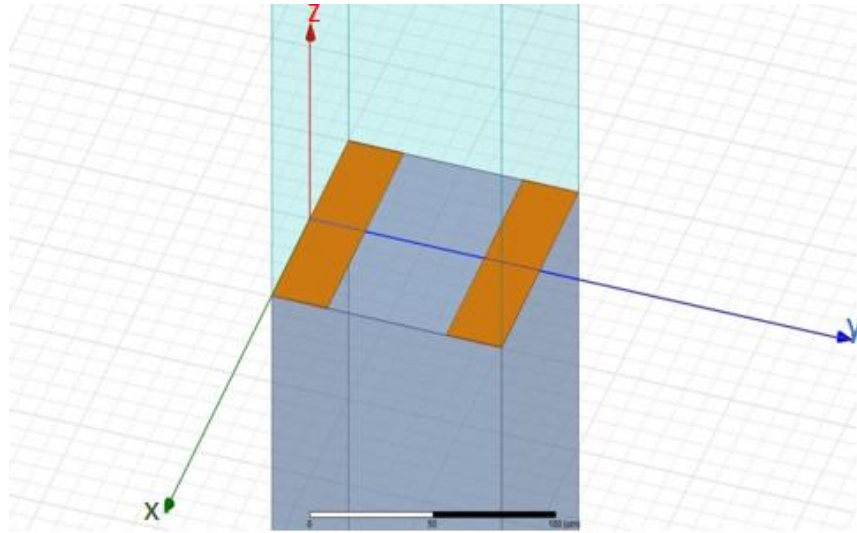
Fig 4-29: Baseline design wire-grid polarizer unit cell, 48% fill factor.
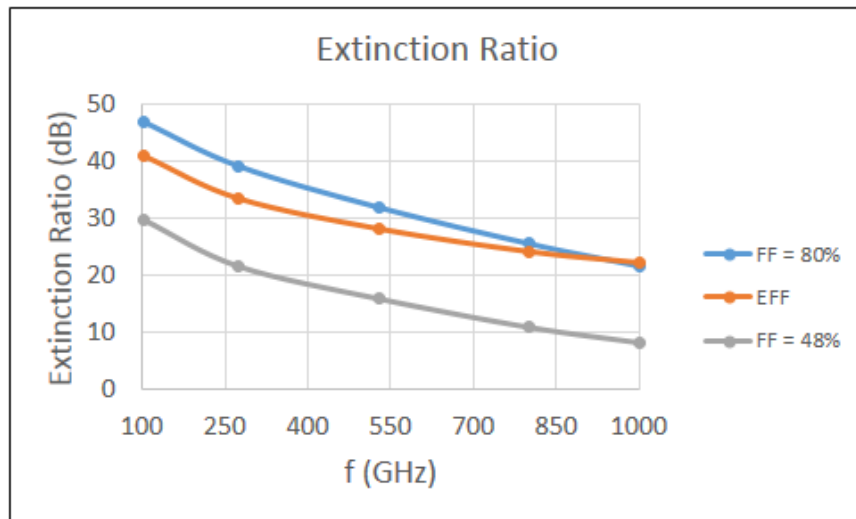
Fig 4-30: Calculated extinction ratio for baseline (80% and 48%) and EFF designs with 80% effective fill factor, 48% actual fill factor.
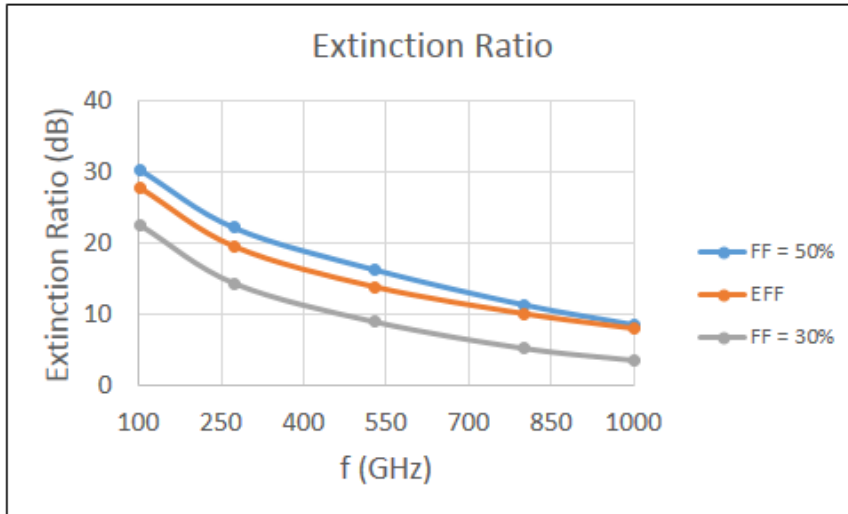
Fig 4-31: Calculated extinction ratio for baseline (50% and 30%) and EFF designs with 50% effective fill factor, 30% actual fill factor.
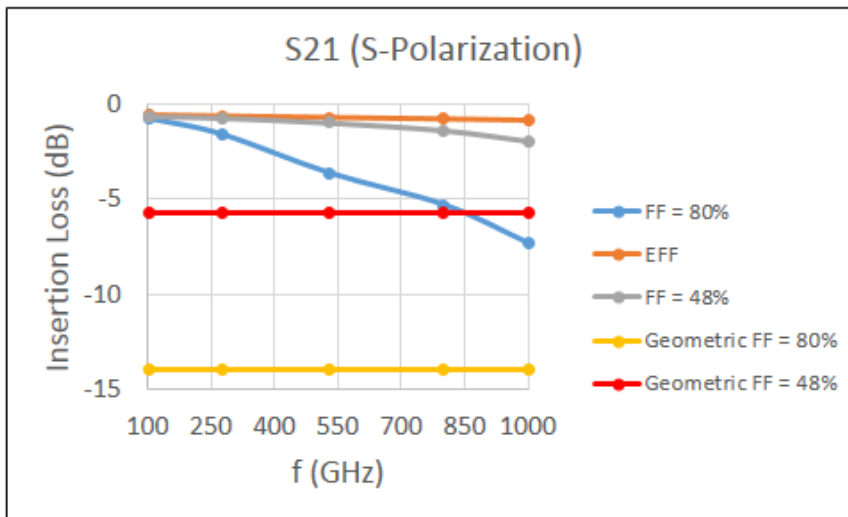
Fig 4-32: Calculated insertion losses (S-polarization) for baseline (80% and 48%), EFF designs, and based on geometrical optics.
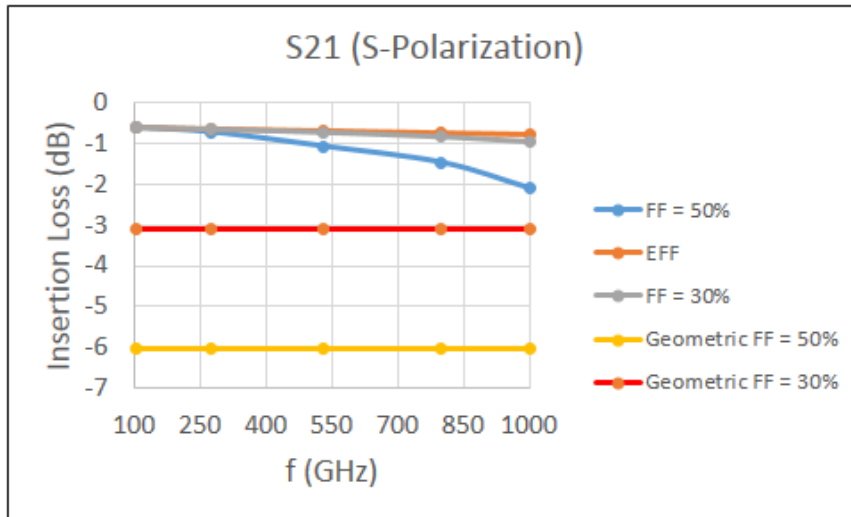
Fig 4-33: Calculated insertion losses (S-polarization) for baseline (50% and 30%), EFF designs, and based on geometrical optics.
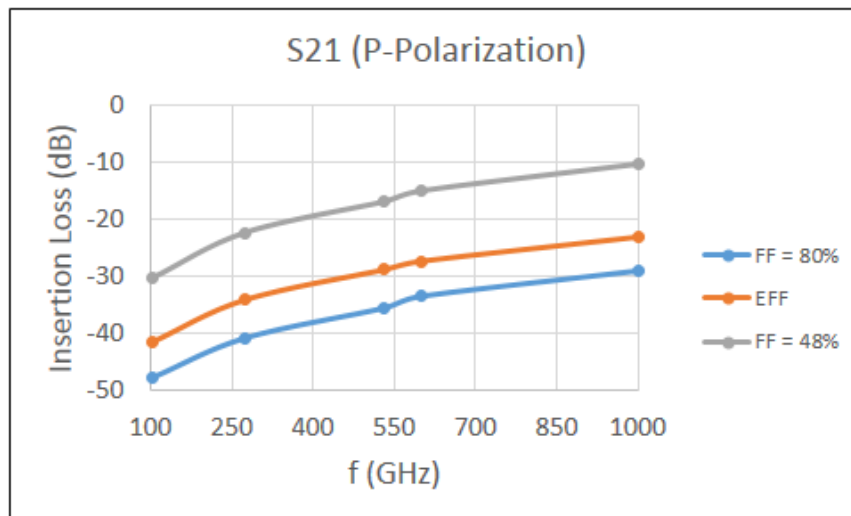
Fig 4-34: Calculated insertion losses (P-polarization) for baseline (80% and 48%) and EFF designs.
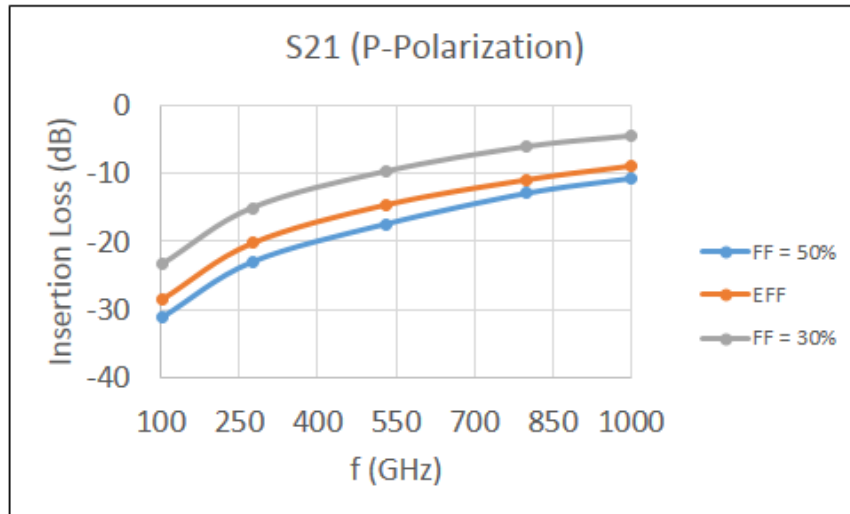
Fig 4-35: Calculated insertion losses (P-polarization) for baseline (50% and 30%) and EFF designs.

Fig 4-32 (Fig 4-33) shows that for S-polarization, the EFF design exhibits lower insertion losses (higher transmission) than the 80% (50%) FF baseline design as frequency increases. Indeed, the EFF insertion losses are equal the 48% (30%) FF baseline design insertion losses and become slightly better with increasing frequency. Fig 4-34 (Fig 4-35) shows that for P-polarization, the EFF design exhibits insertion losses in between those of the 80% (50%) FF baseline design and those of the 48% (30%) FF baseline design. Finally, Fig 4-32 (Fig 4-33) shows S-polarization transmission that is greater than that predicted by geometric optics for the 80% (50%) fill factor and for the 48% (30%) fill factor designs up to 1000 GHz. The simulations predict the EFF designs will produce EOT. In fact, EOT is produced in from the 80% EFF design but not produced from the 80% fill factor baseline design.

The phase angle difference, as defined in Section 4.2, was also calculated and plotted. Fig 4-36 and Fig 4-37 show the phase angle difference between the simulation domain

waveports versus frequency for S- and P-polarization for the 80% and 48% baseline designs

as well as the 80% EFF design. As can be seen in from plots, the phase angle difference
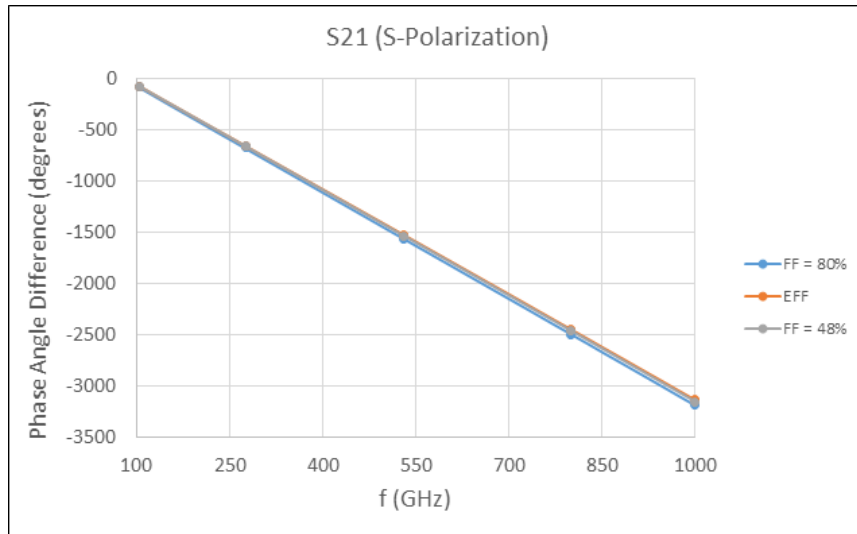
Fig 4-36: S-Polarization phase angle difference versus frequency for baseline (80% and 48 %) and EFF designs.
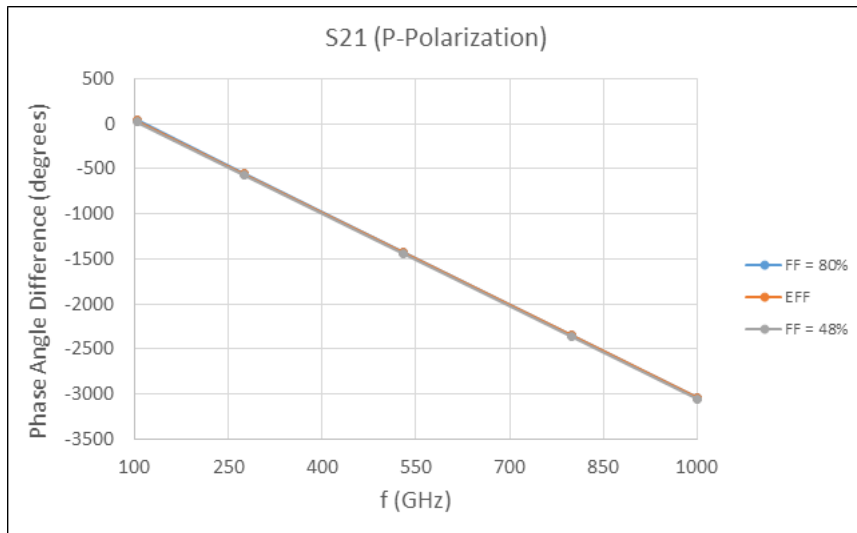
Fig 4-37: P-Polarization phase angle difference versus frequency for baseline (80% and 48 %) and EFF designs.

decreases monotonically with increasing frequency for both polarizations. The phase angle differences for S- and P-polarization for the 50% and 30% baseline designs and the 50% EFF design were also calculated. Plots of these phases angle differences are not shown as they are essentially the same as Fig 4-37 and Fig 4-38.

To investigate the predicted behavior of the EFF strip-grid polarizers experimentally, two polarizers were fabricated (John R. Mittendorf) with aluminum strips on single-crystal quartz substrates using the evaporation and etch-back process described in Section 4.2. A baseline design with a period of 40 μm and fill factor of 75% and an EFF design with a period of 40 μm and fill factor of 40% (EFF = 75%) were compared. The unit cell of the baseline design consisted of one 30 μm wide aluminum strip and an adjacent 10 μm wide gap. The unit cell of the EFF design consisted of group of eight 2 μm wide aluminum strips spaced 2 μm apart from each other with one 10 μm wide gap separating the group of strips from other groups. Fig 4-38 shows the baseline and EFF polarizers. Measurements of the S-polarization and P-polarization transmissions were carried out using a THz photomixing spectrometer. Plots of the measured transmissions for the baseline and EFF polarizers are shown in Fig 4-39. The extinction ratios, and S-, and P-polarization transmissions are shown in Table 4-1, Table 4-2, and Table 4-3 respectively at spot frequencies of 104, 275, 530 and 720 GHz. The behavior predicted by the simulations is seen in the measured data to within a few dB.

The S-polarization transmission slightly decreases with frequency. The P-polarization transmission increases with frequency. The extinction ratio decreases with frequency. In addition, the S-polarization transmission is much higher than would be expected from calculations using geometrical optics. EOT is seen in the experimental results. Thus, in simulation and experiment, the behaviors of the baseline and the EFF polarizers are very

similar qualitatively and quantitatively to within a few dB. The experimental results confirm

the simulation predictions.
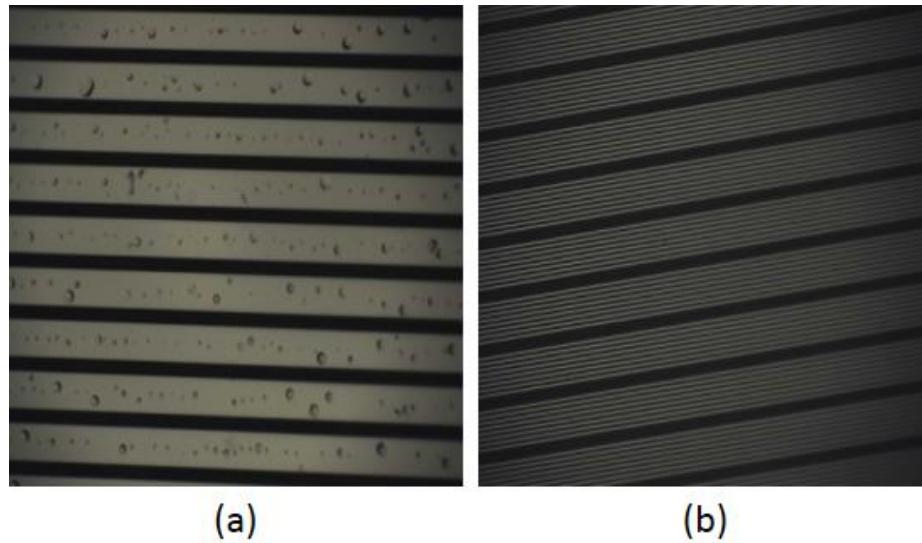
Fig 4-38: a) Baseline and (b) EFF wire-grid polarizers fabricated using aluminum strips on a quartz substrate. Acknowledgement to John R. Middendorf for fabrication.
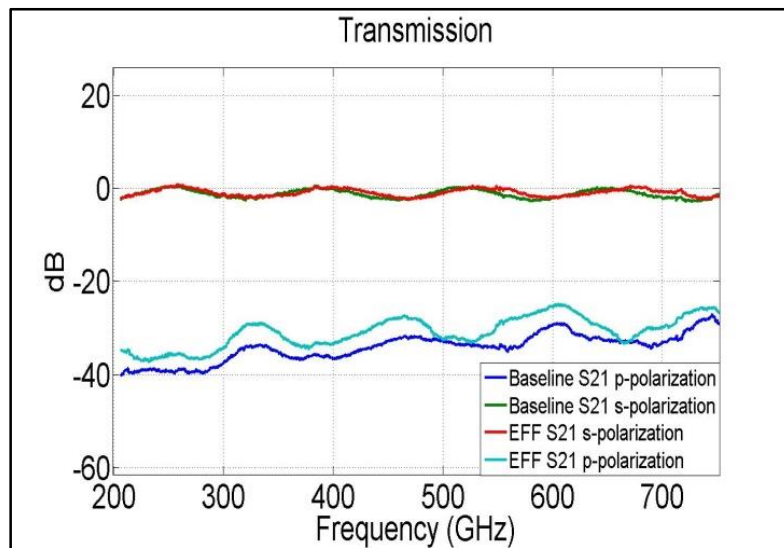
Fig 4-39: Measured S- and P-polarization transmission for baseline and EFF wire-grid polarizers.

f (GHz)	FF = 75%	EFF = 75%, FF = 40%
275	35.7 dB	38.9 dB
530	32.6 dB	33.7 dB
720	28.1 dB	26.0 dB

Table 4-1: Measured extinction ratios for baseline and EFF designs.

f (GHz)	FF = 75%	EFF = 75%, FF = 40%
275	-0.6 dB	-0.1 dB
530	-0.2 dB	-0.1 dB
720	-2.5 dB	-1.0 dB

Table 4-2: Measured S-polarization transmission for baseline and EFF designs.

f (GHz)	FF = 75%	EFF = 75%, FF = 40%
275	-36.3 dB	-39.0 dB
530	-32.8 B	-33.8 dB
720	-30.6 dB	-27.0 dB

Table 4-3: Measured P-polarization transmission for baseline and EFF designs.

In summary, the EFF designs use less metal that the baseline designs but have better transmission properties in S-polarization, especially as frequencies increase. Meanwhile, the P-polarization transmissions of the EFF designs are not quite as good as the higher fill factor baseline designs but still an improvement over designs of equal fill factor. Nonetheless, the EFF design's extinction ratios are still very good and match those of the higher fill factor baseline designs (80% and 50%) as frequency increases. Thus, the EFF concept may be very

useful in future work and applications where better transmission properties are required but high extinction ratios must be maintained.

4.4. A THz Wire-Grid Polarizer with Bridges

In this section another new type of wire-grid polarizing structure is presented, a THz wide-band wire-grid polarizer with metallic bridges. This device functions as a wide-band polarizer to incident THz radiation. In addition, the metallic bridges allow the device to function as a transparent electrode when a uniform electric field creates a DC bias across it while forcing DC currents to take a circuitous "zig-zag" path across the structure due the offset in bridge positions in adjacent slots.

The THz wire-grid polarizer is a structure which consists of a thin metal strips separated by a periodic slit pattern, mounted on a dielectric substrate. An exemplary polarizer discussed in this study uses slits that are 4 micrometers (μm) wide and 12 μm apart. The thickness of the metal film is 0.5 μm. The thickness of the substrate is 500 μm. The slits are not continuous across the entire length of the structure. The continuity of the slits is periodically broken by small metal tabs (bridges) interconnecting the metal on either side of the slits. The thickness of the tabs is equal to that of the metal strips. The positions of the bridges in adjacent slits are offset by one half of the bridge period. A diagram of the unit cell for the structure is shown in Fig 4-40.

A Cartesian coordinate system is used to facilitate the description, with the origin being at the upper left-hand corner. By design, the device is periodic in both the x and the y directions. The x-period defines the positioning of the bridges and is given by x5 in Fig 4-40.
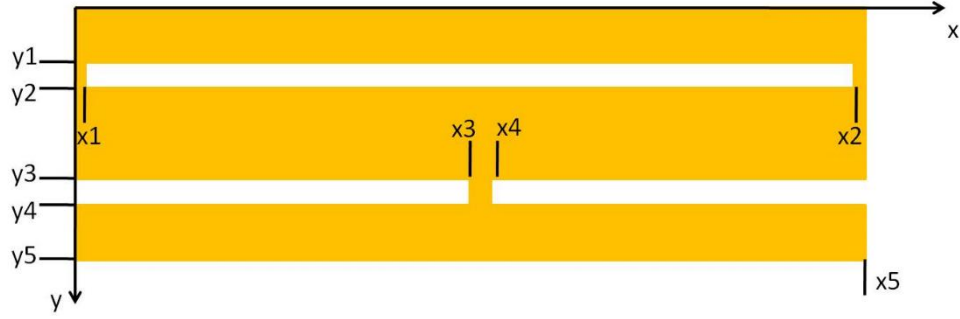
Fig 4-40: Unit cell diagram of the wire grid polarizer with bridges.

The y-period defines the spacing and location of the slots. It is given by y5 in Fig 4-40. In the x direction, the distance between x2 and x1 determines the slit length. The bridge length is given by the distance from x4 to x3; for this example that dimension is 2 μm. In the y direction, the distance between y2 and y1, and y4 and y3 defines the slit and bridge widths. The distance between y3 and y2 determines the strip width. Note that the following relationships between these x and y locations must hold:

$$x5 = (x2 - x1) + (x4 - x3) \tag{4.52}$$

$$\mathbf{y5} = 2(\mathbf{y2} - \mathbf{y1}) + 4\mathbf{y1} \tag{4.53}$$

$$\mathbf{y4} - \mathbf{y3} = \mathbf{y2} - \mathbf{y1} \tag{4.54}$$

$$\mathbf{y1} = \mathbf{y5} - \mathbf{y4} \tag{4.55}$$

$$\mathbf{y3} - \mathbf{y2} = 2\mathbf{y1} \tag{4.56}$$

The metal used for the film is gold. Gold was selected due to its high conductivity in the THz frequency range. The substrate material is single-crystal quartz. Despite having an absorption resonance at 3.84 THz (128 cm^{-1}) [88], crystal quartz has excellent transmittance in

107

the lower THz region. In addition, commercially available quartz crystal wafers exhibit very flat and smooth surfaces that make them well suited for the micro-fabrication and deposition techniques needed to produce this structure.

Full-wave electromagnetic simulations were performed on the structure using HFSS. HFSS was used to determine the transmittance ($|S_{21}|^2$) and reflectance ($|S_{11}|^2$) for incident radiation polarized perpendicular (S) and parallel (P) to the strip axis (x-axis). The frequency of the incident radiation was swept from 100 GHz to 4.0 THz in steps of 1 GHz. Periodic boundary conditions were applied. Floquet ports were used to excite the structure with electromagnetic radiation. The incoming radiation was at normal incidence in all simulations.

To improve accuracy, losses in the gold were accounted for by using a look-up table for the gold dielectric function generated from the Drude model. To further improve accuracy, a look-up table for the crystal-quartz was constructed for the real and imaginary parts of the dielectric function as calculated from the index of refraction and extinction coefficient from Palik [87]. Palik's data ranged in frequency from 300 GHz to 4.2 THz for n and 900 GHz to 4.2 THz for k. A single additional data point for n at 100 GHz and three additional data points for k at 100, 300, and 600 GHz were extrapolated. An examination of Palik's crystal-quartz data shows that this is a reasonable thing to do. From Palik, neither n, the index of refraction, nor k, the extinction coefficient, changes significantly for $f \leq 1500$ GHz. Table 4-4 below is taken from [87]. This approach is accurate from a solid state physics standpoint as well whereby n and k vary negligibly with respect to frequency at a decade or more below the optical phonon resonance [39], which for crystal quartz occurs at a frequency of 3.84 THz at room temperature [88].

The device was optimized for use at 1 THz (λ = 300 µm). To avoid any significant diffraction effects at 1 THz, the initial design used a unit cell period in the x direction of 102 µm, well below 300 µm. After the first simulation results were analyzed, longer periods were investigated. The dimensions for the first five designs are summarized in Table 4-5.

f	n	k
100 GHz	2.1061*	7.96e-4*
300 GHz	2.1063	7.96e-4*
600 GHz	2.1070	7.96e-4*
900 GHz	2.1081	7.96e-4
1200 GHz	2.1096	7.96e-4
1500 GHz	2.1114	7.96e-4

Table 4-4: Index of refraction (n) and extinction coefficient (k) versus frequency from Palik [87] or (*) extrapolated from Palik.

	Design 1	Design 2	Design 3	Design 4	Design 5
x Period (µm)	102	127	157	None	187
y Period (µm)	16	16	16	16	16
Slot x dimension (µm)	100	125	155	None	185
Slot y dimension (µm)	4	4	4	4	4
Film thickness (µm)	0.5	0.5	0.5	0.5	0.5

Table 4-5: Design geometries.

The S-polarization transmittances vs frequency for Designs 1, 2, and 3 are shown below in Fig 4-41. All vertical axes are scaled in decibels (S_{21}[dB] $\equiv$ 20*$\log_{10}$[S_{21}]). The P-polarization transmittances for Designs 1, 2, and 3 are shown in Fig 4-42. There is no

significant difference between the P-polarization transmittances of the three designs. Note, the absorption resonance of bulk crystal quartz can be seen at 3.84 THz in both Fig 4-41 and Fig 4-42, as expected.

Fig 4-41: Calculated transmittance for S-polarization. THz wire-grid polarizers with bridges, Designs 1-3.
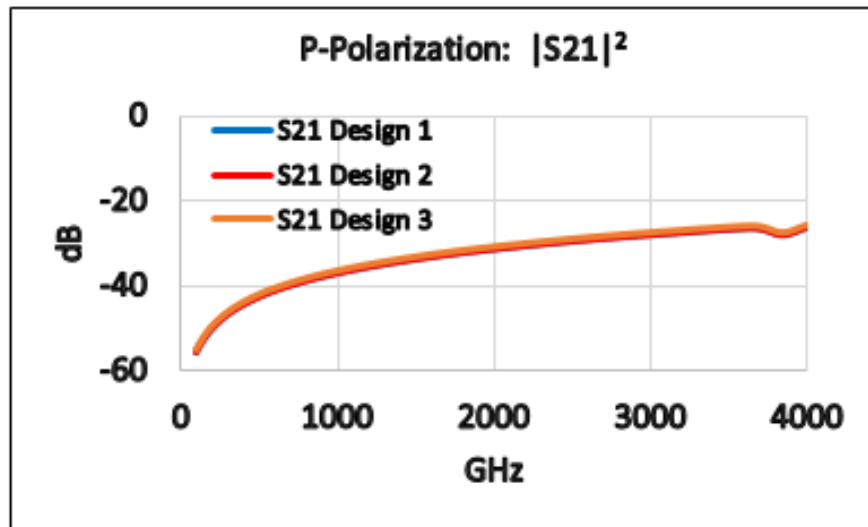
Fig 4-42: Calculated transmittance for P-polarization. THz wire-grid polarizers with bridges, Designs 1-3.

In Design 1, the transmittance response for S polarization displays a passband-like behavior having a 3 dB bandwidth of approximately 2.48 THz. In contrast, the P-polarized radiation spectrum shows no structure; transmittance increases monotonically from -60 to -30 dB over the swept frequency range. At 1 THz, the calculated extinction ratio is approximately 36.2 dB. A second feature of note in the S-polarized transmittance is the sharp resonant notch at 2.76 THz. The magnitude of the transmittance in the center of the notch is -13.7 dB. The quality (Q) factor is the ratio of the energy stored to the energy dissipated per cycle. It is given by

$$Q = \frac{f_0}{\Delta f} \qquad (4.57)$$

where f_0 is the notch center frequency and Δf is the notch 3 dB bandwidth. In Design 1 the Q factor is 102. While the notch depth is not enough to act as a good spectral filter, it does define the upper extent of the width of the -3 dB pass band below it.

Simulation of Design 2 shows that modification of the long dimension (x-axis) period has a strong effect on the spectral location of the notch. The S-polarization 3 dB bandwidth decreases from 2.48 THz to 2.08 THz. The center frequency of the notch feature moves from 2.76 THz to 2.28 THz. The depth of the notch decreases from 13.7 dB to 6.9 dB and the quality factor from 102 to 10.2. There is no change in the P-polarized transmittance. The extinction ratio at 1 THz was 36.4 dB, slightly better than in Design 1.

In Design 3, the S-polarization 3-dB bandwidth of the structure is further reduced to 1.71 THz. In addition, the center frequency of the notch feature moves down to 1.88 THz, the depth decreases to 5.6 dB, and its quality factor drops to 6.7. Nevertheless, the extinction ratio

at 1 THz for Design 3 was 36.0 dB, still very good because there is again no change in the P-polarized transmittance.

Fig 4-43 and Fig 4-44 show the transmittance for S- and P-polarization of Design 4, where the bridges were removed. There is no change in the P-polarization response, but the S-polarization changes drastically. The resonant notch feature disappears completely and with it the passband-like behavior. What is left is a gradual roll-off of the transmittance with frequency until the absorption dip at 3.84 THz is reached. For frequencies below the absorption dip, the S-polarization transmittance is very good, comparable to the transmittance of the bridged designs in the lower passband. The extinction ratio at 1 THz is 37.8 dB, slightly better than the designs with bridges.
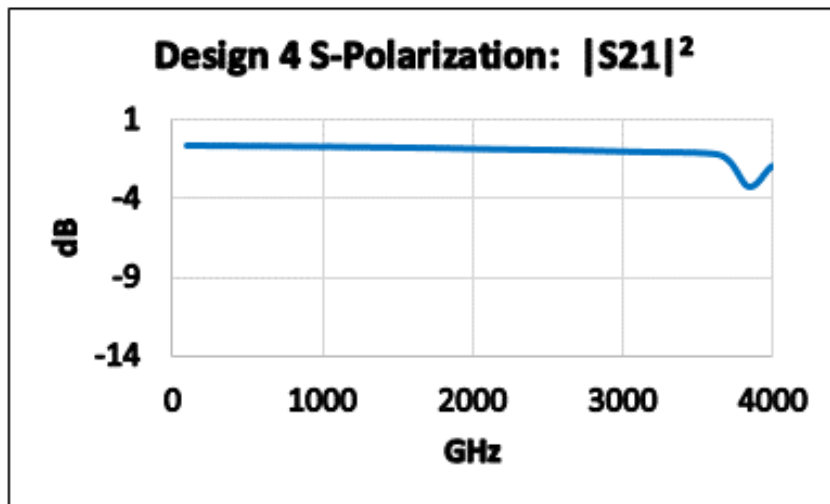
Fig 4-43: Calculated transmittance for s-polarization. THz wire-grid polarizer without bridges, Design 4.
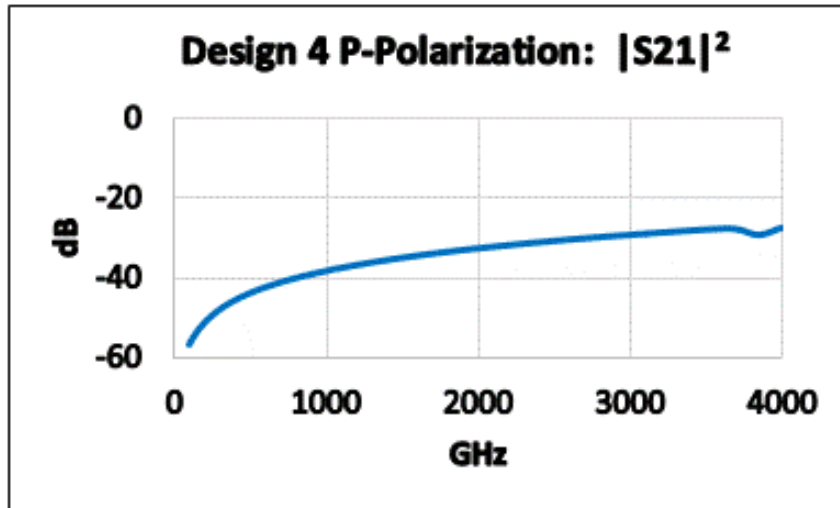
Fig 4-44: Calculated transmittance for p-polarization. THz wire-grid polarizer without bridges, Design 4.

Table 4-6 summarizes the calculated transmittance results for Designs 1-4, and reveals some interesting trends. Increasing the period and slot length in the x-direction causes a decrease in the notch center frequency, the notch depth, and the 3-dB bandwidth for the lower

Transmittance	Design 1	Design 2	Design 3	Design 4
3 dB Bandwidth (THz)	2.48	2.08	1.71	Not Applicable
Notch Frequency (THz)	2.76	2.28	1.88	Not Applicable
Notch Depth (dB)	13.7	6.9	5.6	Not Applicable
Extinction ratio at 1 THz (dB)	36.2	36.4	36.0	37.8
Notch Q Factor	102	10.2	6.7	Not Applicable

Table 4-6: Summary of calculated transmittance data for Designs 1-4.

passband. Further, the width of the notch broadens consistent with the decreasing quality factor. Yet, the extinction ratio at 1 THz changes very little with geometry.

In addition to the transmittance, the reflectance responses for these designs was also calculated. The results of these calculations for S-polarization are shown in Fig 4-45. In all three designs, there are two features that stand out. The first is a monotonic increase in reflectance with decreasing frequency below 1000 GHz. Second is a design-dependent peak. This peak decreases in magnitude and in center frequency with increasing structure period and slot length in the x-direction. Fig 4-46 shows the reflectance response when the bridges are removed from the design. Both reflectance features have disappeared, and what remains is a slight monotonic increase in reflectance with frequency.
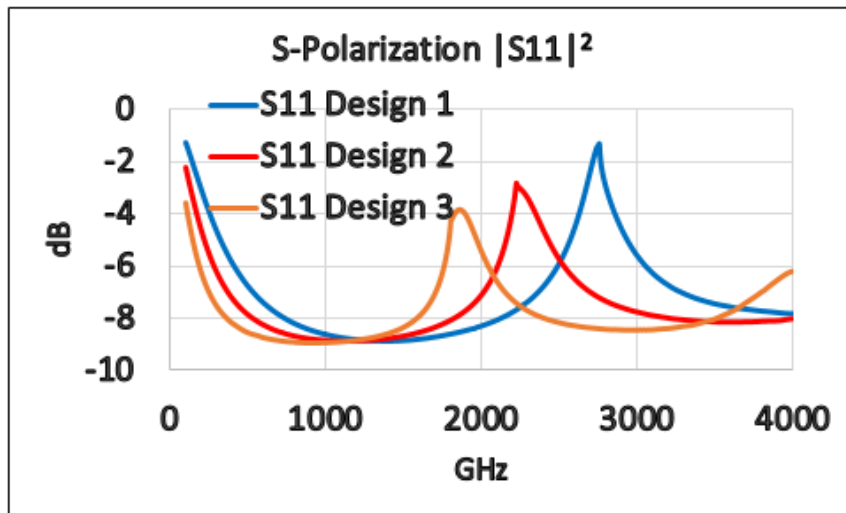
Fig 4-45: Calculated reflectance for s-polarization. THz wire-grid polarizers with bridges, Designs 1-3.

114
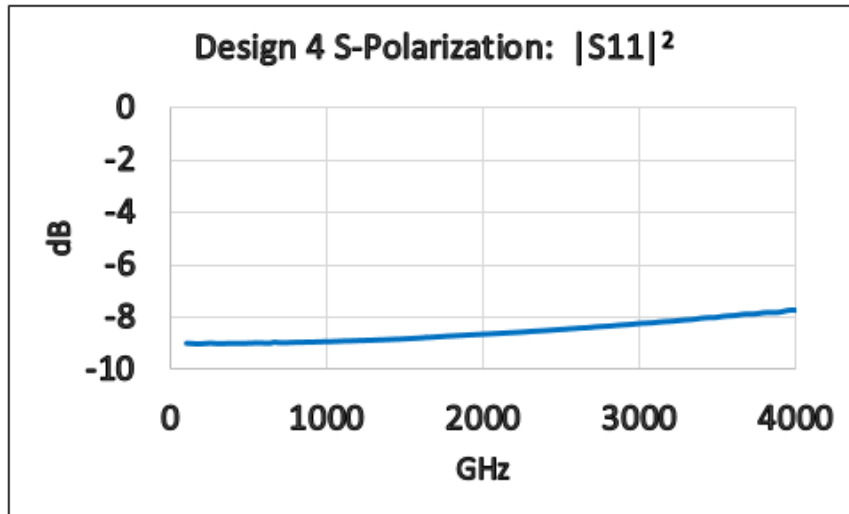
Fig 4-46: Calculated reflectance for s-polarization. THz wire-grid polarizer without bridges, Design 4.

Referring back to Designs 1-3, the peak reflectance frequencies almost coincide with the transmittance notch frequencies seen in Table 4-6. The reflectances for P-polarization are the same for each design iteration. Each shows a reflectance of approximately -0.01 dB at 100 GHz which decreases monotonically to approximately -0.07 dB at 4 THz. Table 4-7 summarizes the S-polarization reflectance results.

Reflectance	Design 1	Design 2	Design 3
Peak Frequency (THz)	2.76	2.23	1.86
Peak Magnitude (dB)	-1.3	-2.8	-3.8
Q Factor	10.4	5.7	4.5

Table 4-7: Summary of calculated reflectance data for Designs 1-3.

Because of their dependence on the period in the x-direction and their absence in wire-grid polarizers without bridges, the notch resonances beckoned further study. To explore them further, Design 5 was created and simulated wherein the slot length and x-period were increased to 185 μm and 187 μm, respectively. This is more than twice the minimum incident wavelength (λ = 71.4 μm) of the corresponding maximum frequency in the sweep. The calculated transmittance for Design 5 is shown in Fig 4-47 which now shows two notches. In addition, the calculated reflectance response for Design 5 is shown in Fig 4-48 which shows two peaks.
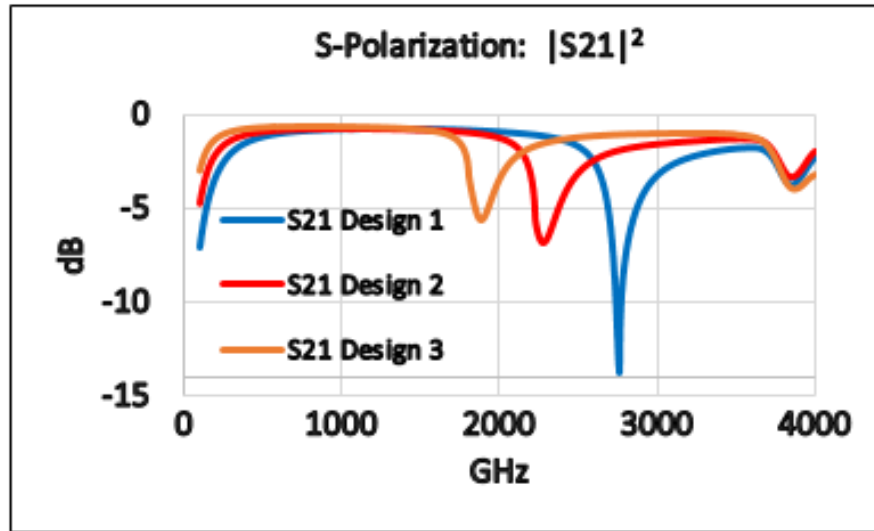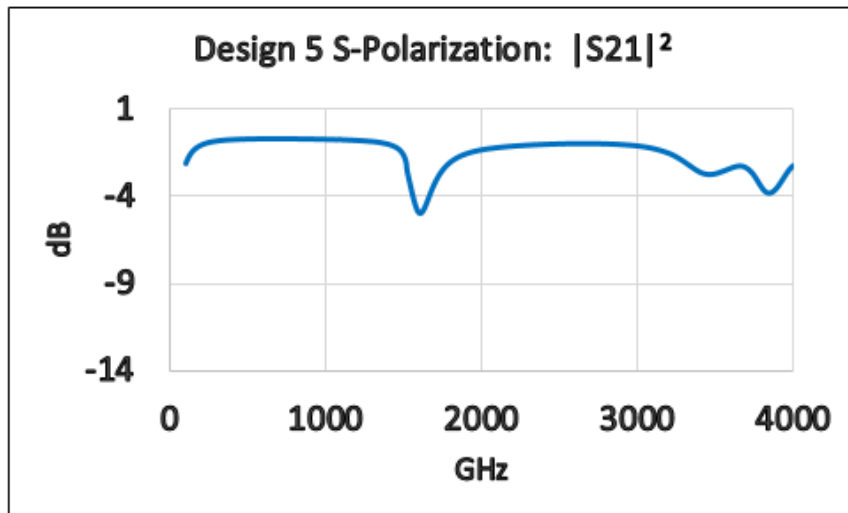

Fig 4-47: Calculated transmittance for s-polarization. THz wire-grid polarizer with bridges, Design 5.
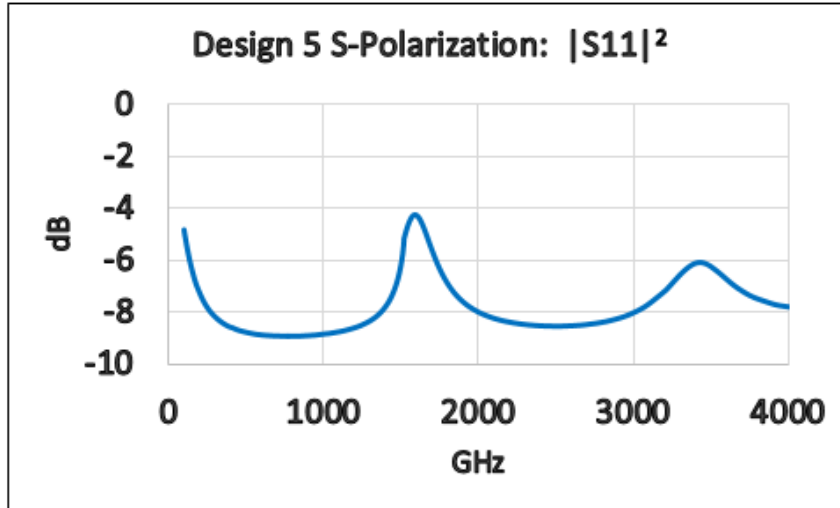
Fig 4-48: Calculated reflectance for s-polarization. THz wire-grid polarizer with bridges, Design 5.

Table 4-8 shows the values of the resonant wavelengths for the transmittance notches and the reflectance peaks, the grating periods for the designs in the x and y directions, and the ratios of the resonant wavelengths to the grating periods. Also listed are the ratios of the first resonant wavelengths to the second resonant wavelengths for the transmittance notches and reflectance peaks in Design 5.

As seen in the λ_{notch}/a_x column, none of the resonant transmittance notch wavelengths equals its corresponding grating period in the x direction. Further, as seen in the λ_{peak}/a_x column, none of the resonant reflectance peak wavelengths equals its corresponding grating period in the x direction. Although in both cases, the values are very close to being equal. For both transmittance notches and reflectance peaks, the ratios move closer to unity as the grating x- period gets larger. Fig 4-49 plots the resonant wavelength versus x direction grating period for Designs 1, 2, 3, and 5. The data points are fitted with a linear trend line approximation. The equations for the trend lines and their correlation coefficients are also given. Note that

117

	a_x (µm)	a_y (µm)	λ_{notch} (µm)	λ_{notch} / a_x	λ_{peak} (µm)	λ_{peak} / a_x
Design 1	102	16	108.8	1.067	108.8	1.067
Design 2	127	16	131.8	1.038	134.7	1.061
Design 3	157	16	159.3	1.015	161.2	1.027
Design 5	187	16	186.8	0.999	188.8	1.010
			86.6	0.463	87.5	0.468
	Design 5 order ratio:		2.157		2.158	

Table 4-8: Ratios of resonant frequencies to grating periods for Designs 1, 2, 3, and 5, and order ratios for Design 5. Parameters: a_x = x direction period, a_y = y direction period, λ_{notch} = transmittance notch resonant wavelength, λ_{peak} = reflectance peak resonant wavelength, order ratio = ratio of the second resonant wavelength to the first resonant wavelength for Design 5.

neither trend line slope is unity but the correlation coefficients are unity. Further, the y intercept values for both trend lines are non-zero.

These somewhat anomalous results can be explained by the fact that the periodicity of this structure has two degrees of freedom (x and y). Both the x and y periods (a_x and a_y) are components that determine the resonant frequencies. Therefore, a_x alone does not determine λ_{notch} or λ_{peak} but the combination of a_x and a_y. However, as the ratio of a_x/a_y increases, a_x starts to become the dominate factor in setting λ_{notch} and λ_{peak}. This is why the ratios move closer to unity as the grating x-period gets larger. Further, the absence or presence of a substrate and the type of substrate material also has a strong effect on the transmission spectrum. The resonances are red-shifted when a substrate is present. Therefore, the y-intercept of the trend lines are shifted above zero. The combination of these factors results in notch and peak frequencies that do not behave exactly as they would in a simple 1D grating.
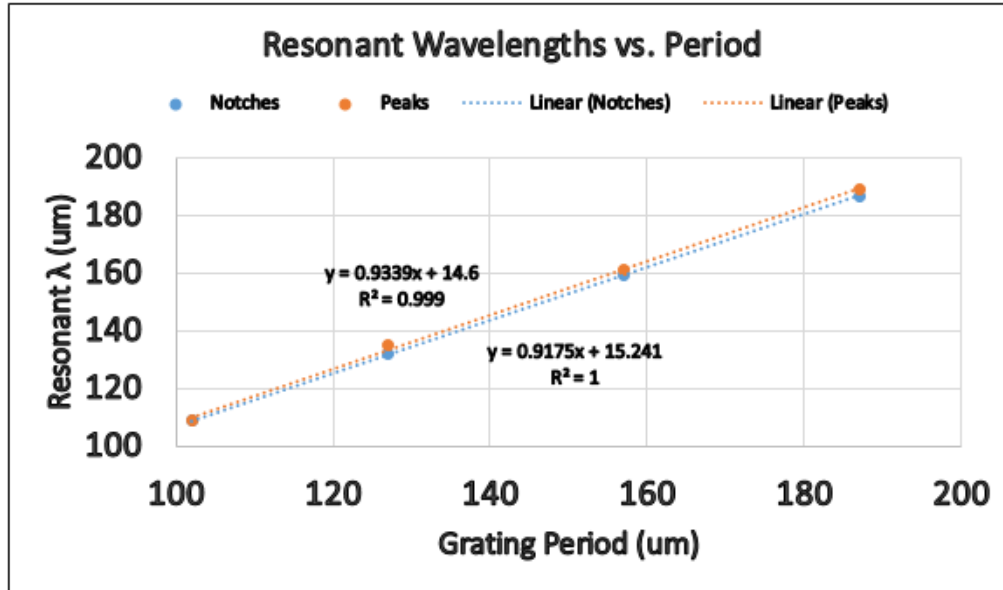
Fig 4-49: Resonant wavelengths for transmittance notches and reflectance peaks versus grating period in the x direction. Linear trend line curves have been fitted to the data. The equations for the trend lines and their correlation coefficients are given.

Next, a fill factor study was performed on this structure to investigate how the zero-order transmission response changed with changing fill factor. For this structure, changing the fill factor involves two degrees of freedom. First, the width of the slots can be increased or decreased in order to decrease or increase the fill factor. Second, the length of the bridges can be increased or decreased in order to increase or decrease the fill factor. In either case, the grating periods in the x and y direction are left constant. Design 1 was used as the baseline design for the fill factor study. Fig 4-50 shows the S-polarization transmittance through the polarizer at three different slot widths (4, 2 and 1 µm) with the bridge length fixed. As can be seen, decreasing the slot width (increasing the fill factor) increases the notch depth but at the cost of broadening the notch shape and therefore decreasing the 3dB bandwidth of the lower passband.

119
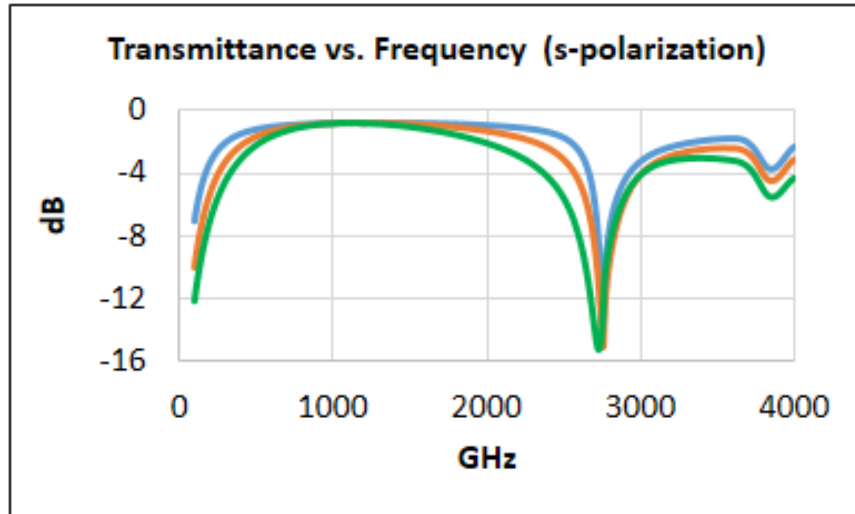
Fig 4-50: Fill factor study – varying slot width. Blue – slots 100 x 4 um. Orange – slots 100 x 2 um. Green – slots 100 x 1 um. Bridge length fixed at 2 um.

Fig 4-51 shows the S-polarization transmittance through the polarizer at four different bridge lengths (1, 2 5, and 20 μm) with the slot width fixed. As can be seen, increasing the bridge length (increasing the fill factor) decreases the notch depth and broadens the notch shape. In addition, there is a noticeable blue shift of the notch center frequency with increasing bridge length.

Fig 4-52 shows the P-polarization transmittance through the polarizer at same three slot widths and the same four bridge lengths. Fig 4-52 shows that the P-polarization transmittance is more effectively lowered by decreasing the slot width than by increasing the bridge length.
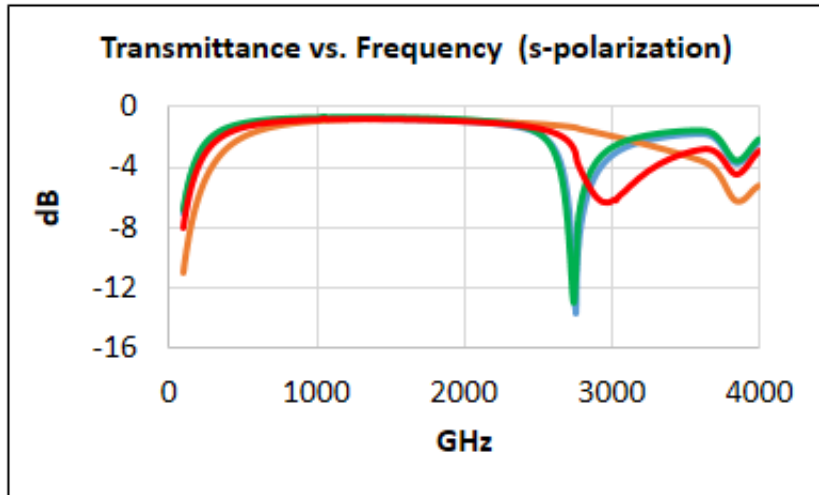
Fig 4-51: Fill factor study – varying bridge length. Green – bridge length 1 um. Blue – bridge length 2 um. Red – bridge length 5 um. Orange – bridge length 20 um. Slot width fixed at 4 um.
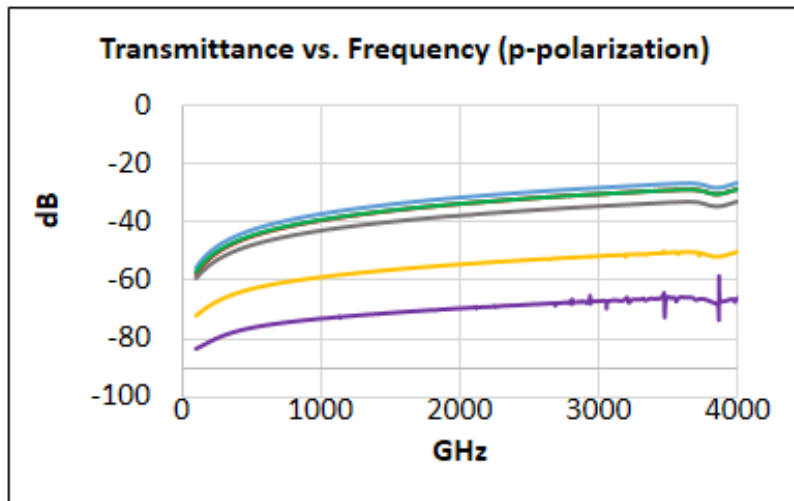
Fig 4-52: Fill factor study – bridge length fixed at 2 μm. Slot width varied. Blue – slots 100 x 4 um. Yellow – slots 100 x 2 um. Purple – slots 100 x 1 um. Slot width fixed at 4 μm. Bridge length varied. Blue – bridge length 2 um. Green – bridge length 1 um. Grey – bridge length 5 um. Red – bridge length 20 um.

Fig 4-53 show the extinction ratios for all of these fill factor changes. Not surprising, the most significant improvement to the extinction ratio can be achieved by decreasing the slot width. It is important to remember that decreasing the slot width also broadens the notch and therefore decreases the 3 dB bandwidth of the passband. Therefore, there is a limit to how far one can go in optimizing this parameter. For this design, Design 1, a slot width of 2 to 4 µm seems to yield a good combination of notch depth and high quality factor.
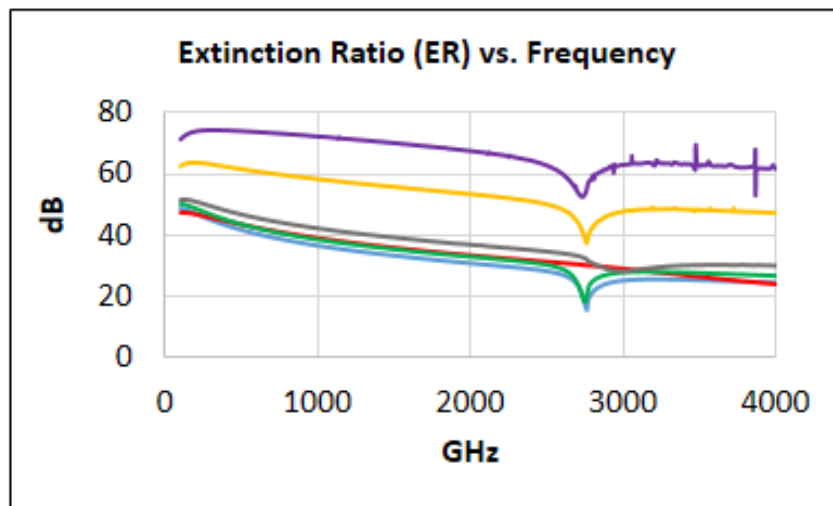
Fig 4-53: Fill factor study – bridge length fixed at 2 µm. Slot width varied. Blue – slots 100 x 4 um. Yellow – slots 100 x 2 um. Purple – slots 100 x 1 um. Slot width fixed at 4 µm. Bridge length varied. Blue – bridge length 2 um. Green – bridge length 1 um. Grey – bridge length 5 um. Red – bridge length 20 um.

To close this section, the response of the THz wire-grid polarizer with bridges was studied while varying the offset between the positions of the bridges in adjacent slots. Referring back to Fig 4-40, the design has bridges connecting adjacent slots at positions offset from one another in the x-direction by $a_x/2$, where a_x is the period in the x-direction. This offset is now varied from $a_x/2$ to $a_x/4$ and then to zero. At zero offset, the device essentially becomes an inductive mesh grid [89]. All the other dimensions were held constant so that the

original fill factor of 75% was maintained. The S-polarized transmittance is shown in Fig 4-54. As be seen, the notch frequency is red-shifted, the notch depth diminishes, and the low frequency roll-off increases as the offset decreases. When the offset goes to zero, the notch disappears, the low frequency roll-off becomes much worse, and a slight cusp appears at approximately $f = 1400$ GHz.

Fig 4-55 shows the P-polarization transmittance as the offset is varied. Here, we see that there is negligible effect due to decreasing the offset from $a_x/2$ to $a_x/4$ to zero. The response is approximately the same of all three offsets. Fig 4-56 shows the effect of varying the offset on the polarizer extinction ratio. These curves essentially mirror the behavior for S-polarized transmittance. The zero offset polarizer tends to have an extinction ratio that is greater than or equal to the other polarizers for frequencies above approximately $f = 500$ GHz.
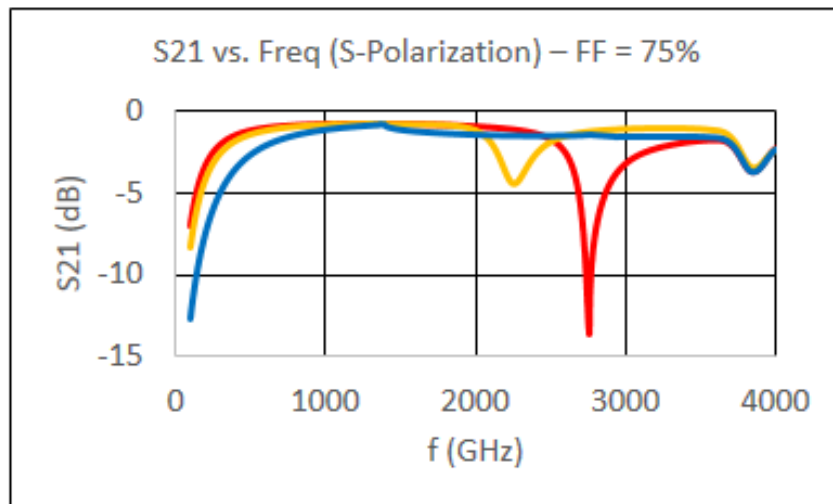
Fig 4-54: Offset study - varying bridge offset. S-polarization transmittance for FF = 75%, red - offset = $a_x/2$, yellow – offset = $a_x/4$, blue – no offset.
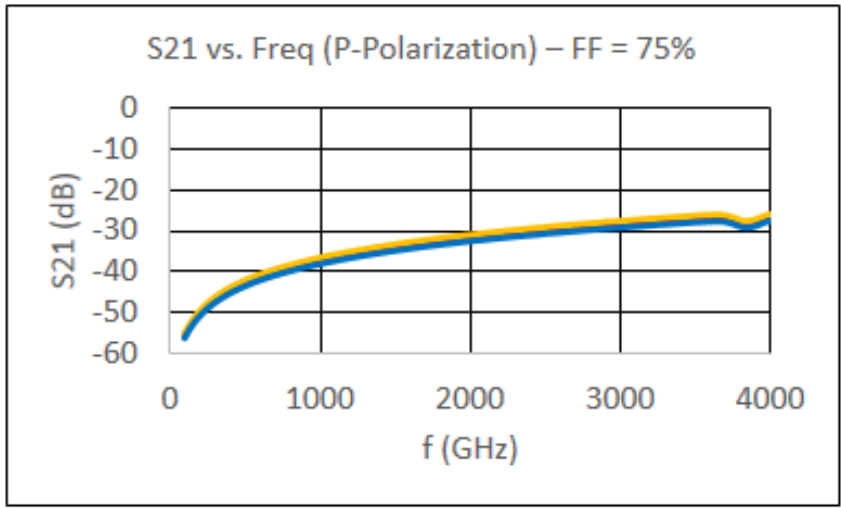
Fig 4-55: Offset study - varying bridge offset. P-polarization transmittance for FF = 75%, red - offset = $a_x/2$, yellow – offset = $a_x/4$, blue – no offset.
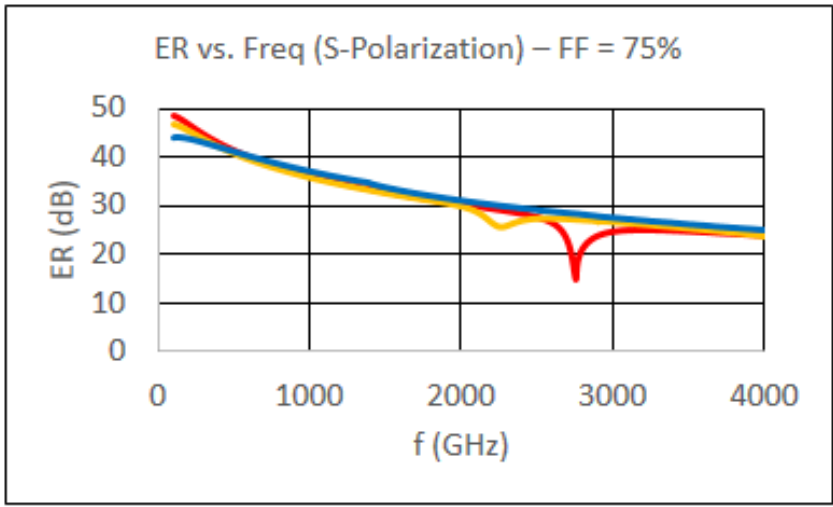
Fig 4-56: Offset study - varying bridge offset. Extinction ratio, FF = 75%, red - offset = $a_x/2$, yellow – offset = $a_x/4$, blue – no offset.

Finally, the bridge offset variation study was recalculated for a fill factor of 91%. The higher fill factor was achieved by decreasing the slot widths from 4 μm to 1.5 μm. The responses of the 91% fill factor to the 75% fill factor are compared. The S-polarization transmittances for both fill factors while varying offsets are shown in Fig 4-57 below. For both fill factors, decreasing the offset has the same effects as before: the notch frequency is red-shifted, the notch depth diminishes, and the low frequency roll-off increases as the offset decreases. We see that there are some subtle differences due to the fill factor changes. The notch frequency blue-shifts slightly with the higher fill factor for the offsets of $a_x/2$ and $a_x/4$. This behavior was seen earlier (see Fig 4-50), and is confirmed here.

Fig 4-58 shows the P-polarization transmittances for both fill factors while varying offsets. Here, there is a striking difference between the two fill factors groups. As can be seen, the group with the higher fill factor has a much lower transmittance (higher insertion loss) for all offset values. This difference in P-polarization transmittance is responsible for the significant difference in the extinction ratios as seen in Fig 4-59. The higher fill factor group has much better extinction ratios than the lower fill factor group at all offsets. This confirms the results seen in Fig 4-53 (Section 4.4) as well as the general findings for the basic wire-grid polarizers studied in Section 4.2 and in Refs [83] and [84].

In summary, the THz wire-grid polarizer with bridges functions as a wide-band polarizer across several THz of bandwidth. An interesting notch feature is seen which gives the device a weak band-pass filter character. The notch feature is controlled by changing the slit length and period, the device fill factor, and the bridge offset. Overall the device shows excellent transmittance and extinction ratios over the range of calculated frequencies. The bridges have an important function as they allow the device to act as a transparent electrode

while forcing DC currents to take an indirect path across the structure due the offset in bridge positions in adjacent slots.
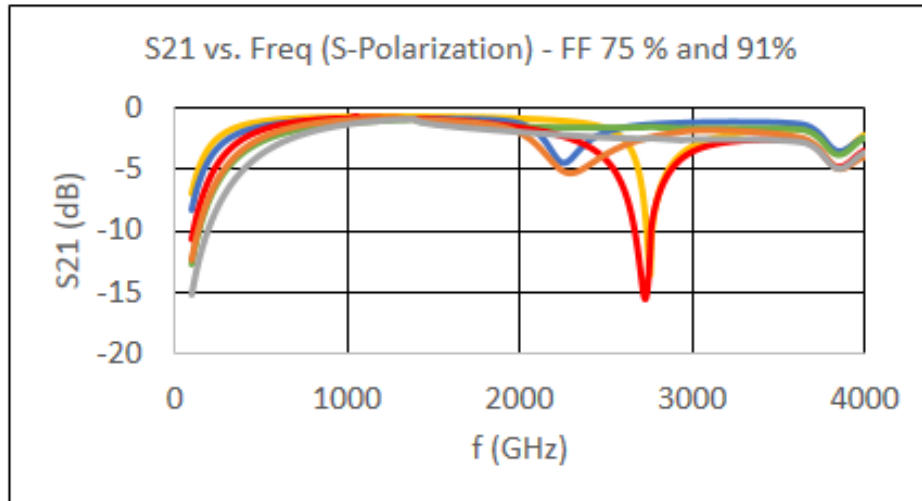
Fig 4-57: Offset study - varying bridge offset and FF. S-polarization transmittance for FF = 75%, yellow - offset = $a_x/2$, blue – offset = $a_x/4$, green – no offset. S-polarization transmittance for FF = 91%, red - offset = $a_x/2$, orange – offset = $a_x/4$, grey – no offset.
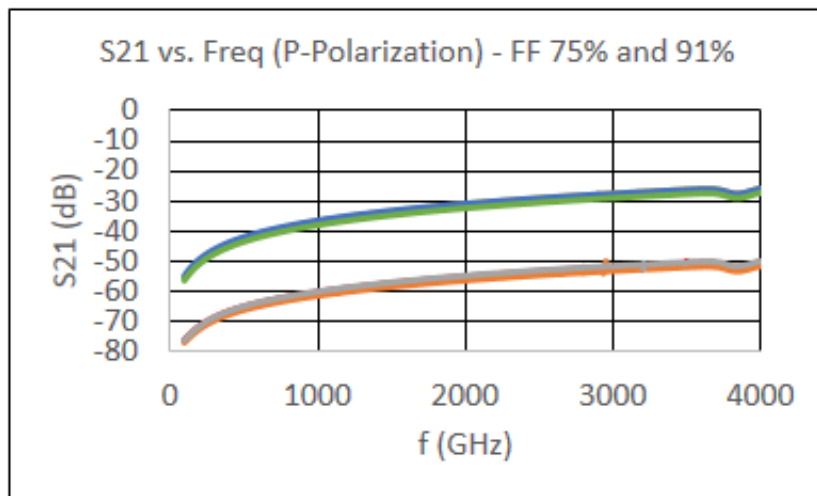
Fig 4-58: Offset study - varying bridge offset. P-polarization transmittance for FF = 75%, yellow - offset = $a_x/2$, blue – offset = $a_x/4$, green – no offset. P-polarization transmittance for FF = 91%, red - offset = $a_x/2$, orange – offset = $a_x/4$, purple – no offset.
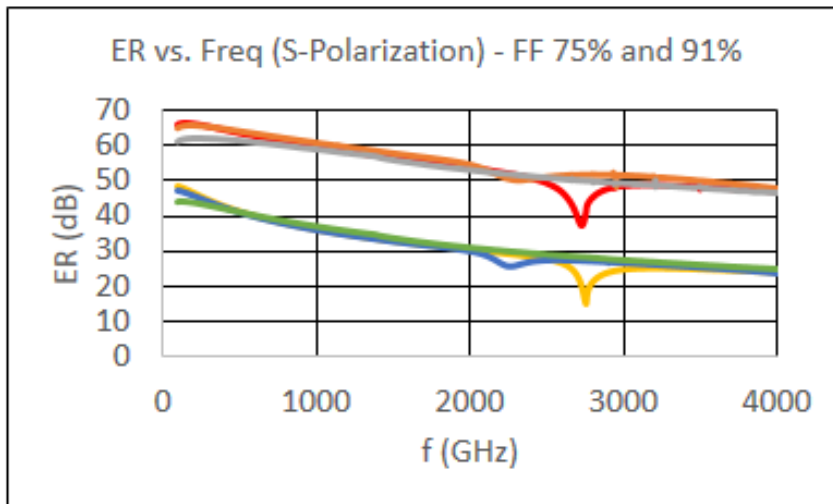
Fig 4-59: Offset study - varying bridge offset. Extinction ratio, FF = 75%, yellow - offset = $a_x/2$, blue – offset = $a_x/4$, green – no offset. Extinction ratio, FF = 91%, red - offset = $a_x/2$, orange – offset = $a_x/4$, purple – no offset.

5. Full Wave Simulations of LWIR Plasmonic Wire Gratings

5.1. Enhancing LWIR Sensor Coupling using SPPs

The previous chapter of this dissertation described how THz radiation incident on subwavelength periodic 1D metallic wire-grid structures can produce novel and interesting electromagnetic phenomena in the zero-order transmission spectra of these structures. The electromagnetic phenomena resulted in EOT. Because of the long wavelength of the incident radiation relative to the plasma wavelength of the metals, the cause for EOT was identified as structured surface plasmons (SSPs) also known as "spoof" plasmons. In this chapter, LWIR radiation incident on Plasmonic Wire Gratings (PWGs) will be discussed. Here, the geometries of the PWGs will be approximately equal to the wavelength of the radiation. In addition, since the radiation is LWIR, the wavelengths will be much closer to the plasma wavelength of the metals. EOT will still be observed. Nevertheless, because of these two factors, the causes for EOT under these conditions will now be surface plasmons (SPPs) and waveguide modes.

Shishodia and Perera modeled PWGs mounted directly on top of the active regions of a class of mid-IR photon detectors known as Heterojunction Interfacial Workfunction Internal Photoemission (HEIWIP) photodetectors [31]. HEIWIP photodetectors operate in the mid-IR having a peak responsivity at approximately $\lambda = 10$ μm, the center of the LWIR region. Shishodia and Perera's calculations showed that the generation of SPPs in PWGs greatly strengthen the coupling between the incident radiation and the active regions of the HEIWIP detector, thus greatly enhancing device performance. Shishodia and Perera predicted resonant

absorption peaks that span the LWIR region. They predicted a blue shift in the resonant peaks with increasing PWG thickness and a red shift with increasing PWG period. Finally, they predicted that the addition of a PWG to a HEIWIP photodetector will result in a substantial increase in the absorption of the incident radiation by the detector. SPP enhanced optical absorption is considered to be of great importance for optoelectronic devices such as photodetectors, solar cells, LEDs, and semiconductor lasers.

The initial goals of this study were to determine if EOT could be seen in FEM simulations of LWIR radiation incident on PWGs, to optimize the PWG design for maximum zero-order transmission, and to fabricate and test an optimized design prototype. Lamentably, no optimized design was found. Therefore, no prototype was fabricated. Nevertheless, a significant theoretical study using both HFSS and COMSOL FEM simulations was performed that yielded some interesting results. Those simulations and their results will be the subject of the next sections.

5.2. LWIR PWG Simulations in HFSS

The initial simulations in the LWIR PWG study used HFSS. The PWG consisted of parallel gold wires separated by air gaps with a period of $d = 10$ μm. As a starting point, this device was modelled as a free space structure, no substrate underneath. First, the zero-order transmission of the structure was studied while varying wire thickness h from 0.1 μm to 2.0 μm with a wire width fixed at 5.0 μm (50% fill factor). Next, the zero-order transmission was then studied while varying wire width from $a = 2.0$ to 8.0 μm – varying fill factor from 20% to 80 %, with a wire thickness fixed at 0.2 μm. A 3D unit cell of the LWIR PWG is shown in Fig 5-1.
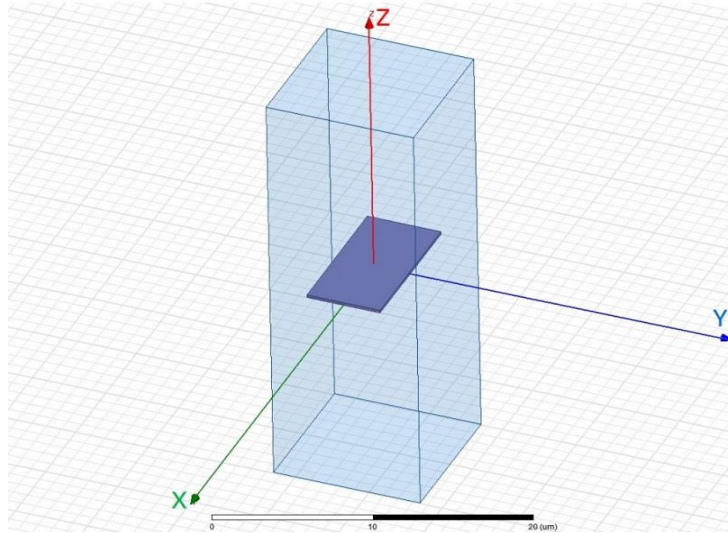
Fig 5-1: LWIR PWG unit cell used in HFSS simulations. Cell dimensions are 10 x 10 x 60 μm.

Periodic boundary conditions and Floquet ports were used in the simulation. The incident radiation was normal to the plane of the structure and polarized perpendicular to the direction of the wire (TM or S-polarization). The wavelength of the incident radiation was swept over a range of 20 THz to 60 THz ($\lambda = 15$ μm to 5 μm) in steps of 500 GHz. The HFSS library gold was used to model the wire.

The transmission versus wavelength plots for various wire thicknesses is shown in Fig 5-2. There is a strong transmission peak, $T \cong 0.90$, located at $\lambda = 10$ μm. The peak is strongest for h = 0.1 μm and decreases in strength with increasing wire thickness.

130
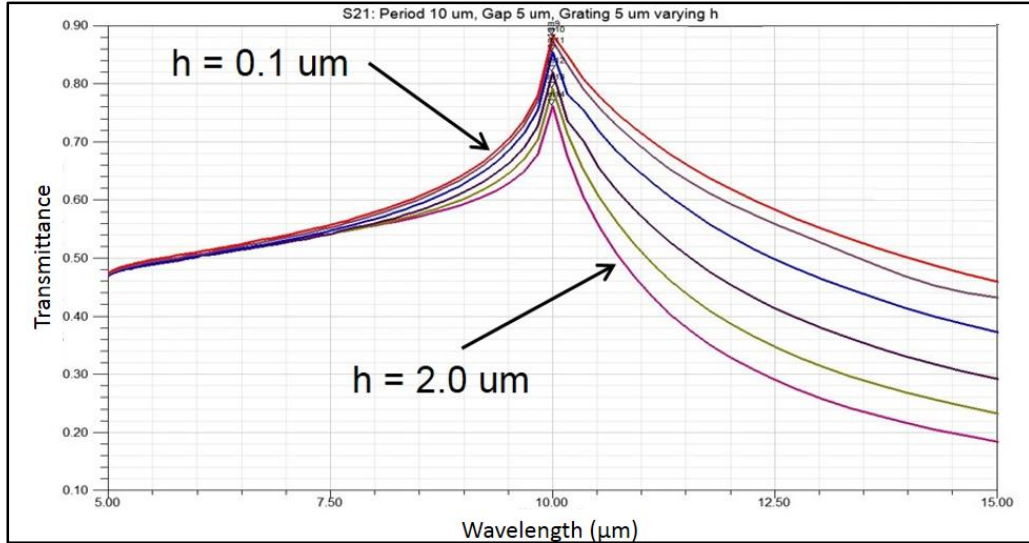
Fig 5-2: Zero-order S-polarization transmission through a LWIR PWG from 20 THz to 60 THz (15 μm to 5 μm wavelength). Grating wire thickness is varied, h = [0.1, 0.2, 0.5, 1.0, 1.5, 2.0] μm. Wire width is a = 5 μm (50% fill factor), and the period is fixed at d = 10 um.

The transmission versus wavelength plots for various wire widths (fill factors) is shown in Fig 5-3. Here, there is a strong transmission peak at λ = 10 μm as well. The peak is strongest for a = 2.0 μm (20% fill factor) and decreases with increasing wire width (increasing fill factor). What is most striking is that the behavior of the PWG in the LWIR region is not at all like the behavior of wire-grid polarizers in the THz region. First and foremost, the transmission peaks seen in the LWIR were not seen in the THz region for these simple 1D structures. Secondly, the transmission decreases with increasing wire width (fill factor) in the LWIR region while it remains roughly constant in the THz region (compare results in Fig 5-3 with results in Fig 4-10a).

Transmission occurs in the LWIR PWG for $h < \lambda/2$. This indicates that the mechanism for this transmission is not a TEM waveguide mode (see Table 2-1). The peaks occur at $\lambda \cong d$

and decreases in strength for increasing wire thickness h. The tentative conclusion is that SPPs are causing these transmission peaks in the LWIR region as opposed to SSPs in the THz region.
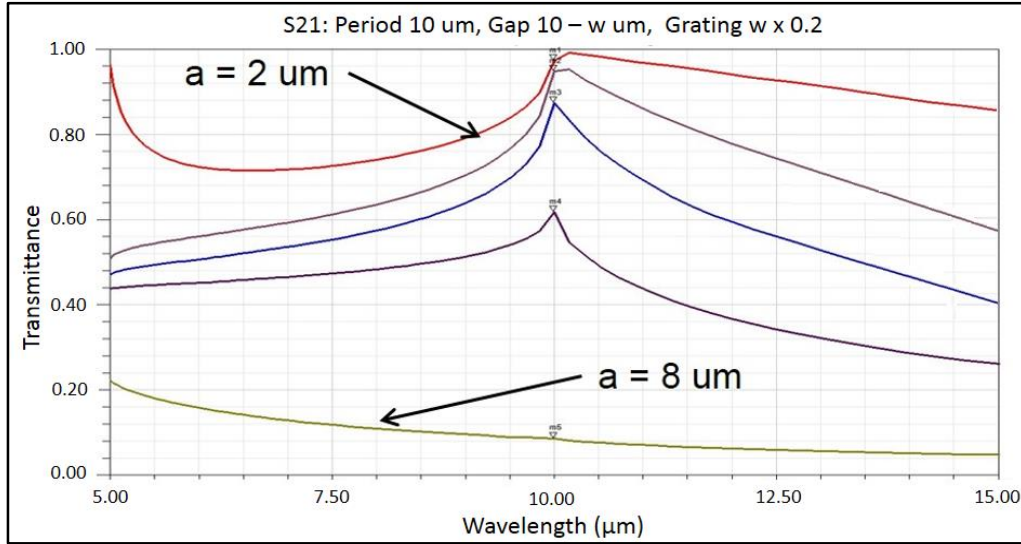
Fig 5-3: Zero-order transmission through a LWIR PWG from 20 THz to 60 THz (15 μm to 5 μm wavelength). Grating wire width is varied, a = [2.0, 4.0, 5.0, 6.0, 8.0] μm (20%, 40%, 50%, 60%, and 80% fill factors). The period is fixed at d = 10 um, and the wire thickness is h = 0.2 μm.

Nevertheless, several issues occurred during the HFSS simulations that contradict this conclusion. First, the shapes of the resonances in Fig 5-2 and Fig 5-3 are broad (low Q-factor), unlike SPP resonance shapes. Second, the LWIR PWG structures have dimensions of the same order of magnitude as the wavelengths of the incident radiation. Because of this, the number of modes that HFSS was required to calculate in each simulation to account for all EM energy rose significantly. HFSS struggled with these calculations. Attempts to incorporate substrates or to use a Drude material model for the gold exacerbated the problem. Therefore, the free space structure using the HFSS library model for the gold was the only configuration simulated. As stated earlier, HFSS material library conductors are both dispersionless, have real valued conductivities, and have real valued dielectric constants equal to unity. SPPs

require the interface of a conductor having a complex dielectric constant (negative real part and positive imaginary part) with a dielectric having a dielectric constant that is both real and positive. These conditions were not met in these HFSS simulations. The HFSS library gold acted more like a perfect electrical conductor (PEC) than a real metal. It is more likely that the mechanism responsible for the high transmission seen in the LWIR PWG is constructive and destructive interference of the secondary radiation originating from the dipoles that form at each gap, indicative of SSPs.

5.3. LWIR PWG Simulations in COMSOL

In the next phase of the study, COMSOL Multiphysics was used to provide contrast to the HFSS analysis. As part of the COMSOL model development, the zero-order transmission studies of Garcia-Vidal and Martin-Moreno (GV-MM) [40] on mid-IR PWGs were repeated. The results were compared against those of GV-MM to verify the validity of the COMSOL model and modeling process. This was done as the author was then new to COMSOL Multiphysics and therefore wanted a "sanity check" of the modeling process against a published result.

In their study, GV-MM used a Matrix Transfer Method and a quasi-analytical mode expansion method to perform their calculations. A schematic of the PWG used by GV-MM is shown in Fig 5-4 (a). The period of the structure is given by d =1.75 μm. The air gap between each wire element is given by a = 0.3 μm (a is now the gap width). The wire thickness is given by h. TM polarization is used in all of these studies as this is the only polarization that will excite SPPs [40]. For their transmission studies, GV-MM assumed that the wires were PECs
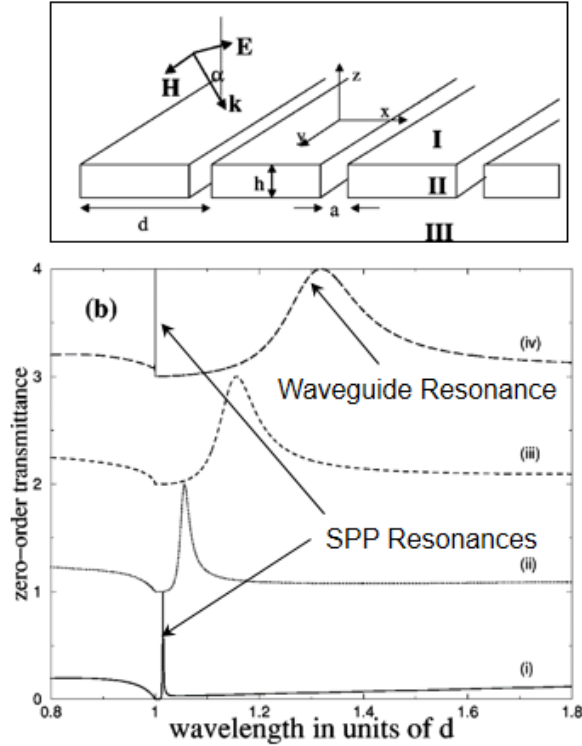
Fig 5-4: (a) Plasmonic wire grating geometry with d = 1.75 μm, a = 0.3 μm. (b) Zero-order transmission through the PWB with h = [0.2, 0.4, 0.6, 0.8] μm bottom to top. TM polarization only. From GV-MM [40].

and that the PWG was free-standing (no substrate). The zero-order transmission spectra as calculated by GV-MM is shown in Fig 5-4 (b) for wavelengths of 0.8d to 1.8d ($\lambda = 1.4$ μm to $\lambda = 3.15$ μm) and wire thicknesses of h = [0.2, 0.4, 0.6, 0.8] μm from bottom to top. Two types of resonances are seen, SPP resonances and TEM parallel plate waveguide resonances. The SPP resonances occur at $\lambda \gtrsim d$ and are reminiscent of Fano resonances. Fano resonances are spectral sharp (high Q), asymmetric (non-Lorentzian in shape) resonances that arise from the constructive and destructive interference of a narrow discrete resonance with a broad spectral line [90].   Note, the transmittance of these resonances is unity, indicating no losses in the metal.

134

An SPP resonance occurs at a thickness h = 0.2 μm < λ/2. As h increases, the resonant wavelength is red-shifted and its shape broadens. These changes continue until h = 0.8 μm, where a second high Q-factor resonance appears again at $\lambda \approx d$. At h = 0.8 μm, there are two transmission resonances, an SPP resonance at $\lambda \approx d$ and a waveguide resonance at $\lambda \cong 1.3d$.

A 2-D simulation was created in COMSOL to confirm these results. The use of a 2D model is justified as there is translational invariance along the axes of the wire elements which constitute the PWG. The use of a 2D model simplifies the computations relative to a 3D model. The unit cell used in the COMSOL simulation is shown in Fig 5-5.
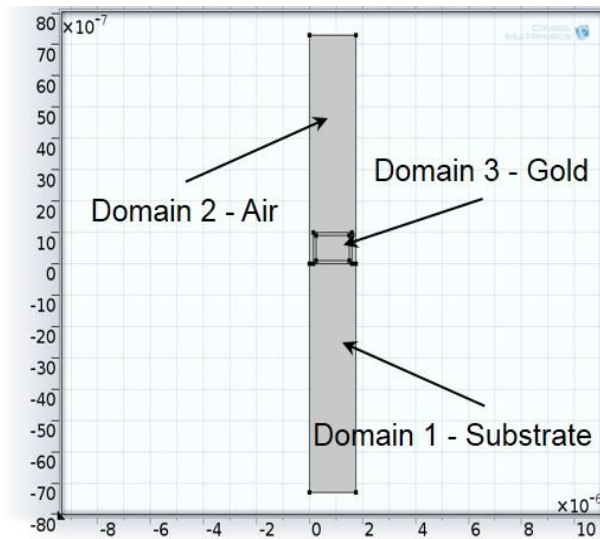
Fig 5-5: COMSOL 2-D unit cell model for a PWG with geometry given by d = 1.75 μm, a = 0.3 μm (w = 1.45 μm), h will vary.

The model was defined with three domains. Domain 1 – substrate, the bottom domain, was defined for use as a dielectric substrate but is kept as air initially to match the GV-MM configuration. Domain 2 – air, is the top domain. The incident radiation approaches the structure from the top. Domain 3 – gold (Au) is a cross-section of a single wire element in the center of the geometry. Au was used since no method was found to incorporate a PEC into a

domain material. COMSOL only allows PECs for boundaries. Rather than use the COMSOL

material library, a gold material model was created using measured optical data published by

Ordal [45]. Therefore, the model was lossy and dispersive and incorporated any far-wing

effects due to interband transitions (see Fig 4-2 and accompanying text in Section 4.1). The

incident radiation was normal to the top of the PWG and TM polarized to match the GV-MM

incident radiation. Periodic ports and boundary conditions were applied. The zero-order

transmission response calculated by COMSOL is shown in Fig 5-6.
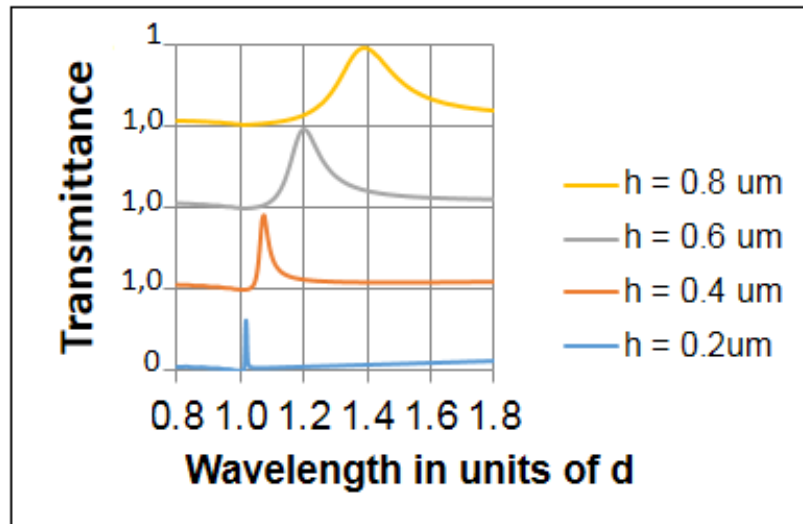
Fig 5-6: COMSOL calculation results for the zero-order transmission through the PWG
with h = [0.2, 0.4, 0.6, 0.8] µm. TM polarization only. Compare with Fig 5-4(b).
Ordinate ranges are from 0 to 1 for each curve.

The responses calculated by COMSOL match up well to those calculated by GV-MM

for all h < 0.8 µm except that the SPP resonance at $\lambda \gtrsim d$ has a much smaller magnitude in the

COMSOL result. This can be explained by the fact that the metal in the COMSOL simulation

had a complex permittivity which allowed it to absorb some of the EM energy from the incident

radiation while GV-MM used a PEC (no absorption loss). At h = 0.8 µm, the waveguide

resonance calculated by COMSOL is the same as that calculated by GV-MM. The SPP resonance at $\lambda \gtrsim d$ is missing in the COMSOL results. The explanation is the same as that explaining the smaller SPP resonance magnitude at h = 0.2 μm. The COMSOL simulation used an absorbing metal for the wire material instead of a PEC. Therefore, because of the extremely high Q-factor response of this resonance, as seen in Fig 5-4 (b), and because its energy is attenuated by the lossy Au in the COMSOL model, this resonance is simply not showing up in the COMSOL plot due to inadequate resolution. So, two further simulations were done with COMSOL to study the zero-order transmission at h = [1.0, 1.2, 1.4, 1.6] μm and h = [2.0, 3.0] μm. The combined COMSOL results for these thickness along with the corresponding GV-MM results are shown in Fig 5-7.
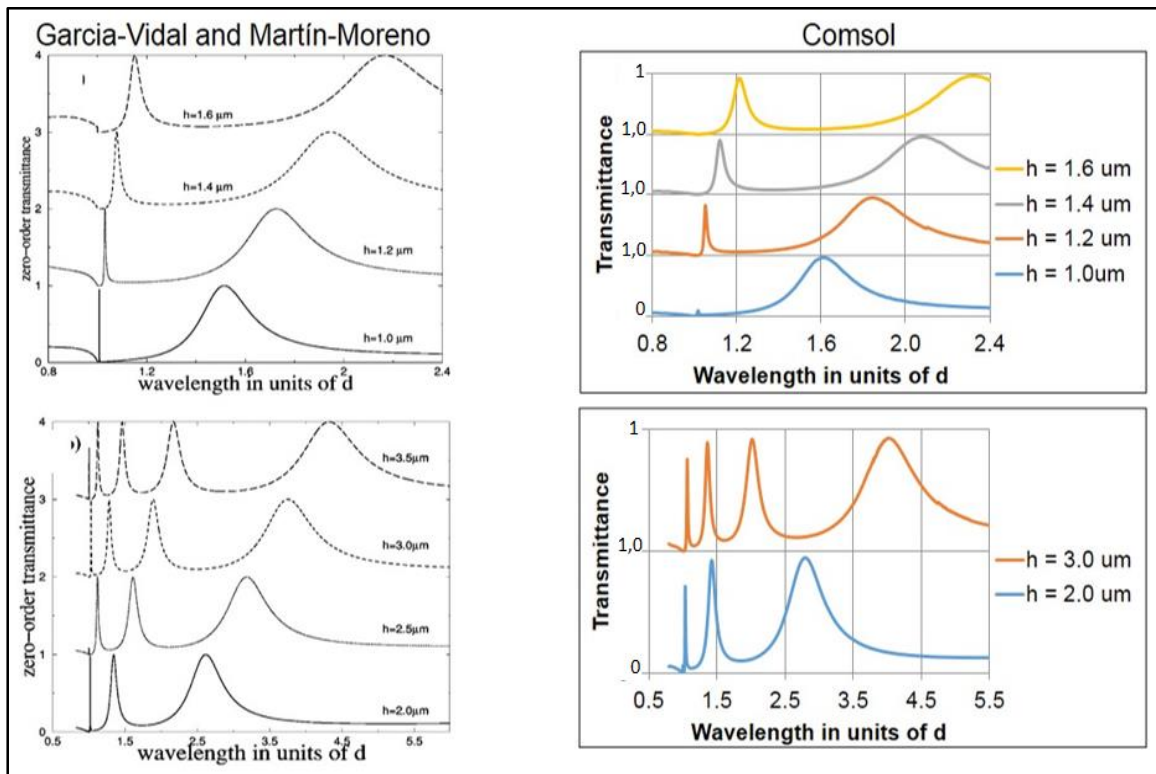
Fig 5-7: Calculated zero-order transmission, GV-MM [40] on the left and COMSOL on the right for various wire thicknesses. GV-MM thickness are (top left) h = [1.0, 1.2, 1.4, 1.6] μm and (bottom left) h = [2.0, 2.5, 3.0, 3.5] μm. Ordinate ranges are from 0 to 1 for each curve.

137

As can be, the COMSOL simulation reproduce the GV-MM results very well. Note the very small SPP resonant response for h = 1.0 μm calculated by COMSOL. This again is due to the use of the lossy Au in the COMSOL simulation.

It was stated earlier that in both the GV-MM and COMSOL, two types of resonances occur, SPP and waveguide resonances. To confirm this, the electromagnetic behavior in and around the PWGs was studied. Fig 5-8 shows GV-MM's plot of the Poynting vector ($\vec{S} = \vec{E} \times \vec{H}$) for an SPP resonance with d = 1.75 μm, a = 0.3 μm, h = 0.4 μm, and λ = 1.84 μm. Note the strong modes excited at the top and bottom horizontal surfaces as well as in the air gap. This field structure is characteristic of SPPs.

Field calculations were also done in COMSOL. Fig 5-9 shows the E-field for the SPP resonance. Here d = 1.75 μm, a = 0.3 μm, h = 2.0 μm, and λ = 1.65 μm. Radiation is incident normally from the top. This resonance can be seen in Fig 5-7 (bottom right, blue curve). Going back to Fig 5-9, note the strong modes excited at the top and bottom horizontal surfaces as well as in the air gap. This field structure is essentially the same as that calculated by GV-MM.

Fig 5-10 shows a plot of the Poynting vector ($\vec{S} = \vec{E} \times \vec{H}$) for a waveguide resonance as calculated by GV-MM. Here we have d = 1.75 μm, a = 0.3 μm, h = 1.2 μm, and λ = 3.0 μm. Radiation is normally incident from the top. Note how the structure acts somewhat like funnel, collecting all the EM energy incident on the top surface and squeezing it into the air gaps.

Fig 5-11 shows the COMSOL calculated E-field for the waveguide resonance. Here we have d = 1.75 μm, a = 0.3 μm, h = 2.0 μm, and λ = 1.65 μm. Radiation is normally incident from the top. This resonance can be seen in Fig 5-7 (bottom right, blue curve). Going back to Fig 5-11, we see the same basic field structure as calculated by GV-MM in Fig 5-10.
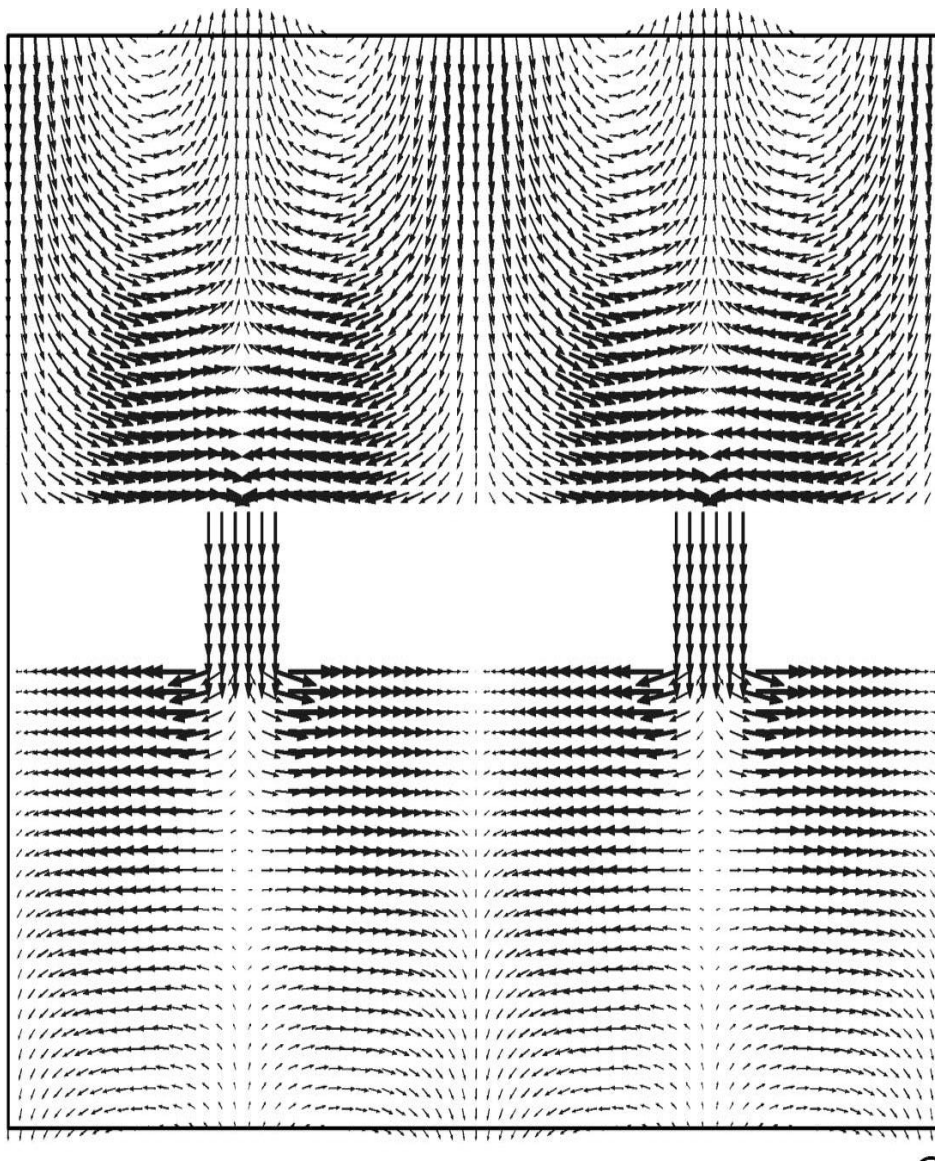
Fig 5-8: Calculated Poynting vector $(\vec{S} = \vec{E} \times \overrightarrow{H})$ showing an SPP resonances. From GV-MM [40]. Here d = 1.75 μm, a = 0.3 μm, h = 0.4 μm, and λ = 1.84 μm. Radiation incident from the top.
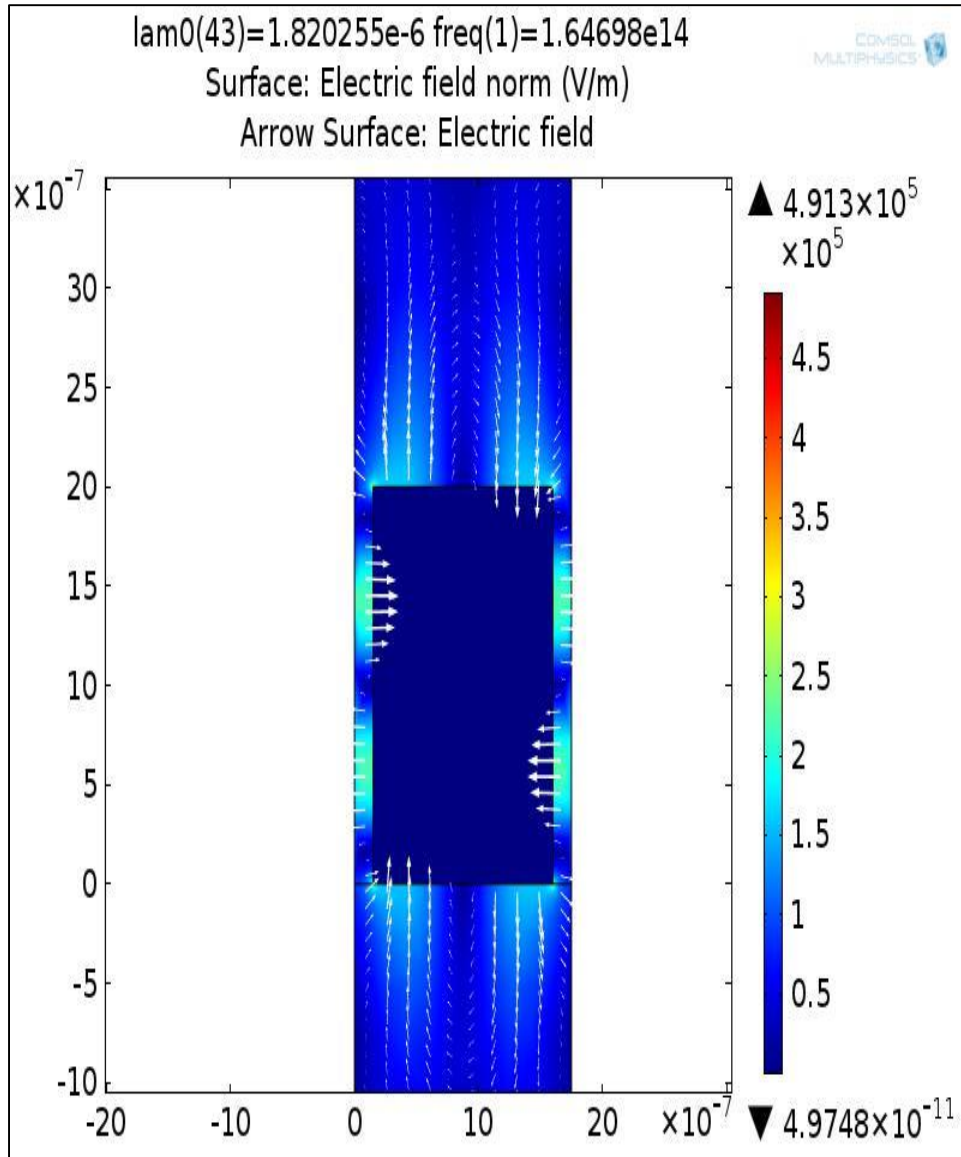
Fig 5-9: Calculated E-Field vector showing SPP resonances from COMSOL. Here d = 1.75 μm, a = 0.3 μm, h = 2.0 μm, and λ = 1.65 μm. Radiation is incident from the top.
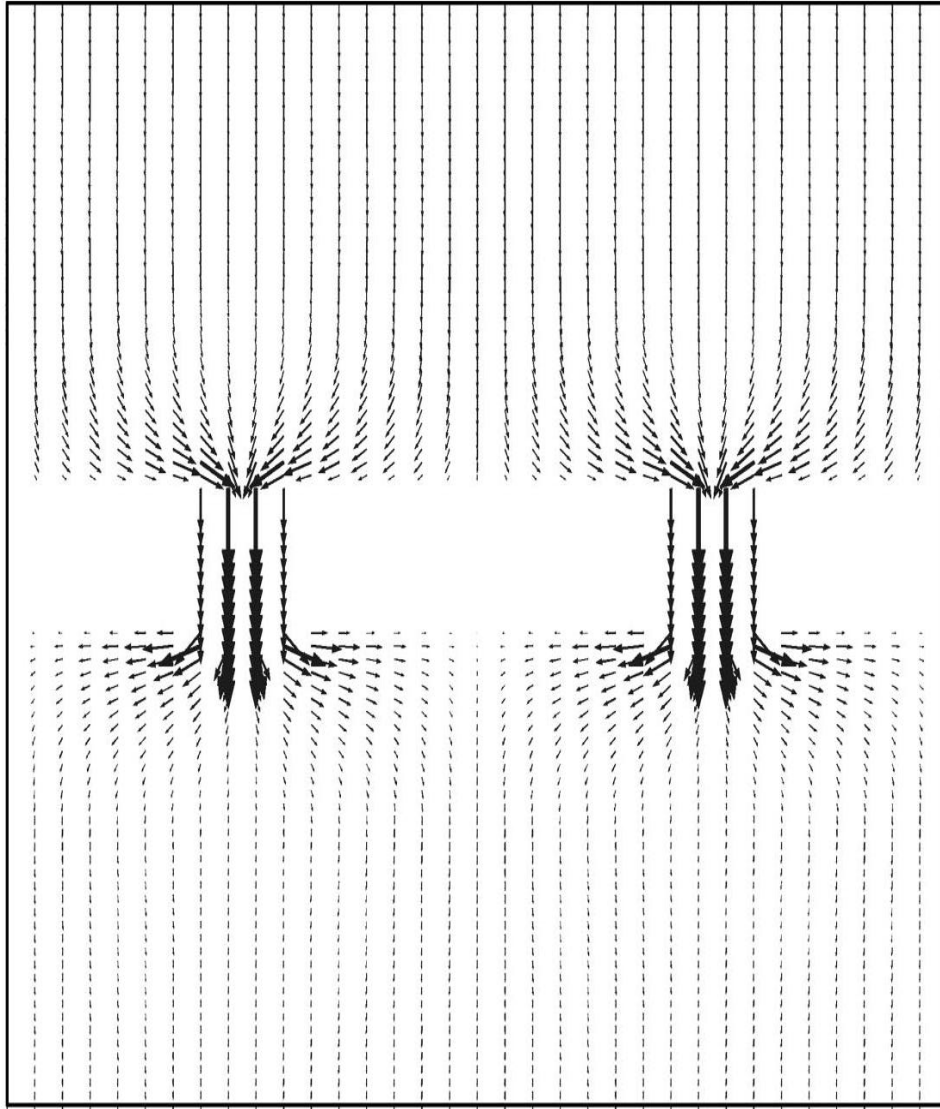
Fig 5-10: Calculated Poynting vector ($\vec{S} = \vec{E} \times \overrightarrow{H}$) showing cavity resonances. From GV-MM [40]. Here d = 1.75 µm, a = 0.3 µm, h = 1.2 µm, and λ = 3.0 µm. Radiation incident from the top.
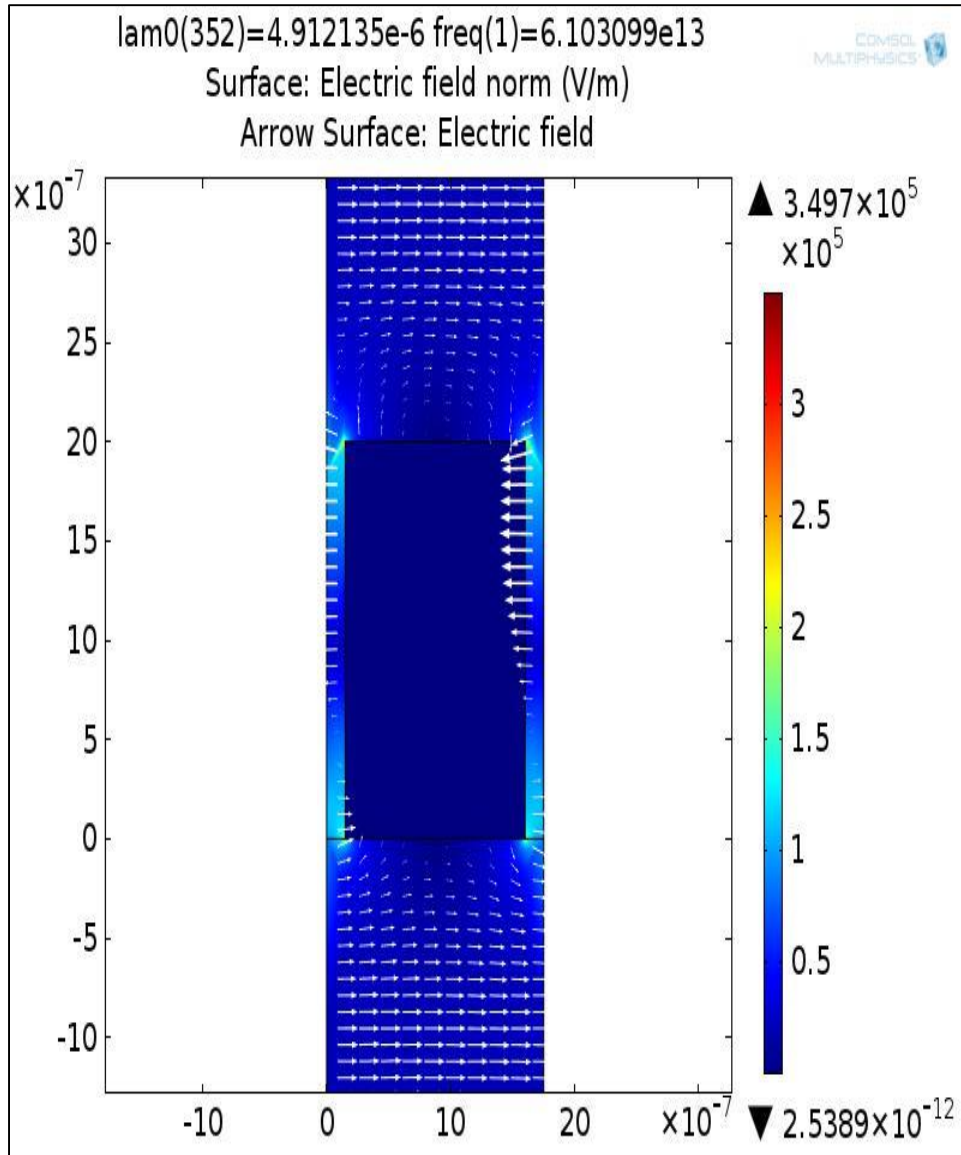
Fig 5-11: Calculated E-Field vector showing cavity resonances from COMSOL. Here d = 1.75 μm, a = 0.3 μm, h = 2.0 μm, and λ = 4.91 μm. Radiation is incident from the top.

The radiation is funneled into the air gaps where the only strong mode interactions occur. There is no strong field excitation on the top or the bottom horizontal surfaces of the wire. Note the electric field vectors are normal to the slit walls indicated a TEM waveguide mode. Fig 5-8, Fig 5-9, Fig 5-10, and Fig 5-11 confirm that there are indeed two mechanisms at work

142

in producing the transmission resonances seen in the GV-MM study and in the COMSOL study. Note that EM field focusing and concentration occurs in both SPP resonant interactions and in waveguide resonant interactions. The focusing is primarily on the top and bottom interfaces with SPP resonances while it is primarily in the air gaps with waveguide resonances. The point of recalculating the GV-MM results was to validate the COMSOL model and modeling processes. A comparison of the COMSOL model results with the published GV-MM results shows that this objective was achieved.

COMSOL was then used to investigate the PWG that was studied in Section 5.2 using HFSS. A 2D model was created in COMSOL as opposed to the 3D model used in HFSS. The use of a 2D model is again justified due to symmetry along the axes if the wire elements. Once more, periodic ports and boundary conditions were applied. The incident radiation was TM polarized and normal to the top surface of the wire element. The frequency was swept from 20 THz to 60 THz (15 μm to 5 μm) in steps of 500 GHz. The zero-order transmission of the structure was studied while varying wire thickness from h = 0.1 μm to 2.0 μm with a wire width fixed at a = 5.0 μm (50% fill factor). The zero-order transmission was also studied while varying wire width from a = 2.0 to 8.0 μm – varying fill factor from 20% to 80 %., with a wire thickness fixed at h = 0.2 μm. The same geometrical model used in the GV-MM study was scaled to use here (see Fig 5-5) so that the grating period for this study was d = 10 μm.

For comparison to the HFSS results, no substrate was initially modeled (Domain 1 was air). Fig 5-12 shows the calculated COMSOL results for the transmittance versus wavelength with various values of the wire element thickness.
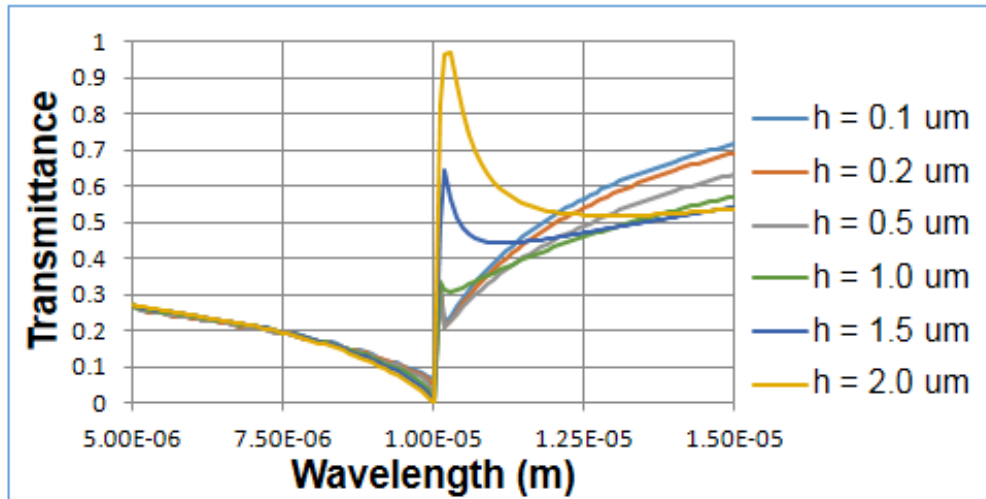
Fig 5-12: Zero-order transmission through a LWIR PWG from 20 THz to 60 THz (15 μm to 5 μm) as calculated with COMSOL. Wire element thickness is varied, h = [0.1, 0.2, 0.5, 1.0, 1.5, 2.0] μm. Wire width is a = 5 μm (50% fill factor). Compare with the HFSS results in Fig 5-2.

These results shows sharp asymmetric resonances for the smaller values of h. The magnitude of the response increases for increasing values of h. In comparing this result with the HFSS result in Fig 5-2, we see that although both COMSOL and HFSS each predict a resonance at approximately λ = 10 μm, the shape of the two resonances is very different. In the HFSS simulation, the possibility that the resonance was being caused by SPPs was ruled out due to the shape and the simulation set up. In the COMSOL case, the shape and the simulation set up both support a SPP explanation.

Fig 5-13 shows the calculated COMSOL results for the transmittance versus wavelength with various values of the wire width (fill factor).

Here the highest transmittance occurs when the wire thickness is the smallest value (smallest fill factor). The transmittance then decreases with increasing wire width (fill factor). A definite resonant peak develops for wire widths from 4 μm ≤ a ≤ 8 μm. Again, the shape of

144
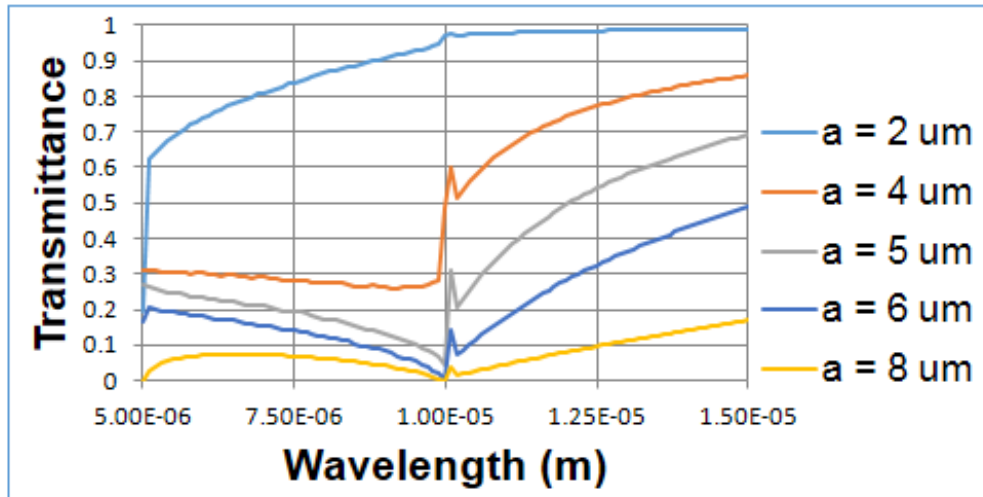
Fig 5-13: Zero-order transmission through a LWIR PWG from 20 THz to 60 THz (15 μm to 5 μm) as calculated with COMSOL. Grating wire width is varied, a = [2.0, 4.0, 5.0, 6.0, 8.0] μm (20%, 40%, 50%, 60%, and 80% fill factors). Wire thickness is h = 0.2 μm. Compare with Fig 5-3.

these resonances and the simulation set up indicate they are caused by SPPs. This can be contrasted with the shape of the HFSS resonances and the HFSS simulation set up (see Fig 5-3).

Up to this point in the study, the objective of using SPP resonances to enhance the coupling between LWIR radiation and LWIR detectors seemed achievable. But, the previous two simulations used a COMSOL model without a substrate. In a real world system, a substrate would be required to improve the mechanical support of the PWG. In addition, a phoconductive material (a photon detector) would most likely be the substrate on which the PWG was mounted. This photon detector would likely be fabricated from a semiconductor bulk material or quantum well structure having a large value of the real and imaginary parts of the dielectric function. Therefore, the next step in this investigation was to simulate the zero-order transmission through a PWG mounted on a substrate. The substrate was modeled

as a lossless homogeneous medium of refractive index n, where n =1 to n = 2.5. Fig 5-14 shows the transmittance versus wavelength results of the COMSOL simulation for a PWG with d = 10 µm, h = 0.2 µm, and a = 5 µm (50% fill factor) while varying n.
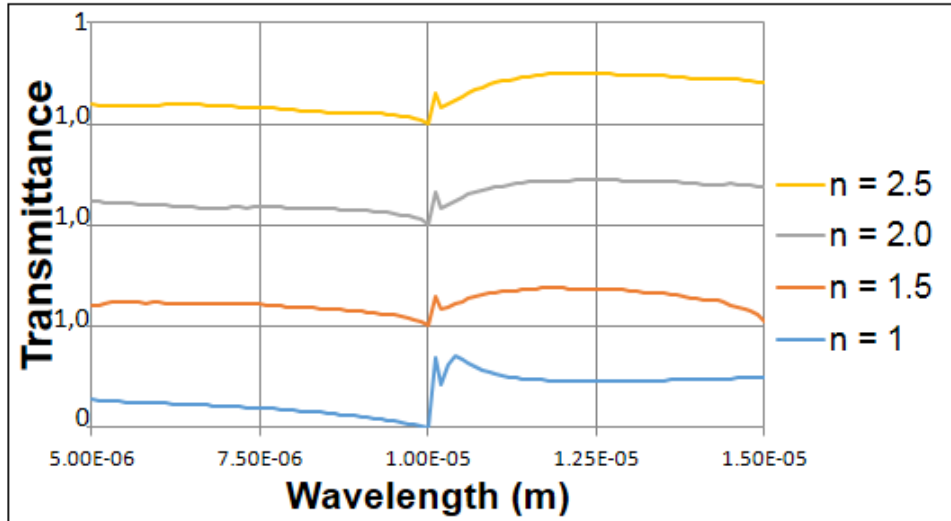
Fig 5-14: Zero-order transmission through a LWIR PWG with Au wires from 20 THz to 60 THz (15 µm to 5 µm). Period is d = 10 µm. Grating wire thickness is h = 0.2 µm. Wire width is a = 5 µm (50% fill factor). Substrate refractive index is varied, n = [1, 1.5, 2.0, 2.5]. Ordinate ranges are from 0 to 1 for each curve.

What is apparent immediately is how quickly the resonant SPP peak is attenuated as n increases. Since the medium is lossless, the low transmittance values for n > 1 are all due to reflection. Real LWIR photon detectors are made from materials that typically have a refractive index values greater than 2.5, for HgCdTe n ≈ 4. In addition, they have finite loss. This simulation result warns of a potential reflection problem when real-world devices are used as substrates unless a method to reduce reflection is employed in this type of design.

Finally, some authors have questioned the use of noble metals for conductors in SPP applications due to interband transitions [38]. A possible alternative often mentioned is a heavily doped transparent conducting oxide such as zinc oxide doped with gallium or indium

tin oxide. Empirical optical data for $Zn_{0.974}Ga_{0.026}O$ [91] was available to use in the building of a material model for use in COMSOL Multiphysics. Using this material model, a PWG was constructed and simulated. The geometry of the ZnO PWG was d = 10 μm, h = 0.2 μm, and a = 5 μm (50% fill factor). The PWG was mounted on a lossless substrate. Fig 5-15 shows the calculation results for transmittance versus wavelength from 5 μm ≤ λ ≤ 15 μm with the substrate refractive index varied from n =1 to n = 2.5.
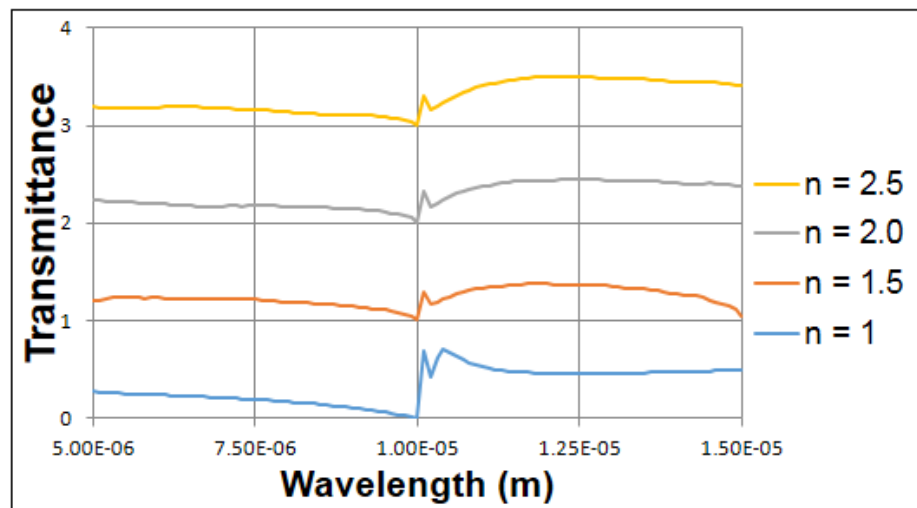
Fig 5-15: Zero-order transmission through a LWIR PWG with $Zn_{0.974}Ga_{0.026}O$ wires from 20 THz to 60 THz (15 μm to 5 μm). Period is d = 10 μm. Grating wire thickness is h = 0.2 μm. Wire width is a = 5 μm (50% fill factor). Substrate refractive index is varied, n = [1, 1.5, 2.0, 2.5]. Ordinate ranges are from 0 to 1 for each curve.

This is essentially the same plot as that shown for an Au PWG in Fig 5-14 with the Au replaced by highly doped ZnO. It is instructive to contrast the two plots. What is seen is that overall the Au performs better than the ZnO. The peak transmittance of the Au is higher than that of the ZnO at all values of n. The non-resonant transmittance of the Au is also slightly better than that seen in the ZnO. This quick computation seems to indicate that in the LWIR region, highly doped ZnO would not be a good substitute for Au as a PWG material.

The study covered by this chapter addressed the use of SPPs generated by 1D PWGs as a means of increasing the coupling between incident LWIR radiation and LWIR photon detectors. Both HFSS and COMSOL Multiphysics were used to simulate the transmission responses and EM fields generated by PWGs. Overall, COMSOL was better suited for this work than HFSS. The primary reason is that these simulations could be done using 2D models in COMSOL; 2D was and is not currently supported in HFSS. In systems with geometric invariance, 2D models have some advantages over 3D models. The main advantage is that 2D models require fewer computational resources (time and memory) than 3D models do. Thus, 2D models allow for more model configurations and scenarios to be explored over a given time span.

In this study, the design idea was more fully investigated with COMSOL than with HFSS. Nevertheless, the COMSOL simulations could not produce a design with strong transmittance resonances at the desired wavelengths (8 − 12 μm) without very thick wire elements (h > 2 μm). Further, the simulations showed that adding a substrate to the design caused a significant drop in the transmittance due to the increased reflectance and that replacing the Au in the wire elements with highly doped ZnO actually lowered performance. No device configuration that generates a strong SPP resonance in the LWIR region was found.

Yet, all is not lost. The transmittance responses observed in this study are all far field phenomena. But, an enhanced far field response may not be needed. It is more likely that the strong near field effects seen in and around the bottom of the PWG structures can be exploited to enhance LWIR detector performance. If a PWG structure can designed that maximizes field penetration depth into real world substrates, for instance doped GaAs or HgCdTe, while still concentrating the fields into a small volume, an enhanced coupling between the incident LWIR

radiation and the active region of a LWIR photon detector could achieved. Study of Fig 5-8 through Fig 5-11 indicates that strong concentrated fields do exist in these areas and could be used to excite charge carriers the active regions of underlying devices. This could allow for the active areas of photon detectors to be decreased, thus decreasing dark currents, while maintaining strong coupling. This would improve detector performance by increasing SNR, responsivity, and specific detectivity. This is something that should be pursed in the next phase of this work.

6. Conclusions

In this study, we examined the phenomenon of extraordinary optical transmission through wire-grid polarizers in the THz region and through plasmonic wire gratings in the LWIR region. For both cases, full wave electromagnetic simulations using the finite element method were used to analyze the transmission spectra and field enhancement. In addition, THz wire-grid polarizer prototypes were fabricated and characterized which confirmed the simulation predictions to within a few dB.

Extraordinary optical transmission was seen in the simulation and experimental results for the THz wire-grid polarizers. Extraordinary optical transmission was seen in the simulation results for the LWIR plasmonic wire gratings. Nevertheless, the physical mechanisms behind the extraordinary optical transmission observed in these structures in these two regions of the electromagnetic spectrum were not the same.

In the THz region, the mechanism was structured surface plasmons. Structured surface plasmons, also called spoof surface plasmons [59], are not real surface plasmons strictly speaking. In the THz region there are three reasons for this. First, the frequencies of THz radiation are too far from the plasma frequencies of these metals for a strong surface plasmonic response to occur. Second, the periods of the wire-grid polarizers are too small relative to the incident radiation for any surface plasmon resonance to occur. Finally, the aluminum and gold, of which the wire-grid polarizers were made in this dissertation, are too close to being perfect electrical conductors in the THz region for surface plasmons to be well confined.

On the other hand, structured surface plasmons may occur when the frequency of the incident radiation is much lower than the plasma frequency of the conducting material. They may occur when the period of the structure is sub-wavelength relative to the incident radiation. They may even occur on perfect electrical conductors as long as they are patterned. This is because structure surface plasmons come about due to the constructive and destructive interference of secondary radiation emanating from oscillating dipoles which form across the apertures in these structures. They are created by and depend on the geometry of the structure, not the electrical characteristics of the conducting material. Their behavior is similar to that seen in metamaterials.

Extraordinary transmission in the THz region, as produced by structured surface plasmons, was manifested has a very high transmittance (much higher than predicted by geometrical optics) in high fill factor polarizers for perpendicularly polarized radiation. The reason for the high transmittance seen with perpendicular polarization was that the perpendicular polarized radiation created oscillating surface charge distributions oriented perpendicular to the wires of the polarizer. These oscillating surface charge distributions generated very high concentrations of electric field energy in the gaps. These fields were coupled to the incident radiation and therefore formed very strong oscillating electric dipoles across the gaps. These dipoles re-radiated incident radiation out of the opposite side of the polarizer. Higher fill factors resulted in higher concentrations of electromagnetic energy in the gaps and thus stronger radiating dipoles.

Meanwhile, a very low transmittance in high fill factor polarizers was observed for parallel polarized radiation. The parallel polarized radiation only created surface charge distributions parallel to the wires. Thus, no oscillating dipoles were formed across the air gaps

and no radiation was transmitted out of the opposite side of the polarizer. When combined, these two phenomena resulted in remarkable extinction ratios, an important figure of merit for polarizers, not previously reported in the literature for single layer polarizers. These results were seen in both simulation and experiment. Thus, a huge improvement in the performance of passive components like wire-grid polarizers was realized by increasing fill factors. A results that may be counter-intuitive but was proven to be true.

Further, it was discovered that creating a compound wire-grid, using an effective fill factor concept, resulted performance that often equaled or exceeded baseline designs. The effective fill factor concept consisted of replacing each metal wire in a baseline wire-grid polarizer design with several thinner wires separated by small air gaps. This caused the actual fill factor of the component to decrease to a value much less than that of the baseline design while its effective fill factor remained the same as the baseline design. The results observed in both simulations and experiment showed that S-polarization transmittances for effective fill factor polarizers where superior to those for baseline designs of higher fill factor. Effective fill factor extinction ratios were also very good compared to baseline designs of higher fill factor and equaled or exceeded them as frequency increased. In addition, these figures of merit were much better for effective fill factor designs than for baseline designs having fill factors equal to those of the actual fill factor of the effective fill factor components. The physical effects seen in the high fill factor baseline designs are realized in effective fill factor designs which have lower actual fill factors and thus less metallization.

In the LWIR region, surface plasmon polaritons and TEM parallel plate waveguide resonances were the causes of extraordinary optical transmission. The gold and ZnO plasmonic wire gratings modeled in the LWIR studies had grating periods either equal to or

within the same order of magnitude of the wavelengths of the incident radiation. Further, the incident LWIR radiation was close enough in frequency to the plasma frequencies of Au and ZnO so that surface plasmons could be supported. In addition, the boundary conditions required for the existence of surface plasmon waves were met in the COMSOL simulations. Finally, by examination of the electromagnetic fields calculated in the COMSOL simulations and the results from Garcia-Vidal and Martin-Moreno [40], we see proof that both surface plasmons polaritons and waveguide modes exist in these structures and are the mechanisms behind EOT.

The motivation for this study was to investigate the use of SPPs generated in 1D plasmonic wire gratings as a means of strengthening the coupling between incident LWIR radiation and LWIR photon detectors. Both HFSS and COMSOL Multiphysics were used to simulate the zero-order transmission and EM fields generated with plasmonic wire gratings. COMSOL was the preferred FEM software package for this work because it allows for the use of 2D models whereas HFSS supports only 3D models.

Nonetheless, the COMSOL simulations did not produce a design with strong transmission resonances at the desired wavelength range of $8 - 12$ μm without resorting to excessively thick wire elements (h > 2 μm). In addition, the simulations showed that adding a substrate beneath the plasmonic wire grating caused a large drop in transmittance because of increased reflectance. Replacing the gold in the wire elements with highly doped ZnO lowered performance.

Therefore, no device configuration that generated a strong SPP resonance in the LWIR region was found. But, there still is an aspect of using plasmonic wire gratings to enhance coupling that still needs to be studied. The zero-order transmission responses calculated in this

dissertation are far field phenomena. An enhanced far field response may not be needed to enhance coupling. It is possible that the strong near field effects calculated in and around the bottom of the plasmonic wire grating structures can be used to enhance LWIR detector performance. If a plasmonic wire grating can be designed that maximizes field penetration depth into photon detector substrates across the LWIR region, while still concentrating the fields into a small volume, an enhanced coupling between the incident LWIR radiation and the active region of a LWIR photon detector may be realized. Fig 5-8 through Fig 5-11 indicate that strong fields do exist in these areas and could be used to excite charge carriers in the active regions of underlying devices.

Finally, this PhD work was a successful example of the use of simulation and experiment as a research and development method. In this dissertation, simulation drove fabrication. Fabrication resulted in experiments and characterization. Characterization verified simulation and posed new computational questions. These component tasks, when used in such a symbiotic manner, create a strong interlinked research and development environment that results in a better understanding of the physical phenomena observed, and a more efficacious and efficient design process. The THz wire-grid polarizers and LWIR plasmonic wire gratings investigated here were but simple examples of many passive quasi-optical components that can be fruitfully explored using this method.

In closing, the research work done in dissertation demonstrates novelty, depth, and utility. Real world devices (THz wire-grid polarizers) were created and demonstrated because of this work. Provisional patents were applied for because of this work. Papers in peer reviewed scientific journals and conference proceedings were published because of this work.

Future research topics to investigate were identified because of this work. The proof of the success of this process and this dissertation is in these results.

Appendix

Matlab File drude_al.m

```matlab
%%%%%%%%%%%%%%%%%%%%%%%%%%%%%%%%%%%%%%%%%%%%%%%%%%%%%%%%%%%%%%%%%%%%%%%
% Drude model for aluminum
%
% By:   John Cetnar
% Date: 12-7-2011
%
%%%%%%%%%%%%%%%%%%%%%%%%%%%%%%%%%%%%%%%%%%%%%%%%%%%%%%%%%%%%%%%%%%%%%%%

% Constants
tau = 0.8e-14;                      % Mean time between collisions in sec at
                                    % 273 K.
                                    % Ashcroft and Mermin, Solid State Physics
                                    % Brooks/Cole, New York, NY (1976).
rho0 = 28.2;                        % DC resistivity in nOhm*m at 293 K.
                                    % http://en.wikipedia.org/wiki/Aluminium
N = 10001;                          % Number of frequencies to sample
eps0 = 1e-9/(36*pi);                % Free space electrical permittivity in
F/m
f1 = 100e9;                         % Starting frequency in Hz
f2 = 4000e9;                        % Ending frequency in Hz

rho0 = rho0*1e-9;                   % DC resistivity in Ohm*m
sigma0 = 1/rho0;                    % DC conductivity in S/m

% Define and initialize variable arrays

sigma1 = zeros(N,1);                % Real part of the conductivity in S/m
sigma2 = zeros(N,1);                % Imaginary part of the conductivity in
S/m
sigma = zeros(N,2);                 % Frequency and real part of the
                                    % conductivity in S/m
eps1 = zeros(N,1);                  % Real part of the permittivity in F/m
eps2 = zeros(N,1);                  % Imaginary part of the permittivity in
F/m
eps1_rel = zeros(N,1);              % Real part of the relative permittivity
eps2_rel = zeros(N,1);             % Imaginary part of the relative
permittivity
eps_rel = zeros(N,2);               % Frequency and real parts of the relative
                                    % permittivity
eps1_rel_eff = zeros(N,1);          % Real part of the effective relative
                                    % permittivity, used by HFSS
eps2_rel_eff = zeros(N,1);          % Imaginary part of the effective relative
                                    % permittivity, used by HFSS
```

156

```matlab
eps_rel_eff = zeros(N,2);        % Frequency and real parts of the relative
                                 % effective permittivity, used by HFSS
loss_tan = zeros(N,1);           % Dielectric loss tangent
freq_tan = zeros(N,2);           % Frequency and dielectric loss tangent.
omega = 2*pi*linspace(f1,f2,N);  % Frequency range in rad/sec

% Calculate the complex, frequency dependent conductivity, permittivity,
% relative permittivity, effective relative permittivity and loss tangent
for i = 1:N
    sigma1(i) = sigma0/(1 + omega(i)^2*tau^2);
    sigma2(i) = sigma0*omega(i)*tau/(1 + omega(i)^2*tau^2);
    eps1(i) = (eps0 - sigma2(i)/omega(i));
    eps2(i) = (sigma1(i)/omega(i));
    eps1_rel(i) = eps1(i)/eps0;
    eps2_rel(i) = eps2(i)/eps0;
    eps1_rel_eff(i) = eps1(i)-sigma2(i)./omega(i)/eps0;
    eps2_rel_eff(i) = eps2(i)+sigma1(i)./omega(i)/eps0;
    loss_tan(i) = -eps2_rel_eff(i)/eps1_rel_eff(i);
end

% Plot the complex conductivity, permittivity, effective relative
permittivity
% and loss tangent versus frequency and store in comma delimited text
files.
figure(1);
plot(omega/(2*pi*1e9),sigma1);
xlabel('f (GHz)');
ylabel('\sigma (S/m)');
grid;
title('Re(\sigma)for Al from the Drude Model');
sigma(:,1) = omega/(2*pi);
sigma(:,2) = sigma1;
dlmwrite('sigma_al.tab',sigma,'delimiter','\t','precision','%.6f');

figure(2);
semilogy(omega/(2*pi*1e9),sigma2);
xlabel('f (GHz)');
ylabel('\sigma (S/m)');
grid;
title('Im(\sigma)for Al from the Drude Model');

figure(3);
plot(omega/(2*pi*1e9),eps1_rel);
xlabel('f (GHz)');
ylabel('\epsilon');
grid;
title('Re(\epsilon) for Al from the Drude Model');
eps_rel(:,1) = omega/(2*pi);
eps_rel(:,2) = eps1_rel;
dlmwrite('eps_rel_al.tab',eps_rel,'delimiter','\t','precision','%.6f');

figure(4);
semilogy(omega/(2*pi*1e9),eps2_rel);
xlabel('f (GHz)');
ylabel('\epsilon');
grid;
```

```matlab
title('Im(\epsilon) for Al from the Drude Model');

figure(5);
semilogy(omega/(2*pi*1e9),loss_tan);
xlabel('f (GHz)');
ylabel('tan(\delta)');
grid;
title('Loss Tangent for Aluminum from the Drude Model');
freq_tan(:,1) = omega/(2*pi);
freq_tan(:,2) = loss_tan;
dlmwrite('freq_tan_al.tab',freq_tan,'delimiter','\t','precision','%.6f');
```

Matlab File drude_au.m

```matlab
%%%%%%%%%%%%%%%%%%%%%%%%%%%%%%%%%%%%%%%%%%%%%%%%%%%%%%%%%%%%%%%%
% Drude model for gold
%
% By:   John Cetnar
% Date: 3-19-2012
%
%%%%%%%%%%%%%%%%%%%%%%%%%%%%%%%%%%%%%%%%%%%%%%%%%%%%%%%%%%%%%%%%

% Constants
clear all;
clc;

tau = 3.0e-14;                 % Mean time between collisions in sec at
                               % 273 K.
                               % Ashcroft and Mermin, Solid State Physics
                               % Brooks/Cole, New York, NY (1976).
rho0 = 22.14;                  % DC resistivity in nOhm*m at 293 K.
                               % http://en.wikipedia.org/wiki/Gold
N = 10001;                     % Number of frequencies to sample
eps0 = 1e-9/(36*pi);           % Free space electrical permittivity in
F/m
f1 = 100e9;                    % Starting frequency in Hz
f2 = 4000e9;                    % Ending frequency in Hz

rho0 = rho0*1e-9;              % DC resistivity in Ohm*m
sigma0 = 1/rho0;               % DC conductivity in S/m

% Define and initialize variable arrays

sigma1 = zeros(N,1);           % Real part of the conductivity in S/m
sigma2 = zeros(N,1);           % Imaginary part of the conductivity in
S/m
sigma = zeros(N,2);            % Frequency and real part of the
                               % conductivity in S/m
eps1 = zeros(N,1);             % Real part of the permittivity in F/m
eps2 = zeros(N,1);             % Imaginary part of the permittivity in
F/m
eps1_rel = zeros(N,1);         % Real part of the relative permittivity
eps2_rel = zeros(N,1);         % Imaginary part of the relative
permittivity
eps_rel = zeros(N,2);          % Frequency and real parts of the relative
                               % permittivity
eps1_rel_eff = zeros(N,1);     % Real part of the effective relative
                               % permittivity, used by HFSS
eps2_rel_eff = zeros(N,1);     % Imaginary part of the effective relative
                               % permittivity, used by HFSS
eps_rel_eff = zeros(N,2);      % Frequency and real parts of the relative
                               % effective permittivity, used by HFSS
loss_tan = zeros(N,1);         % Dielectric loss tangent
freq_tan = zeros(N,2);         % Frequency and dielectric loss tangent.
omega = 2*pi*linspace(f1,f2,N); % Frequency range in rad/sec
```

```matlab
% Calculate the complex, frequency dependent conductivity, permittivity,
% relative permittivity, effective relative permittivity and loss tangent
for i = 1:N
    sigma1(i) = sigma0/(1 + omega(i)^2*tau^2);
    sigma2(i) = sigma0*omega(i)*tau/(1 + omega(i)^2*tau^2);
    eps1(i) = (eps0 - sigma2(i)/omega(i));
    eps2(i) = (sigma1(i)/omega(i));
    eps1_rel(i) = eps1(i)/eps0;
    eps2_rel(i) = eps2(i)/eps0;
    eps1_rel_eff(i) = eps1(i)-sigma2(i)./omega(i)/eps0;
    eps2_rel_eff(i) = eps2(i)+sigma1(i)./omega(i)/eps0;
    loss_tan(i) = -eps2_rel_eff(i)/eps1_rel_eff(i);
end

% Plot the complex conductivity, permittivity, effective relative
permittivity
% and loss tangent versus frequency and store in comma delimited text
files.
figure(1);
semilogy(omega/(2*pi*1e9),sigma1,omega/(2*pi*1e9),sigma2);
xlabel('f (GHz)');
ylabel('\sigma (S/m)');
grid;
title('Conductivity for Gold from the Drude Model');
legend('Real(\sigma)','Imag(\sigma)','location','southeast');
sigma(:,1) = omega/(2*pi);
sigma(:,2) = sigma1;
dlmwrite('sigma_au.tab',sigma,'delimiter','\t','precision','%.6f');

figure(2);
plot(omega/(2*pi*1e9),eps1_rel,omega/(2*pi*1e9),eps2_rel,omega/(2*pi*1e9),
eps1_rel_eff);
xlabel('f (GHz)');
ylabel('\epsilon');
grid;
title('Relative Permittivity for Gold from the Drude Model');
legend('Real(\epsilon)','Imag(\epsilon)','Real(\epsilon-
eff)','location','northeast');
eps_rel(:,1) = omega/(2*pi);
eps_rel(:,2) = eps1_rel;
eps_rel_eff(:,1) = omega/(2*pi);
eps_rel_eff(:,2) = eps1_rel_eff;
dlmwrite('eps_rel_au.tab',eps_rel,'delimiter','\t','precision','%.6f');
dlmwrite('eps_rel_eff_au.tab',eps,'delimiter','\t','precision','%.6f');

figure(3);
semilogy(omega/(2*pi*1e9),loss_tan);
xlabel('f (GHz)');
ylabel('tan(\delta)');
grid;
title('Loss Tangent for Gold from the Drude Model');
freq_tan(:,1) = omega/(2*pi);
freq_tan(:,2) = loss_tan;
dlmwrite('freq_tan_au.tab',freq_tan,'delimiter','\t','precision','%.6f');
```

Bibliography

[1]   A. Rogalski, *Infrared Detectors*, 2nd ed. Boca Raton, FL: CRC Press, 2011, pp. 1–40.

[2]   P. H. Siegel, "Terahertz technology," *IEEE Trans. Microw. Theory Tech.*, vol. 50, no. 3, pp. 910–928, Mar. 2002.

[3]   G. Gallerano and S. Biedron, "Overview of terahertz radiation sources," in *Proceedings of the 2004 FEL Conference*, 2004, pp. 216–221.

[4]   I. Duling and D. Zimdars, "Terahertz imaging: Revealing hidden defects," *Nat. Photonics*, vol. 3, no. 11, pp. 630–632, Nov. 2009.

[5]   C. Medrano, "Monitoring Terahertz Technology," 2008.

[6]   J. F. Federici, D. Gary, R. Barat, and D. Zimdars, "Thz standoff detection and imaging of explosives and weapons," in *2005 Proceedings of the SPIE*, 2005, vol. 5781, pp. 75–84.

[7]   D. Gu, *Terahertz imaging system using hot electron bolometer technology*. 2007, pp. 1 − 174.

[8]   A. Rostami, H. Rasooli, and H. Baghban, *Terahertz Technology: Fundamentals and Applications (Google eBook)*, vol. 2010. Springer, 2010, p. 260.

[9]   D. Johnson and G. Brooker, "Research radar for unmanned navigation," in *2008 International Conference on Radar*, 2008, pp. 165–170.

[10]   X. Yin, B. W.-H. Ng, and D. Abbott, *Terahertz Imaging for Biomedical Applications: Pattern Recognition and Tomographic Reconstruction*. New York: Springer, 2012, pp. 45–244.

[11]   X.-C. Z. Albert Redo-Sanchez, Gurpreet Kaur, "2-D Acoustic Phase Imaging With Millimeter-Wave Radiation," *IEEE Trans. Microw. Theory Tech.*, vol. 57, no. 3, pp. 589–593, Mar. 2009.

[12] C. D. Stoik, M. J. Bohn, and J. L. Blackshire, "Nondestructive evaluation of aircraft composites using transmissive terahertz time domain spectroscopy.," *Opt. Express*, vol. 16, no. 21, pp. 17039–51, Oct. 2008.

[13] L. Owens, D. T. Petkie, and J. A. Deibel, "Non-Destructive Evaluation of Aerospace Materials using Terahertz Time-Domain Imaging," in *Imaging and Applied Optics Technical Papers*, 2012, vol. 2, p. SW4C.4.

[14] D. T. Petkie, C. Benton, and E. Bryan, "Millimeter wave radar for remote measurement of vital signs," *2009 IEEE Radar Conf.*, no. 2, pp. 1–3, 2009.

[15] D. T. Petkie, C. Benton, and E. Bryan, "Millimeter-wave radar for vital signs sensing," in *Radar Sensor Technology XIII*, 2009, vol. 7308, p. 73080A–73080A–5.

[16] Z. D. Taylor, R. S. Singh, M. O. Culjat, J. Y. Suen, W. S. Grundfest, H. Lee, and E. R. Brown, "Reflective terahertz imaging of porcine skin burns.," *Opt. Lett.*, vol. 33, no. 11, pp. 1258–60, Jun. 2008.

[17] M. H. Arbab, T. C. Dickey, D. P. Winebrenner, A. Chen, M. B. Klein, and P. D. Mourad, "Terahertz reflectometry of burn wounds in a rat model.," *Biomed. Opt. Express*, vol. 2, no. 8, pp. 2339–47, Aug. 2011.

[18] D. B. Bennett, W. Li, Z. D. Taylor, W. S. Grundfest, and E. R. Brown, "Stratified Media Model for Terahertz Reflectometry of the Skin," *IEEE Sens. J.*, vol. 11, no. 5, pp. 1253–1262, May 2011.

[19] Y. Sun, M. Y. Sy, Y.-X. J. Wang, A. T. Ahuja, Y.-T. Zhang, and E. Pickwell-Macpherson, "A promising diagnostic method: Terahertz pulsed imaging and spectroscopy.," *World J. Radiol.*, vol. 3, no. 3, pp. 55–65, Mar. 2011.

[20] C. Townes, "The present status of microwave spectroscopy," *Ann. N. Y. Acad. Sci.*, vol. 55, pp. 745–750, 1952.

[21] R. Hall and J. Dowling, "Pure rotational spectrum of water vapor," *J. Chem. Phys.*, vol. 47, no. 7, pp. 2454–2461, 1967.

[22] P. Rosenkranz, "Interference coefficients for overlapping oxygen lines in air," *J. Quant. Spectrosc. Radiat. Transf.*, vol. 39, no. 4, pp. 287–297, 1988.

[23] B. J. Drouin and F. W. Maiwald, "Extended THz measurements of nitrous oxide, N2O," *J. Mol. Spectrosc.*, vol. 236, no. 2, pp. 260–262, Apr. 2006.

[24] C. Kulesa, "Terahertz Spectroscopy for Astronomy: From Comets to Cosmology," *IEEE Trans. Terahertz Sci. Technol.*, vol. 1, no. 1, pp. 232–240, Sep. 2011.

[25] M. V. Zombeck, *Handbook of Space Astronomy and Astrophysics*, 3rd ed. Cambridge, United Kingdom: Cambridge University Press, 2007, pp. 211–232.

[26] S. T. Fiorino, R. J. Bartell, M. J. Krizo, S. L. Marek, M. J. Bohn, R. M. Randall, and S. J. Cusumano, "A computational tool for evaluating THz imaging performance in brownout or whiteout conditions at land sites throughout the world," in *SPIE7324 Atmospheric Propagation IV*, 2009, vol. 7324, pp. 732410–732410–12.

[27] H. G. Young and R. A. Freedman, *University Physics with Modern Physics*, 11th ed. San Francisco: Addison Wesley, 2004, pp. 1474–1477.

[28] E. R. Brown, "Fundamentals of Terrestial Millimeter-Wave and THz Remote Sensing," in *Terrahertz Sensing Technology, Vol. 2: Emerging Scientific Applications and Novel Device Concepts*, D. L. Woolard, W. R. Loerop, and M. S. Shur, Eds. Singapore: World Scientific Publishing, 2004.

[29] J. C. Wiltse, "History of millimeter and submillimeter waves," *IEEE Trans. Microw. Theory Tech.*, vol. 32, pp. 118–127, 1984.

[30] R. H. Kingston, *Detection of Optical and Infrated Radiation*. Berlin, Germany: Springer-Verlag, 1978, p. 45.

[31] M. S. Shishodia and a. G. Unil Perera, "Heterojunction plasmonic midinfrared detectors," *J. Appl. Phys.*, vol. 109, no. 4, p. 043108, 2011.

[32] P. Norton, "HgCdTe infrared detectors," *Opto-electronics Review*, 2002. [Online]. Available: http://www.wat.edu.pl/review/optor/10(3)159.pdf. [Accessed: 27-Jan-2014].

[33] "Mercury cadmium telluride," *Wikipedia Foundation Inc.* [Online]. Available: http://en.wikipedia.org/wiki/Mercury_cadmium_telluride. [Accessed: 29-Jan-2014].

[34] M. W. Scott, "Energy Gap in Hg1−xCdxTe by Optical Absorption," *J. Appl. Phys.*, vol. 40, no. 10, p. 4077, Sep. 1969.

[35] P. Capper, *Properties of Narrow Gap Cadmium-Based Compounds*, 1st ed. London: INSPEC, The Institution of Electrical Engineers, 1994, pp. 80–81.

[36] T. W. Ebbesen, H. J. Lezec, H. F. Ghaemi, T. Thio, and P. A. Wolff, "Extraordinary optical transmission through sub-wavelength hole arrays," *Nature*, vol. 391, no. 12 February 1998, pp. 667–669, 1998.

[37] H. Bethe, "Theory of Diffraction by Small Holes," *Phys. Rev.*, vol. 66, no. 7–8, pp. 163–182, Oct. 1944.

[38] J. B. Khurgin and A. Boltasseva, "Reflecting upon the losses in plasmonics and metamaterials," *Mater. Res. Soc. Bull.*, vol. 37, no. August, pp. 768–779, 2012.

[39] C. Kittel, *Introduction to Solid State Physics*, 8th ed. Hoboken, NJ: John Wiley & Sons, 2005, p. 413.

[40] F. García-Vidal and L. Martín-Moreno, "Transmission and focusing of light in one-dimensional periodically nanostructured metals," *Phys. Rev. B*, vol. 66, no. 15, p. 155412, Oct. 2002.

[41] F. J. Garcia-Vidal, L. Martin-Moreno, T. W. Ebbesen, and L. Kuipers, "Light passing through subwavelength apertures," *Rev. Mod. Phys.*, vol. 82, no. 1, pp. 729–787, Mar. 2010.

[42] S. A. Maier, *Plasmonics: Fundamentals and Applications*. New York: Springer Science + Business Media, 2007, pp. 89–101.

[43] N. W. Ashcroft and N. D. Mermin, *Solid State Physics*. New York: Holt, Rinehart and Winston, 1976, p. 27.

[44] J. R. Sambles, G. W. Bradbery, and F. Yang, "Optical excitation of surface plasmons: An introduction," *Contemp. Phys.*, vol. 32, no. 3, pp. 173–183, May 1991.

[45] M. a Ordal, L. L. Long, R. J. Bell, S. E. Bell, R. R. Bell, R. W. Alexander, and C. a Ward, "Optical properties of the metals Al, Co, Cu, Au, Fe, Pb, Ni, Pd, Pt, Ag, Ti, and W in the infrared and far infrared.," *Appl. Opt.*, vol. 22, no. 7, pp. 1099–20, Apr. 1983.

[46] T. W. Ebbesen, C. Genet, and S. I. Bozhevolnyi, "Surface-plasmon circuitry," *Phys. Today*, vol. 61, no. 5, p. 44, May 2008.

[47] W. L. Barnes, A. Dereux, and T. W. Ebbesen, "Surface plasmon subwavelength optics.," *Nature*, vol. 424, no. 6950, pp. 824–30, Aug. 2003.

[48] A. Otto, "Excitation of nonradiative surface plasma waves in silver by the method of frustrated total reflection," *Zeitschrift fur Phys.*, vol. 216, no. 4, pp. 398–410, Aug. 1968.

[49] E. Kretschmann and H. Raether, "Radiative decay of nonradiative surface plasmons excited by light," *Z. Naturforsch. A*, vol. 23, 1968.

[50] H. Ghaemi, T. Thio, D. Grupp, T. Ebbesen, and H. Lezec, "Surface plasmons enhance optical transmission through subwavelength holes," *Phys. Rev. B*, vol. 58, no. 11, pp. 6779–6782, Sep. 1998.

[51] "Parallel Plate Waveguide," *Amanogawa.com Interactive Software for Education*. [Online]. Available: http://www.amanogawa.com/archive/docs/EM12.pdf.

[52] J. Porto, F. García-Vidal, and J. Pendry, "Transmission Resonances on Metallic Gratings with Very Narrow Slits," *Phys. Rev. Lett.*, vol. 83, no. 14, pp. 2845–2848, Oct. 1999.

[53] X.-R. Huang and R.-W. Peng, "General mechanism involved in subwavelength optics of conducting microstructures: charge-oscillation-induced light emission and interference.," *J. Opt. Soc. Am. A. Opt. Image Sci. Vis.*, vol. 27, no. 4, pp. 718–29, Apr. 2010.

[54] H. E. Went, A. P. Hibbins, J. R. Sambles, C. R. Lawrence, and A. P. Crick, "Selective transmission through very deep zero-order metallic gratings at microwave frequencies," *Appl. Phys. Lett.*, vol. 77, no. 18, p. 2789, Oct. 2000.

[55] M. Beruete and M. Sorolla, "Enhanced millimeter wave transmission through quasioptical subwavelength perforated plates," *IEEE Trans. Antennas Propag.*, vol. 53, no. 6, pp. 1897–1903, 2005.

[56] H. Cao and A. Nahata, "Resonantly enhanced transmission of terahertz radiation through a periodic array of subwavelength apertures.," *Opt. Express*, vol. 12, no. 6, pp. 1004–10, Mar. 2004.

[57] COMSOL, "Model Gallery: Optical Scattering Off of a Gold Nanosphere." [Online]. Available: http://www.comsol.com/model/optical-scattering-by-gold-nanospheres-14697. [Accessed: 02-Aug-2014].

[58] X. Huang, R. Peng, Z. Wang, F. Gao, and S. Jiang, "Charge-oscillation-induced light transmission through subwavelength slits and holes," *Phys. Rev. A*, vol. 76, no. 3, p. 035802, Sep. 2007.

[59] J. B. Pendry, L. Martín-Moreno, and F. J. Garcia-Vidal, "Mimicking surface plasmons with structured surfaces.," *Science*, vol. 305, no. 5685, pp. 847–8, Aug. 2004.

[60] M. Born and E. Wolfe, *Principles of Optics*, 7th ed. New York: Cambridge University Press, 2002, p. 43.

[61] W. B. Zimmerman, *Multiphysics Modelling with Finite Element Methods*. Hackensack: World Scientific Publishing, 2006, pp. 81–84.

[62] P. Drude, "Zur Elektronentheorie der Metalle," *Ann. Phys.*, vol. 306, no. 3, pp. 566–613, 1900.

[63] "Dielectric loss," *Wikipedia Foundation Inc.* [Online]. Available: http://en.wikipedia.org/wiki/Dielectric_loss. [Accessed: 02-Jan-2014].

[64] S. Lucyszyn, "Investigation of anomalous room temperature conduction losses in normal metals at terahertz frequencies," *IEE Proceedings-Microwaves, Antennas Propag.*, vol. 151, no. 4, pp. 321–329, 2004.

[65] P. B. Johnson and R. W. Christy, "Optical Constants of the Noble Metals," *Phys. Rev. B*, vol. 6, no. 12, pp. 4370–4379, Dec. 1972.

[66] H. Hertz, *Electric Waves*. London: Macmillan and Company, 1893, p. 177.

[67] W. T. E. Vaessen, J. Dyk, and v. d. A. Vorst, "RF Shielding Due to Building Structures Like Brick Walls, Wire Grids and Metal Coated Windows," in *18th European Microwave Conference, 1988*, 1988, pp. 625–631.

[68] A. Isozaki, T. Kan, K. Takano, M. Hangyo, K. Matsumoto, and I. Shimoyama, "Double-Layer Wire Grid Polarizer for Improving Extinction Ratio," in *The 17th International Conference on Transducers and Eurosensors*, 2013, no. June, pp. 530–533.

[69] H. Park, H. Zhe, E. P. Parrott, A. Chan, and E. Pickwell-MacPherson, "Novel wire grid polarizer for accurate antenna characterization," in *2012 37th International Conference on Infrared, Millimeter, and Terahertz Waves*, 2012, pp. 1–3.

[70] H. Garvin, J. Kiefer, and S. Somekh, "Wire-grid polarizers for 10.6-µm radiation," *IEEE J. Quantum Electron.*, vol. 9, no. 6, pp. 718–719, Jun. 1973.

[71] X. J. Yu and H. S. Kwok, "Optics of LCOS projection system based on wire-grid polarizers," in *Proceedings of the Sixth Chinese Optoelectronics Symposium (IEEE Cat. No.03EX701)*, 2003, pp. 189–192.

[72] A. Higo, T. Lee, S. Maruyama, H. Fujita, Y. Nakano, and H. Toshiyoshi, "Transmission color control by stacked wire-grid polarizers with in-plane rotation," in *16th International Conference on Optical MEMS and Nanophotonics*, 2011, pp. 209–210.

[73] J. J. Wang, F. Walters, X. Liu, P. Sciortino, and X. Deng, "High-performance, large area, deep ultraviolet to infrared polarizers based on 40 nm line/78 nm space nanowire grids," *Appl. Phys. Lett.*, vol. 90, no. 6, p. 061104, Feb. 2007.

[74] V. Pelletier, K. Asakawa, M. Wu, D. H. Adamson, R. A. Register, and P. M. Chaikin, "Aluminum nanowire polarizing grids: Fabrication and analysis," *Appl. Phys. Lett.*, vol. 88, no. 21, p. 211114, May 2006.

[75] "Polarizer," *Wikipedia Foundation Inc.* [Online]. Available: http://en.wikipedia.org/wiki/Polarizer.

[76] P. Piksa and S. Zvanovec, "Specific usage of a wire-grid polarizer for millimeter waves," in *2010 Proceedings of the Fourth European Conference on Antennas and Propagation (EuCAP)*, 2010, pp. 6–8.

[77] I. Yamada, K. Takano, M. Hangyo, M. Saito, and W. Watanabe, "Terahertz wire-grid polarizers with micrometer-pitch Al gratings.," *Opt. Lett.*, vol. 34, no. 3, pp. 274–6, Feb. 2009.

[78] L. Zhang, J. H. Teng, H. Tanoto, S. Y. Yew, L. Y. Deng, and S. J. Chua, "Terahertz wire-grid polarizer by nanoimprinting lithography on high resistivity silicon substrate," in *35th International Conference on Infrared, Millimeter, and Terahertz Waves (IRMMW-THz)*, 2010, pp. 2–3.

[79] K. Takano, H. Yokoyama, A. Ichii, I. Morimoto, and M. Hangyo, "Wire-grid polarizer sheet in the terahertz region fabricated by nanoimprint technology.," *Opt. Lett.*, vol. 36, no. 14, pp. 2665–7, Jul. 2011.

[80] F. T. Ulaby, *Fundamentals of Applied Electromagnetics*, 2004 Media. Upper Saddle River, NJ: Peason Prentice Hall, 2004, p. 282.

[81] D. M. Pozar, *Microwave Engineering*, 4th ed. Singapore: John Wiley & Sons, 2012, pp. 147–151.

[82] J. R. Middendorf, J. S. Cetnar, J. L. Owsley, and E. R. Brown, "Substrate-Based Wire-Grid Polarizers and Beam-Splitters with High Extinction Ratios," *IEEE Trans. Terahertz Sci. Technol.*, 2014.

[83] J. S. Cetnar, J. R. Middendorf, and E. R. Brown, "Extraordinary optical transmission and extinction in a Terahertz wire-grid polarizer," *Appl. Phys. Lett.*, vol. 100, no. 23, p. 231912, 2012.

[84] J. S. Cetnar, J. R. Middendorf, and E. R. Brown, "Finite-element simulation and design of a high-extinction-ratio THz wire-grid polarizer," in *2012 IEEE National Aerospace and Electronics Conference (NAECON)*, 2012, pp. 20–23.

[85] J. S. Cetnar, J. R. Middendorf, and E. R. Brown, "Effective fill-factor design results in extraordinary optical transmission in a THz wire-grid polarizer," in *2013 38th International Conference on Infrared, Millimeter, and Terahertz Waves (IRMMW-THz)*, 2013, pp. 1–2.

[86] D. Skigin and R. Depine, "Transmission Resonances of Metallic Compound Gratings with Subwavelength Slits," *Phys. Rev. Lett.*, vol. 95, no. 21, p. 217402, Nov. 2005.

[87] H. R. Philipp, "Silicon Dioxide (SiO2), Type alpha (Crystalline)," in *Handbook of Optical Constants of Solids*, E. D. Palik, Ed. Orlando, FL: Academic Press, Inc, 1985, pp. 746–747.

[88]   E. V Loewenstein, D. R. Smith, and R. L. Morgan, "Optical constants of far infrared materials. 2: crystalline solids.," *Appl. Opt.*, vol. 12, no. 2, pp. 398–406, Feb. 1973.

[89]   R. Ulrich, "Far-infrared properties of metallic mesh and its complimentary structure," *Infrared Phys.*, vol. 7, pp. 37–55, 1967.

[90]   R. Singh, I. Al-Naib, M. Koch, and W. Zhang, "Sharp Fano resonances in THz metamaterials," *Opt. Express*, vol. 19, no. 7, pp. 6312–9, Mar. 2011.

[91]   J. W. Cleary, M. Snure, K. D. Leedy, D. C. Look, K. Eyink, and A. Tiwari, "Mid- to long-wavelength infrared surface plasmon properties in doped zinc oxides," in *SPIE Security + Defence*, 2012, vol. 6, no. 1, pp. 854504–854504–10.